

<https://doi.org/10.15388/vu.thesis.145>

<https://orcid.org/0000-0002-9360-5118>

VILNIUS UNIVERSITY  
CENTER FOR PHYSICAL SCIENCES AND TECHNOLOGY

Linus  
JONUŠAUSKAS

# 3D Laser Lithography of Meso-Scale Structures: Towards Applications

**DOCTORAL DISSERTATION**

Technological sciences

Material engineering (T 008)

---

VILNIUS 2021

The doctoral dissertation was prepared at Vilnius University during 2016–2020.

**Scientific supervisor** – dr. Mangirdas Malinauskas (Vilnius University, Technological Sciences, Material Engineering – T 008).

<https://doi.org/10.15388/vu.thesis.145>

<https://orcid.org/0000-0002-9360-5118>

VILNIAUS UNIVERSITETAS  
FIZINIŲ IR TECHNOLOGIJOS MOKSLŲ CENTRAS

Linas  
JONUŠAUSKAS

# Mezoskalinių darinių gamyba 3D lazerine litografija: link taikymų

**DAKTARO DISERTACIJA**

Technologijos mokslai  
Medžiagų inžinerija (T 008)

---

VILNIUS 2021

Disertacija rengta 2016–2020 metais Vilniaus universitete.

**Mokslinis vadovas** – dr. Mangirdas Malinauskas (Vilniaus universitetas, technologijos mokslai, medžiagų inžinerija – T 008).

# Acknowledgement

*There are no desperate situations, there are only desperate people.*

Heinz Guderian

I believe that every decision we ever make is taken by time and sewed into a pattern we call life. And it is only up to us to decide if that would be something we are ashamed of and want to hide, or will it be a cloak that we can wear each day with pride and honor. The path that I took had led me to this very moment writing these words for my Ph.D. thesis. And while I am the one responsible for all the decisions and actions that led me here, there are people who in one form or another influenced me along the way. Here I will list those whom I remember dearly for their help and support in making all the right moves and helping me to cope with the consequences of bad ones.

I was blessed with the extreme support and understanding of my family. From childhood through the teenage years, they taught me that I and only I am responsible for my actions and decisions. This notion of free choice in life formed the basis for my personality. Thus, I would like to thank my family: Father Audrius, Mother Nijolė (who, unfortunately, passed away), my Stepmother Vanda, and Grandmother Veronika (who is also not with us anymore). Without You, I would not be where I am as a person. Additionally, as years pass, the role of the family is slowly supplemented by the friendships. Some good, some bad, but all rewarding and adding to what I identify as "myself". From all the wonderful people whom I met over the years, I would like to say special thanks to Monika, Greta, and Karolina. I could not appreciate more all the time I had the pleasure to call You Friends.

I love the science field I am in. It would not be possible without the great education I got in the Vilnius University Faculty of Physics. I would like to thank all the lecturers I had the pleasure to learn from. Laser Research Center is an institution where I learned the practical aspects of the art of laser research. A lot of people from there helped me to get

where I am today. Thus, I would like to thank all of the Laser Research Center and some people in particular. Prof. A. Piskarskas for capturing my imagination and offering to join the prestigious club of Lithuania's laser researchers. Prof. R. Gadonas for inviting me to His group. My older colleagues dr. S. Rekštytė, dr. V. Purlys and dr. A. Žukauskas for their patience teaching me to be proficient in the lab. My peers dr. Darius and dr. Titas for the cooperation and good times in the lab. My younger collaborators Gabrielius, Laurynas, Agnė, Tomas, and Dovilė, who in one way or another, contributed to this dissertation. The Reviewers of this dissertation, Prof. Dr. Mikas Vengris, and Dr. Gediminas Račiukaitis, deserve mention as well - their fierce but honest critique helped to improve the final version of this dissertation immensely. And, of course, my scientific supervisor dr. M. Malinauskas - He is the main person who captured my imagination in this area and showed what true passion for science looks like. I would not be where I am without Him.

Finally, while this dissertation marks the end of my "student days" I view it as a new beginning. A stepping stone for my further career in the private sector. For an opportunity to grow in this regard I would like to thank my senior colleagues from "Femtika", especially Vidmantas Šakalys and Valdas Monkus. Working with them shows just how much more I can learn and grow outside of laser science. With them, I see that the sky is the limit. They showed me the door. Now I just need to go through it. And for this opportunity, I would like to thank them.

When one chapter ends, something else starts. And I like new beginnings.

Linus Jonušauskas  
2021-01-23

# Contents

<b>List of Abbreviations</b>	<b>9</b>
<b>Introduction</b>	<b>10</b>
<b>1 Literature Review</b>	<b>21</b>
1.1 Additive <i>vs</i> Subtractive Manufacturing . . . . .	21
1.2 General Overview of Optical 3D Printing . . . . .	23
1.2.1 Various Optical 3D Printing Techniques . . . . .	24
1.2.2 Applications of Macro-3D Printing . . . . .	28
1.2.3 Perspectives of the Technology . . . . .	29
1.3 Femtosecond Lasers in Material Processing . . . . .	30
1.3.1 Interaction Between Materials and Ultrashort Pulses	30
1.3.2 Various Femtosecond Processing Examples . . . . .	33
1.3.3 Perspectives of Femtosecond Manufacturing Field . .	36
1.4 3D Laser Lithography . . . . .	37
1.4.1 Photopolymerization <i>via</i> fs-Induced Non-Linear Light-Matter Interactions . . . . .	38
1.4.2 Direct sub-Wavelength Fabrication . . . . .	41
1.4.3 Compatibility with Other Fabrication Methods . . .	43
1.4.4 Towards 4D Printing . . . . .	44
1.5 Applications of 3D Laser Lithography . . . . .	45
<b>2 Experimental Section</b>	<b>48</b>
2.1 Fabrication Setups . . . . .	48
2.2 Materials and Characterization . . . . .	50
2.3 Laser Induced Damage Threshold Measurement . . . . .	52
<b>3 High-Throughput 3D Mesoscale Manufacturing</b>	<b>55</b>
3.1 Comparison of Structuring Rates . . . . .	56
3.1.1 Expanding Throughput with Different Focusing Optics	64

3.2	Functional 3D Mesoscale Structures . . . . .	69
3.2.1	Refractive Optics . . . . .	72
3.2.2	Free-form Mechanical Structures . . . . .	75
3.3	Conclusions . . . . .	79
<b>4</b>	<b>3D Laser Lithography of Non-Photosensitized SZ2080</b>	<b>81</b>
4.1	Fabrication Window and Resolution . . . . .	81
4.2	Structure Quality with Various Focusing Conditions . . . . .	85
4.3	Conclusions . . . . .	91
<b>5</b>	<b>Optical Resiliency of Laser Made Structures</b>	<b>92</b>
5.1	Qualitative Investigation of Microlens Optical Resilience . . . . .	92
5.2	Quantitative Investigation of LIDT for Laser Made 3D Structures . . . . .	96
5.3	Conclusions . . . . .	105
	<b>Bibliography</b>	<b>107</b>
	<b>Santrauka</b>	<b>131</b>
	<b>Curriculum Vitae</b>	<b>133</b>



# List of Abbreviations

3DP	3D printing
O3DP	Optical 3D printing
SLA	Stereolithography
SLS/M	Selective laser sintering/melting
LIFT	Laser induced forward transfer
fs	Femtosecond
ps	Picosecond
ns	Nanosecond
CW	Continuous wave laser
DPSS	Diode pumped solid state
LOC	Lab-on-chip
LASE	Laser-assisted selective etching
3DLL	3D Laser lithography
TPP	Two-photon polymerization
MPP	Multi-photon polymerization
DLW	Direct laser writing
LIDT	Laser induced damage threshold
PI	Photoinitiator
IRG	Irgacure 369
FDTD	Finite-difference time-domain

# Introduction

Ever since the beginning of human history entire eras were defined according to the main technological advancement: bronze age, iron age, the industrial revolution, etc. In the wake of the XXI century, the 4th industrial revolution is in its full swing, blurring the lines between classical science and engineering fields [1]. As a result, an entirely new generation of functional device concepts emerged, combining the newest advances in cybernetics, biology, nanotechnologies, and other similar fields. However, in order to transfer such concepts from the idea to reality requires completely new manufacturing techniques that have to be precise down to nanometer-scale, offer easy on-demand tunability between various needed designs, and, finally, have throughput and cost ratio suitable for the mass production. For this reason, new ways to produce functional devices are being investigated, ranging from self-organization [2, 3] to ultra-advanced 3D printing (3DP) [4, 5].

Laser-based solutions stand out among other material processing techniques as being incredibly versatile and easy to adopt for most given applications. Indeed, it took just one year from the creation of the first operational laser [6] to full-on investigations of advanced nonlinear light-matter interactions [7]. Heavy industry was fast to grasp the potential of lasers as simple, relatively cheap, rapid, and contactless tools for manufacturing, adopting them into macro-manufacturing where they are unmatched up until today. However, most of these lasers are either continuous wave (CW) or operating at long pulse duration (millisecond (ms) or nanosecond (ns)) with sub-mm processing quality. While this is completely acceptable in heavy industry, modern nanotechnology-based devices cannot be produced using them.

High-beam quality ( $M^2 < 1.5$ ) short (sub-ns) pulse lasers opened entirely new possibilities in processing due to the possibility to exploit highly nonlinear and thermal aspects of light-matter interaction [8]. Usage of optical nonlinearities enabled to use of any wavelength for arbitrary material because there was no more necessity to optimize the process around the energy

introduction to the process *via* direct absorption [9]. Therefore, a lot simpler solid-state Nd:YAG laser could be used instead of highly complicated gas (CO<sub>2</sub> or excimer) lasers, as long as the intensity is high enough for nonlinear processes to take place. Additionally, such processes have intensity thresholds, thus are naturally confined only to the high-intensity regions of the laser irradiation, making them highly selective. Combined with pulse length  $\tau$  and spacing (*i.e.* repetition rate  $f$ ) induced control of thermal effects, it allowed achieving processing precision down to micrometer scale with throughput suitable for the industrial use.

Diode-pumped solid-state (DPSS) femtosecond (fs) lasers are the pinnacle of short pulse generation in visible and near-infrared wavelengths [10]. Due to the ultra-high intensities ( $\text{GW}/\text{cm}^2 <$ ) achievable with such radiation, nonlinear interactions are the primary channel of energy introduction to the material [8, 11]. At the same time, due to ultra-fast interaction timescale, heat dissipation from the light affected region can be made nominal, resulting in nearly material-independent ultra-high precision (down to nanometer scale) processing [8, 11]. Thus, this dissertation is dedicated to exploring and expanding the capabilities of using fs lasers for 3D laser lithography (3DLL).

Multi-photon polymerization (MPP) based femtosecond (fs) laser 3DLL has come a long way since its introduction in 1997 [12], becoming irreplaceable tool in diverse fields of science, including micromechanics [13, 14], biomedicine [15, 16], microfluidics [17, 18], microoptics [19, 20] and photonics [21, 22]. This is due to some inherent strengths of this technique, including the possibility to produce nearly unlimited 3D geometry [5, 23], a huge array of materials available [24, 25] and the capability to produce structures directly on functional substrates [26, 27]. Therefore, wide adoption of this technology in the industry is only a matter of improving throughput [28], mesoscale structure quality [29] and ease of use *via* advanced amortization of various functions of the system [30]. Here, we define mesoscale structures as ones having an overall size in the range from mm to cm yet retaining nano-micro features [5].

When it comes to throughput, one of the key parameters in direct laser writing (DLW) is the translation velocity at which the focal spot of a laser is positioned in relation to the sample or *vice versa*. The first consideration is that such a system has to support nm-level positioning accuracy. This severely limits possible candidates for usage in 3DLL. Sample positioning in relation to the laser beam can be realized using either piezo stages or linear positioning. While the high-precision low working field (up to

300 x 300 x 300  $\mu\text{m}^3$ ) piezo stages are inherently the most precise with controllable movement down to sub-nm level, they are also the slowest and have very limited (down to sub-mm) travel range in any direction. Linear stages are faster and grant nearly unlimited working field (up to tens of cm), yet can have inertia-related distortions if complex 3D shape at high translation velocities ( $v_t$ ) is produced. Alternatively, scanners can be used to move a focal point in relation to the sample. They have minimal inertia-related distortions but limit the size of the structure to the working field of an objective, which can be as small as  $\sim 100 \mu\text{m}$  for an objective with a numerical aperture (NA) above 1. For some applications, this is completely acceptable, as the average size of an object needed does not exceed the working field of an objective. However, if bigger structures are needed, they have to be produced in segments, bringing in so-called "stitching" between them [29, 30, 31, 32, 33]. This induces mechanical [29, 31] and optical [32, 33] defects rendering produced structures sub-par in comparison to what could be achieved without stitching.

Another way to control the throughput of 3D laser 3DLL is to manipulate the volume polymerized during the laser exposure. Indeed, when talking about 3DLL most of the time sub-diffraction limited resolution achieved *via* liquid immersion objectives with  $\text{NA} < 1$  is brought up, as it is the main enabler in fields such as photonics or micro-optics. On the other hand, lowering NA increases voxel size, especially in longitudinal direction [5, 23]. This effect is further accentuated by tuning the average laser power as this enables voxel size tuning with a single objective [34]. Both of these effects were exploited when relatively bigger structures with no need for sub-diffractive resolution, yet intricate internal geometries were manufactured [35, 36]. Therefore, tuning objective's NA and laser power is a simple and straightforward way to acquire the best combination between needed structure fidelity and fabrication throughput.

One of the possibilities to avoid stitching and acquire high throughput in 3DLL is to use synchronized movements of various positioning devices. Indeed, the idea of synchronizing different types of positioning (linear stages, galvo-scanners, polygon scanners, etc.) is not new and was exploited in the past [37]. Galvo-scanner and linear stage synchronization is especially interesting in the 3DLL case, as both of these positioning systems are already successfully used for nanopolymerization and are prevalent in most fabrication setups. After synchronization, it should yield scanner-level translation velocity (up to cm/s) and linear stage enabled movement distances (up to tens of cm) with relevant NAs (up to 1.4). Such a method was used to

some extent over the years in 3DLL [15]. However, there is very little understanding on how much translation velocity can be pushed with high NA objectives, and does it in any way interfere with structuring quality and/or resolution.

The next consideration associated with the spread of 3DLL, especially when it comes to micro-optics and nanophotonics, is extremely limited empirical knowledge about the optical resilience of laser made structures. Indeed, despite the huge diversity of 3D micro-optical structures that were made using this technique, most of them were applied to imaging or light shaping techniques. There are no successful attempts to implement them in areas such as communications or laser engineering. While there were some investigations associated with the laser structurable materials [38], they were done in accordance to standard ISO testing protocols, meaning that the tested materials were not cross-linked in multiphoton fashion and structures themselves were not truly 3D. Thus, there is a distinct lack of laser-induced damage threshold (LIDT) in laser-made true 3D structures. This is a huge hindrance as high-resolution complex 3D structures were shown to be a powerful tool for photonics.

## Goal of the dissertation

The goal of the dissertation was to investigate to what extent galvo-scanner and linear stage synchronization can improve the throughput of 3DLL towards mesoscale structure fabrication and are there any additional considerations when using such a method for nanopolymerization. The second goal was tied with a better understanding of photoinitiator (PI) influence on 3DLL structuring as elimination of PI should potentially benefit the final structure's biocompatibility and optical resiliency. This ties to the third goal of this work - create a methodology for experimental LIDT investigation of 3DLL made structures and after performing qualitative and quantitative investigation determine what are the tendencies of LIDT in different material and which material is the most resilient.

## Tasks of the work

To reach the goals of the dissertation the following tasks were set:

1. Evaluate the possibility to use the linear stage and galvo-scanner synchronization and variable NA for 3DLL combining both high resolution and maximal throughput.
2. Deduce capabilities and limitations of PI-free structuring of hybrid organic-inorganic photopolymers using 3DLL.
3. Perform qualitative and quantitative LIDT investigation of 3DLL made objects.

## Novelty and importance of the work

The novelty of this work lies in the capabilities to manufacture 3D mesoscale objects *via* 3DLL with increased throughput, pushing the technology closer to industrial use. While synchronizations and/or combinations of various positioning systems were employed in the past, there is a distinct lack of understanding to what extent this can be used for high-resolution 3D polymerization. Furthermore, while PI-free structuring was demonstrated in previous works, the structuring peculiarities and material properties had a minimal comparison to standard photosensitized materials. Finally, in this work novel, LIDT measurement strategies for 3DLL made structures were developed laying the foundation for future works in this area.

## Practical impact

Presented work has immense practical implications. First off, developed meso-printing strategies become the basis for novel commercial fs laser-based polymerization workstation. Pure material structuring is extremely important for the development of high-resiliency micro-optics. Finally, created LIDT evaluation/measurement methods go above and beyond standard ISO characterization, potentially inspiring new standards in this area in the future.

## Key statements for defense

1. 3DLL employing linear stages synchronized with galvo-scanners allows manufacturing of 3D structures with the sub-diffraction limited resolution at galvo-scanner level rates (up to cm/s) over mesoscopic spatial dimensions (0.1 - 10 mm).
2. Non-photosensitized hybrid organic-inorganic photopolymer SZ2080 can be 3D structured with parameters similar to those needed for photosensitized counterpart (difference in  $P$  at same  $v$  is within  $\sim$ tens of %); the achieved mechanical properties and surface roughness of resulting microstructures are comparable (RMS < 10 nm) with and without the use of photosensitizer.
3. LIDT of 3DLL made microstructures varies for different geometries (bulk, woodpile, microlens) made from the same polymer; for all geometries and tested materials, hybrid organic-inorganic photopolymers are more optically resilient compared to photosensitized organic photopolymers with similar absorption properties.

## Approbation of the research results

This section presents the lists of papers and conferences related to the dissertation.

## List of papers related to the dissertation

- I L. Jonušauskas, S. Rekštytė and M. Malinauskas, Laser fabrication of 3D trans-micro-scale structures by varying focusing conditions, Opt. Eng. **53**(12), 125102 (2014).

- II L. Jonušauskas, D. Gailevičius, L. Mikoliūnaitė, D. Sakalauskas, S. Šakirzanovas, S. Juodkakis and M. Malinauskas, Optically clear and resilient free-form  $\mu$ -optics 3D-printed via ultrafast laser lithography, *Materials*, **10**(1), 12 (2017).
- III L. Jonušauskas, S. Juodkakis and M. Malinauskas, Optical 3D printing: bridging the gaps in the mesoscale, *J. Opt.* **20**(5), 053001 (2018).
- IV L. Jonušauskas, D. Gailevičius, S. Rekštytė, T. Baldacchini, S. Juodkakis and M. Malinauskas, Mesoscale laser 3D printing, *Opt. Express* **27**(11), 15205-15221 (2019).
- V A. Butkutė, L. Čekanavičius, G. Rimšelis, D. Gailevičius, V. Mizeikis, A. Melninkaitis, T. Baldacchini, L. Jonušauskas and M. Malinauskas, Optical damage thresholds of microstructures made by laser three-dimensional nanolithography, *Opt. Lett.* **45**(1), 13-16 (2019).

## List of conference contributions directly related to the dissertation

- I L. Jonušauskas, D. Gailevičius, R. Gadonas, M. Malinauskas 3D polymeric microlenses in high intensity light, Merging Micro- and Nano-Optics: 3D Printing for Advanced and Functional Optics, Bad Honnef, Germany, 2017.
- II L. Jonušauskas, M. Malinauskas, Realisation of optically resilient fiber tip 3D microoptics, SPIE Optics + Optoelectronics, Prague, Czech Republic, 2017. (Won best student paper award)
- III L. Jonušauskas, D. Gailevičius, R. Gadonas, A. Melninkaitis, M. Malinauskas, The optical resiliency of 3D nanolithography produced microstructures to intense irradiation, CLEO/Europe-EQEC 2017, Munich, Germany, 2017.
- IV L. Jonušauskas, Mesoscale hybrid fabrication: a magic bullet in today's laser material processing, ad3pa 2017, Dresden, Germany, 2017. (Invited talk)
- V L. Jonušauskas, D. Gailevičius, S. Rekštytė, M. Malinauskas, Fabrication of 3D meso-scale structures out of non-photosensitized polymers via femtosecond laser lithography, 42nd Lithuanian Conference of physics, Vilnius, Lithuania, 2017.



- VI L. Jonušauskas, D. Gailevičius, S. Rekštytė, S. Juodkazis, M. Malinauskas, Write-on-the-fly: synchronization of linear stages and galvanoscanners for mesoscale 3D optical printing, SPIE Australasia, Melbourne, Australia, 2017.
- VII L. Jonušauskas, G. Rimšelis, D. Gailevičius, R. Gadonas, A. Melninkaitis, M. Malinauskas, The optical damage threshold of 3D nanolithography produced microstructures under intense femtosecond irradiation, SPIE Photonics West, San Francisco, USA, 2018.
- VIII L. Jonušauskas, L. Čekanavičius, A. Butkutė, M. Malinauskas, Quantitative laser induced damage threshold investigation of femtosecond laser lithography produced 3D structures, LPM 2018, Edinburgh, UK, 2018.
- IX L. Jonušauskas, D. Gailevičius, T. Baravykas, S. Rekštytė, S. Juodkazis, M. Malinauskas, Multi-scale rapid laser 3D printing, LPM 2018, Edinburgh, UK, 2018.
- X L. Jonušauskas, T. Baravykas, D. Gailevičius, S. Rekštytė, S. Juodkazis, M. Malinauskas, Continuous 3D Writing for Stitch-Free 3D Meso-Scale Laser Printing, ICPEPA 2018, Vilnius, Lithuania, 2018.
- XI L. Jonušauskas, L. Čekanavičius, A. Butkutė, M. Malinauskas, Qualitative and Quantitative Investigation of Free-Form fs Laser Made Structures to Intense Ultrafast Laser Radiation, ICPEPA 2018, Vilnius, Lithuania, 2018.
- XII L. Jonušauskas, Sub-micro hybrid subtractive-additive 3D fabrication of medical devices using femtosecond laser: towards widespread solution, Life Sciences Baltics 2018, Vilnius, Lithuania, 2018.
- XIII L. Jonušauskas, Hybrid subtractive-additive femtosecond laser manufacturing of functional 3D structures: towards industrial applications, ad3pa 2018, Dresden, Germany, 2018.
- XIV L. Jonušauskas, T. Baravykas, D. Gailevičius, S. Rekštytė, S. Juodkazis, M. Malinauskas, Linear-stage and galvo-scanner synchronization for rapid fabrication of 3D mesoscale structures via femtosecond laser direct writing, SPIE Photonics West, San Francisco, USA, 2019.

- XV L. Jonušauskas, L. Čekanavičius, A. Butkutė, M. Malinauskas, Femtosecond laser induced damage threshold (LIDT) of 3D nanolithography made micro- and nano-optical elements, SPIE Photonics West, San Francisco, USA, 2019.

## List of other papers in reviewed literature

- I M. Malinauskas, G. Kiršanskė, S. Rekštytė, T. Jonavičius, E. Kaziulionytė, L. Jonušauskas, A. Žukauskas, R. Gadonas and A. Piskarskas, Nanophotonic lithography: a versatile tool for manufacturing functional three dimensional micro-/nano-objects, *Lith. J. Phys.* **2**(4), 312–326 (2012).
- II L. Jonušauskas, E. Skliutas, S. Butkus and M. Malinauskas, Custom on demand 3D printing of functional microstructures, *Lith. J. Phys.* **5**(3), 227-236 (2015).
- III L. Jonušauskas, M. Lau, P. Gruber, B. Gökce, S. Barcikowski, M. Malinauskas and A. Ovsianikov, Plasmon assisted 3D microstructuring of gold nanoparticle-doped polymers, *Nanotechnology* **27**(15), 154001 (2016).
- IV E. Garškaitė, L. Alinauskas, M. Drienovsky, J. Krajcovic, R. Cicka, M. Palcut, L. Jonušauskas, M. Malinauskas, Ž. Stankevičiūtė and A. Kareiva, Fabrication of a composite of nanocrystalline carbonated hydroxyapatite (cHAP) with polylactic acid (PLA) and its surface topographical structuring with direct laser writing (DLW), *RSC Adv.* **6**(76), 72733-72743 (2016).
- V L. Jonušauskas, S. Rekštytė, R. Buividas, S. Butkus, R. Gadonas, S. Juodkazis and M. Malinauskas, Hybrid subtractive-additive-welding microfabrication for lab-on-chip applications via single amplified femtosecond laser source, *Opt. Eng.* **56**(9), 094108 (2017).
- VI E. Skliutas, S. Kašetaitė, L. Jonušauskas, J. Ostrauskaite and M. Malinauskas, Photosensitive naturally derived resins toward optical 3-D printing, *Opt. Eng.* **57**(4), 041412 (2018).
- VII L. Jonušauskas, D. Mackevičiūtė, G. Kontenis and V. Purlys, Femtosecond lasers: the ultimate tool for high-precision 3D manufacturing, *Adv. Opt. Tech.* **8**(3-4), 241-251 (2019).

- VIII L. Jonušauskas, T. Baravykas, D. Andrijec, T. Gadišauskas, V. Purlys, Stitchless support-free 3D printing of free-form micromechanical structures with feature size on-demand, *Sci. Rep.* **9**, 17533 (2019).
- IX G. Merkininkaitė, D. Gailevičius, S. Šakirzanovas, and L. Jonušauskas, Polymers for Regenerative Medicine Structures Made via Multiphoton 3D Lithography, *Int. J. Polym. Sci.* **2019**, 3403548 (2019).
- X B. Sanchez-Padilla, L. Jonušauskas, M. Malinauskas, R. Wunenburger, and E. Brasselet, Direct mechanical detection and measurement of wave-matter orbital angular momentum transfer by non-dissipative vortex mode conversion, *Phys. Rev. Lett.* **123**, 244301 (2019).
- XI G. Nemickas, G. Kontenis, A. Žemaitis, V. Purlys, and L. Jonušauskas, Industrial-grade processing of metal surfaces via femtosecond laser, *J. Phys. Photon.* **2**, 041004 (2020).
- XII L. Bakhchova, L. Jonušauskas, D. Andrijec, M. Kurachkina, T. Baravykas, A. Eremin, and Ulrike Steinmann, Femtosecond Laser-Based Integration of Nano-Membranes into Organ-on-a-Chip Systems, *Materials* **13**(14), 3076 (2020).
- XIII G. Kontenis, D. Gailevičius, L. Jonušauskas, and V. Purlys, Dynamic aberration correction *via* spatial light modulator (SLM) for femtosecond direct laser writing: towards spherical voxels, *Opt Express* **28**(19), 27850-27864 (2020).
- XIV A. Maruška, T. Drevinskas, M. Stankevičius, K. Bimbiraitė-Survilienė, V. Kaškonienė, L. Jonušauskas, R. Gadonas, S. Nilsson, and O. Kornyšova, Single-chip based contactless conductivity detection system for multi-channel separations, *Anal. Methods* **13**, 141-146 (2021).

## Contribution of the Authors

The vast majority of work presented in the dissertation was performed by the author. This includes literature review, formulation of hypothesis, preparation for experiments, their execution, measurement, and data analysis. Nevertheless, several colleagues also had substantial contribution to some aspects or parts of the presented work:

- **Dr. Mangirdas Malinauskas** - supervisor of the work, who suggested and consulted on presented research directions and topics.

- **Prof. Dr. Saulius Juodkazis** - suggested physical interpretation for some of the presented experimental results.
- **Dr. Andrius Melninkaitis** - consulted on LIDT measurement methodology, result interpretation, and error calculation.
- **Dr. Vytautas Purlys** - extensive consultations regarding the setup and usage of laser fabrication systems.
- **Tomas Baravykas** - prepared some of the 3D models for the presented mesoscale structures, theoretical energy dose calculation when translation velocity is changed.
- **Agnė Butkutė** - fabrication and LIDT testing of photonic crystals, theoretical calculation of their photonic properties.
- **Laurynas Čekanavičius** - LIDT measurement of bulk laser made structures.

## Layout of the dissertation

The dissertation is dispersed into five distinct parts. The first part deals with the general introduction and theory of the field. The second one discusses the experimental part of the whole work. The last three sections are dedicated to the experimental results and their evaluation.

# 1. Literature Review

Due to immense technological progress, novel manufacturing techniques emerged in the last few decades. One of the most prominent ones is additive manufacturing and processing using fs lasers. While this dissertation is directed towards expanding the capabilities of 3DLL and investigating properties of printed structures, it is important to understand in what context the technology is developed. Thus, during the literature review, we will discuss other additive manufacturing techniques as well as fs-laser material processing peculiarities. This will allow establishing proper context where the motivation for this work comes from.

## 1.1. Additive *vs* Subtractive Manufacturing

In essence, all manufacturing techniques can be labeled as subtractive, additive, joining, dividing, and transformative [39]. Due to their popularity, for the sake of this dissertation, let's consider subtractive and additive cases. In subtractive manufacturing, the material is removed from the initial slab revealing the structure [Fig. 1.1 (a)]. The advantage of such a manufacturing strategy is that it can be relatively simple and well-suited for the mass production of virtually any material (or workpiece). While it can produce simple 3D structures, it is limited in terms of objects with an intricate internal geometry. Also, the material removed during fabrication is a technological waste that has to be somehow removed from the manufacturing setup and either thrown away or recycled adding to the overall cost of the product [40]. Currently, the most advanced kinds of subtractive fabrication are mechanical machining [41], laser cutting [42, 43, 44] and selective laser etching [45, 46, 47].

In the additive case, the object is created by adding the material to the structure until it is finished [Fig. 1.1 (b)]. The main advantage of additive manufacturing is that there is a lot more freedom in the internal geometry of the structure/pattern enabling true 3D fabrication. The amount of waste

is also greatly reduced [40]. What is more, the general handling of it is a lot easier, as it is either dissolved as unused resin in lithographic methods or can be extracted for further use in melting/sintering based methods. For a long time, one of the most prominent additive manufacturing approaches was casting, providing a capability for the fast creation of intricate shapes, with the main difficulties being a fabrication of initial mold and finding the right substances that could be turned from a liquid to solid under controlled parameters. However, some limitations for complex 3D geometries still remain.

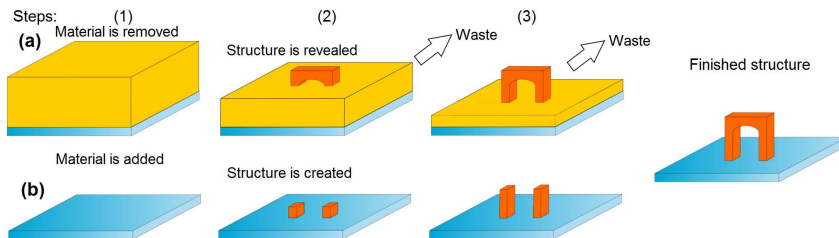


Figure 1.1: Schematics of subtractive (a) and additive (b) manufacturing of a 3D structure. In the subtractive case, the material is removed from the initial slab until the final structure is revealed. Technological waste is unavoidable in this process. Furthermore, complex internal 3D structures are only possible *via* multiple technological steps. It is not the case in additive manufacturing as the structure is created by adding the material until the object is finished.

3DP represents an approach in manufacturing based on the idea of an object being produced by adding the material to the structure until it is finished, hence additive manufacturing. In most cases, it is done in a layer-by-layer fashion with some works exploiting other strategies as well [48, 49]. Complex shapes can be achieved in this manner, including various arches or woodpiles [50, 51]. Depending on how 3DP is realized, this can be a very simple process from the point of view of the user as it provides structure in one or two fabrication steps, with the minimal workload to the 3DP operator. It is possible due to the high degree of automation inherent in most 3DP techniques. Model for the structure itself can be provided as a separate 3D file (mostly in STL format) [52]. For this reason, one of the first applications of 3DP was in rapid prototyping, as the time needed to turn the digital model into a physical object is minimal. Furthermore, to date, almost any material was structured *via* 3DP, including paper [53], food [54],

plastics [55], glasses [56], metals [57], wood [58], ceramics [59] or even living cells [60]. One of the main disadvantages of 3DP involves the necessity to compromise between the fabrication resolution and throughput. Indeed, as the fabrication is based on the consecutive creation of different parts of the object, the higher the writing resolution the smaller volume is added to the structure in each step and *vice versa* [61, 62]. Although there are attempts to amend this problem and increase the efficiency of 3DP [63, 64, 65], so far it is considered that 3DP is a technology best suited for prototyping or small scale production. Nevertheless, 3DP is a fast-growing industry since it can cope with otherwise unachievable structural complexity [66].

## 1.2. General Overview of Optical 3D Printing

O3DP can be defined as a kind of 3DP that uses a light source (both coherent and incoherent) as the main channel for introducing energy needed for the fabrication. The attractiveness of the light as an energy source is dictated by the possibility to precisely control it spatiotemporally. This assures maximal selectivity and quality during the structuring. Light delivery is contactless, allowing to induce changes in the material without physical contact, assuring that there will be minimal contamination in the final product from the machining tools. Light can be generated by many different sources, both incoherent and coherent. Paired with the high flexibility of optical system design, this enables a plethora of different configurations in O3DP to explore. With such a definition, stereolithographic printing (SLA), selective laser sintering/melting (SLS/SLM), and laser-induced forward transfer (LIFT) structuring can be considered as different kinds of O3DP with some distinct features, advantages, limitations, and subsequent perspectives.

In O3DP, the light is directed to the substance that, in most cases, is sensitive to the wavelength generated by the light source. During the irradiation/exposure introduced energy induces either chemical changes in the material or phase transitions, i.e., melt, evaporate or turn into plasma. As these regimes differ heavily, a lot of substances can be structured with at least one of these methods, making O3DP very versatile when it comes to the choice of the material. Overall, different kinds of O3DP in most cases are separated from each other by the type of interaction [Fig. 1.2].

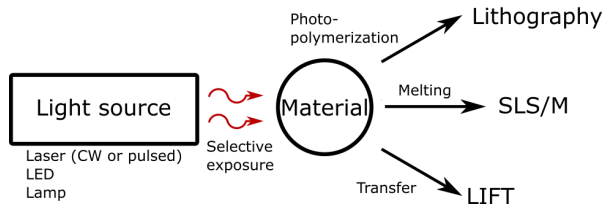


Figure 1.2: Basic principles of different approaches of O3DP. The light source is used to introduce energy to specified regions of the sample resulting in photochemical reactions, melting, or evaporation. It is then exploited for additive 3D manufacturing.

### 1.2.1. Various Optical 3D Printing Techniques

In the simplest case, lithographic O3DP or SLA operates by the principle that photosensitive monomer mixture (resin) is exposed to the light source that has sufficient one photon energy to induce the polymerization reaction in the material. Acrylate and epoxy-based resins dominate this technology [67, 68]. Although a visible-light-induced polymerization is possible [69], in most cases, near-UV radiation is utilized. By selectively exposing the material to the light, a 2D shape (layer) is created. The 3D structure is produced by stacking 2D layers on top of each other. After this, the operation sample is submerged into a solvent that washes away the unexposed material. In the standard case, the achievable feature sizes can be between tens to hundreds of micrometers [70].

The required 2D pattern of the material can be achieved by raster scanning of the focused light. Exposure can be performed from the top of the reservoir of a resin and by lowering the structure into it after each layer is produced. After each exposure, a blade can be used to make sure that the new resin layer is of the correct thickness [Fig. 1.3 (a)] [71]. This limits the maximum achievable height of an object to that of the reservoir's depth and also requires an excessive amount of material in it. Therefore, a considerably more popular approach is to expose resin from the bottom through the transparent window [Fig. 1.3 (b)]. The window is made out of oxygen permeable material (for instance polydimethylsiloxane PDMS or silicone), thus there is no adhesion between it and the formed structure as the oxygen quenches polymerization of common lithographic resins and forms a "dead zone" over the area of the window. The correct polymerized layer height is guaranteed by moving the resin tank from side to side after each exposure. Overall, this greatly reduces the height restrictions and allows to have a



relatively small amount of photo-active resin in the reservoir [72].

By using modern galvo-scanners, the translation velocity of raster scanning can reach several m/s [72], yet it is still a relatively slow fabrication method in terms of volume per time. It is the result of the point-by-point fabrication nature of SLA. One of the newest developments in the field is to expose the material to the projected image of an entire layer, therefore moving from point-by-point fabrication to plane-by-plane structuring/stacking [Fig. 1.3 (c)] [73]. It significantly enhances the fabrication throughput. The increase in the complexity of the optical components and higher requirements for the beam quality are the disadvantages of this approach.

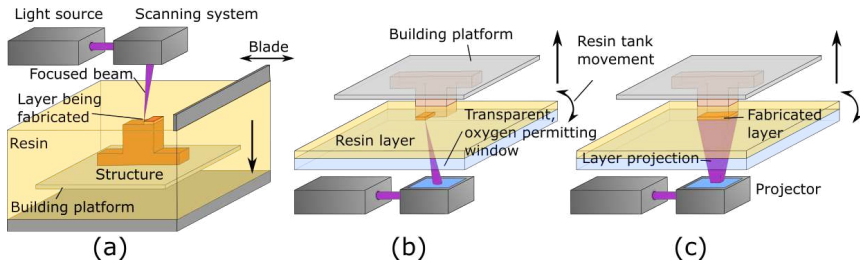


Figure 1.3: Realizations of lithographic 3D printing: (a) - platform and structure are moving down inside a resin tank (black arrow), exposure is carried out from the top, (b) - the structure is being pulled out of the resin, exposure is from the bottom through the oxygen-permitting window, (c) - based on a digital light projection. (a) and (b) represent point-by-point structuring while (c) - layer-by-layer.

It is worth noting that photopolymerization can be induced by multi-photon absorption (MPA) also, opening entirely new possibilities in ultra-precise O3PD. This technology is still considered lithography, yet differs heavily from standard SLA and will be discussed in great detail later in the work.

Modern laser sources allow achieving focused light intensities high enough to melt any material. Therefore, SLM or SLS was applied for O3DP as well [74]. For simplicity, we will use these terms as synonyms in this work, although there are some differences between these regimes [74]. Fine powder (particle size in a range of  $\sim 10\text{-}150\ \mu\text{m}$  [75]) of the required material is spread to form a thin ( $\geq 20\ \mu\text{m}$  [74]) layer that could later be selectively melted by the focused laser beam. After that, a new fine overcoat of particles is applied on top of it, and the process is repeated [Fig. 1.4]. Depending

on the peculiarities of the exact material and technological variations, other post-processing steps, such as development or post-bake, might follow. The final size of the structure can reach up to tens-of-centimeters in the overall structure [76] size while retaining a  $\sim \mu\text{m}$  [74] level surface smoothness.

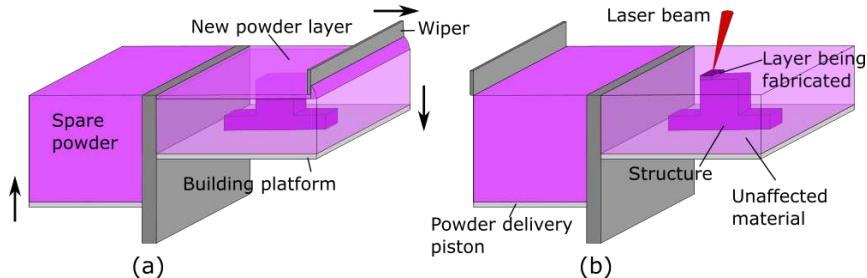


Figure 1.4: Visualization of selective laser sintering/melting O3DP. The powder delivery piston is pushing spare material up, while the building platform moves down (black arrows). The wiper then distributes a new powder layer on an already produced structure (a). After that laser is used to sinter/melt powder creating a new structure layer (b) and the process is continued until the entire structure is produced.

One of the main advantages of sintering is a broad range of materials that can be structured this way. Polymers, both amorphous and semi-crystalline, were processed with this technology [75, 77]. Metal 3DP is also possible [78, 79]. Direct and indirect ceramic bonding was shown too [80, 81]. Composite materials, combining polymers and ceramics is another interesting direction [82, 83], as the final characteristics and functionality of the structure can be tuned *via* change of properties and composition of the source material. It is important to stress that some substances are easier to process than others, and, in most cases, some specific parameters have to be used to achieve the best possible result and overcome shortcomings such as structure shrinkage, brittleness, or porosity [84, 85].

While lithography and sintering are based on the idea of locally changing the material, the laser also can induce physical transfer from the donor sample to the recipient structure [Fig. 1.5] [86]. In practice, LIFT has many different variations, using pulsed [87] or CW lasers [88], a donor can use some intermediate absorbing layer [89], the transfer can also be applied not only to homogeneous solid materials but also to liquid droplets [90] or multi-material structures [87, 91, 92] that can sometimes act as functional devices. A reversed case is also possible - laser then induces backward (in

relation to the laser beam propagation direction) transfer [93], yet it is a lot less common.

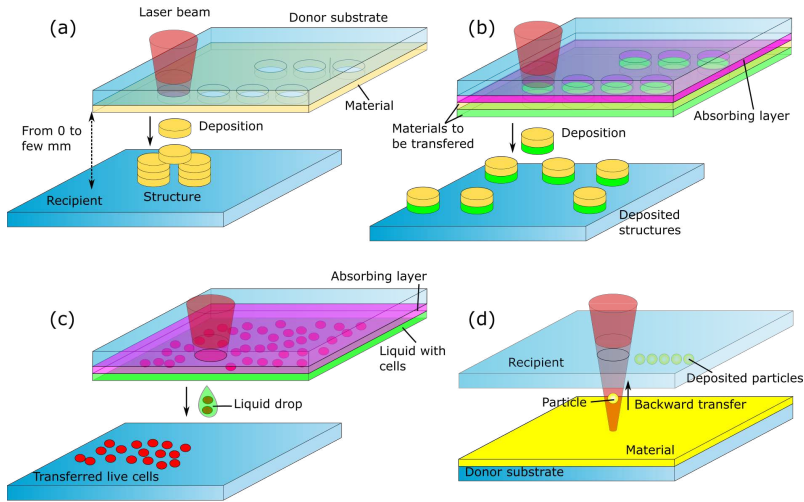


Figure 1.5: Variations LIFT types. (a) - LIFT printing of paste voxels (volume elements) allowing a 3D fabrication of hollow structures. (b) Multi-layered LIFT. The energy of the laser is absorbed in a special layer, enabling the deposition of multiple unaffected layers of material. The deposited layers can act as the devices (for instance, LED pixels) or one of the layers can act as an adhesion agent, while the other performs the function. (c) - Printing of cells out of a liquid suspension. As the absorbing layer propels the liquid ink with cells without direct light interaction with a living bio-component, it is possible to print live cells without damage to their integrity nor DNA. After the process, cells can stay in a liquid or adhere to the functionalized substrate. (d) The laser light interacts with the material and forces a particle to be deposited in the opposite direction to the beam propagation (hence, the name LIBT).

In contrast to all other O3DP technologies, material out of which fabrication is carried out is minimally or entirely unaffected by the incident light during LIFT. Thus, metals [94, 95], polymers [96, 87] and living cells can be transferred [89, 97], paving the way for true 3DP of organs. Also, the LIFT resolution spans from tens on nm [98] to hundreds [99] of  $\mu\text{m}$  opening a possibility to print functional plasmonic, electronic, solar harvesting, light-emitting devices. Additionally, in the lithography or sintering, if a closed part of the structure is left unstructured, it is still full of unprocessed initial

material. Therefore, openings in the final object are required for removal of unaffected material *via* post-processing steps [100]). In contrast, during LIFT, the material is constantly added to the structure and true empty gaps inside the object/workpiece can be realized if hard material is used [101].

LIFT is currently under active investigation. Pulse duration [102, 103] and fast-switching between materials [87, 104] and overall printing speed are just several challenges that are being addressed right now. The final goal for this technology is the capability to print at nm resolution centimeter-sized structures (i.e. in mesoscale) with the possibility to choose any material on-the-fly.

### 1.2.2. Applications of Macro-3D Printing

3DP in general opens new prospects in terms of structures with specified and function-orientated properties that could not be achieved with other technologies. Currently, 3DP does not offer throughput high enough for the mass production required in the industry. However, the freedom of design coupled with a relatively short time from an idea to the physical object fabrication and complexity embracing the character of the method enables prototyping and small-scale production capabilities unmatched by basically any other modern fabrication technique.

In terms of scientific applications, the rapid expansion of the lab-on-chip (LOC) type technologies seems to benefit greatly from the design freedom offered by the O3DP. Additive manufacturing can be used in many different ways here, including fabrication of molding tools [105], manufacturing of some parts of the LOC systems [106], or entire functional chips [107]. In most cases, LOC systems are relatively complex and function-orientated [108, 109], thus design freedom and the possibility to test a relatively high number of designs quickly is both highly beneficial and required. Also, one such system can be produced using just a very basic 3D printer and a few relatively simple technological steps. Thus, the price of one LOC system can be as little as 1 Euro [107], assuring a faster than ever spread of LOC devices. This explains a fast uptake of O3DP by R&D teams in companies and academic laboratories.

The O3DP is also starting a revolution in patient-oriented regenerative medicine. Currently, most medical practices are based on highly standardized methods, offering little in terms of adaptability to each patient and case. The O3DP allows creating various implants specially tailored for each person capitalizing on all the main strengths of O3DP. Exam-

ples include various bone-replacing implants [76, 79] or scaffolds for stem cell growth [110, 111, 112]. If the first example is a well-known approach adapted even at a commercial level, regenerative medicine based on scaffolds seeded with patient's stem cells is a relatively new method, benefiting from the fact that some O3DP processable materials can be biodegradable [112]. It can be considered that 3D printed replacements for various body parts will become a standard procedure in the treatment of various diseases or traumas. O3DP allows control of mechanical strength of the fabricated parts matching their intended function and environment by controlling the porosity of constituent materials.

In terms of industrial applications, O3DP serves as means for rapid prototyping, as it was intended at the very infancy of the technology [113, 114]. However, as the manufacturing throughput grows and material variety is constantly increasing, more common direct fabrication of functional 3D structures emerges. Complex functional parts of exotic materials recently are of the great interest [53, 56]. Because of unmatched design flexibility, plasmonic or microelectronic systems created using LIFT are also considered [88, 115, 116]. Application of O3DP in optical component fabrication is another field [117, 118], as it promises a relatively simple way to produce free-form objects for light shaping. All in all, while most of these approaches are in a testing phase, there is no doubt that O3DP will become a standard industrial tool in the near future.

### **1.2.3. Perspectives of the Technology**

O3DP already passed the infancy stage and found its way into scientific labs and industrial facilities. However, this success only fuels further developments in this field, as there are many areas where these technologies could still be improved.

Flexibility in terms of design complexity is one of the main advantages of O3DP. It is achieved partially by sacrificing throughput of fabrication. Indeed, point-by-point structuring by a focused laser beam is a relatively slow process, even if modern scanning systems are applied. A possible solution to this problem would be to project the entire layer image in one exposure and forming/building structures in a layer-by-layer fashion. This method is already available in SLA [73]. However, as SLM/SLS is more sensitive to spatial beam distribution [119, 120], this approach is not common there. Experiments in LIFT are underway as spatial light shaping allows to achieve a complex-geometry printing with only one exposure [121, 122].

Materials are another area that is currently gaining substantial attention. From the first glance, by combining all the existing O3DP technologies, it should be possible to process virtually any material. However, in most cases, a combination of specific material and the technology determines peculiarities of fabrication, which can induce some limitations to the final structures or how easily they could be produced. Therefore, the search for new ways to process existing industrial materials or entirely new substances is constantly active. For instance, optical printing of live cells of various types is a promising prospect in medicine [89, 97]. Biologically derived polymers should provide a way to create structures out of renewable and potentially biodegradable plastics [123, 124]. Lithographic printing of hybrid polymers could yield highly complex and resistant ceramic structures, as the organic part (required for lithography-based manufacturing) is removed in thermal post-processing step [125, 126]. These examples show that various novel ideas combined with the newest advances in material science could allow an entirely new wave of 3D-printed objects made out of previously incompatible and/or new materials.

## **1.3. Femtosecond Lasers in Material Processing**

### **1.3.1. Interaction Between Materials and Ultrashort Pulses**

In a very generalized case, the material can either reflect, transmit, scatter or absorb light. In the last case, energy is introduced to the material. If energy is sufficiently high, it can induce various changes in the substance. Selective exposure of the material with a sufficient amount of laser light, in order to induce desired changes in the medium, is the main idea behind laser material processing.

Nonlinear processes were discovered almost immediately after the creation of the laser [7]. Nevertheless, when lasers were applied for material processing main pathway for energy introduction to the sample was linear absorption. In that case, photons of energy matching or slightly exceeding bandgap energy of the material  $E_g$  are used to excite material and induce melting or evaporation. As photon energy  $E_p$  is dependant on emission wavelength  $\lambda$  as  $E_p = hc/\lambda$ , appropriate  $\lambda$  has to be used for any material. Therefore, various materials required different lasers to be used in fabrica-

tion. For instance, CO<sub>2</sub> lasers were widely adopted for metal cutting [127], while Excimer lasers became popular in polymer processing [128].

With the advances in laser technology, pulsed lasers became widely available. First, Q-switched lasers allowed to reduce pulse duration to  $\sim$ ns range [129]. Then, the introduction of mode synchronization pushed the limit of the pulse duration to almost one optical cycle [130]. The main advantage of pulsed laser operation is a sharp increase in the peak power  $P_p$ , which can be calculated as:

$$P_p = \frac{P}{f\tau}, \quad (1.1)$$

here  $P$  is the average laser power and  $\tau$  is the pulse duration and  $f$  is the laser pulse repetition rate. Thus,  $P_p$  increases as  $\tau$  becomes shorter. For instance, if a laser  $P = 10$  W is operating at  $\tau_1 = 30$  ns and  $f = 1$  kHz,  $P_{p1} = 330$  kW. However, in the case of a  $\tau_2 = 300$  fs and  $f = 1$  kHz laser, the  $P_{p2} = 33.33$  GW. It is obvious that decreasing  $\tau$  increases  $P_p$  by the same order of magnitude.

Such a sharp increase in  $P_p$  can be paired with focusing optics to achieve very high light intensities  $I$  in the focal point. Indeed, in the most general case,  $I$  can be calculated as  $P$  to the laser spot:

$$I = \frac{P}{\pi w_0^2}, \quad (1.2)$$

where  $w_0$  is the laser spot radius. Considering Gaussian light distribution  $w_0 = 0.61\text{NA}/\lambda$ . Thus, peak  $I$  in the middle of a Gaussian laser spot can be calculated as:

$$I_0 = \frac{2P}{fw_0^2\pi\tau}, \quad (1.3)$$

$I$  is proportional to the square of the electric field of the light. High  $I$  values enable nonlinear light and matter interactions. In the case of a transparent medium, two distinct nonlinear light-matter interaction regimes can be deduced: multiphoton and tunneling ionization. Which regime is dominating shows the Keldysh parameter [131]:

$$\gamma = \frac{\omega}{e} \sqrt{\frac{\epsilon_0 c m n E_g}{I}}, \quad (1.4)$$

here  $\omega$  is the frequency of the light,  $e$  - electron charge,  $\epsilon_0$  - dielectric permittivity,  $c$  - speed of light,  $n$  - refractive index of the material. It is considered that if  $\gamma \ll 1$ , the tunneling ionization is a dominant process.

In that case, relatively slow oscillations of the electric field of the light severely perturb the energy level system of material for a long enough time for an electron to tunnel from the valence band to the conduction band. Higher  $\omega$  results in shorter perturbations to the electron system, which minimizes the possibility for electron tunneling. Therefore, when  $\gamma \gg 1$ , the dominant process is a multiphoton excitation. It is important to note that the probability of multiphoton ionization  $p$  is highly dependant on  $I$  and  $E_g$ :

$$p = \sigma_k I^k, \quad (1.5)$$

with  $k$  showing the number of photons, so  $kE_p \geq E_g$  - a condition needed for MPA. Also,  $p$  is diminishing as  $k$  increases, meaning that lower-order nonlinearities (for instance, TPA) has a higher probability than the higher-order process. Contrary to MPA, the probability of tunneling ionization is a lot less dependant on  $E_g$  of the material [131, 132]. It is important to note that for some materials and experimental conditions (for example, fused silica and 1030 nm laser radiation)  $\gamma \sim 1$ , which denotes that there is no dominant process, resulting in a comparable probability of multiphoton, and tunneling ionization.

Finally, an avalanche ionization has to be discussed as well. An electron in the conduction band can interact with the electric field of light by being accelerated, increasing the kinetic energy  $E_k$ . If  $E_k$  exceeds the  $E_g$  in the time needed for an electron to reach another atom, it can transfer its energy to another electron, thus exciting it to the conduction band [133]. This results in the ever-increasing concentration of excited electrons  $n(t)$  over time  $t$  which follows exponential growth law:

$$n(t) = n_0 e^{\beta t}, \quad (1.6)$$

where  $n_0$  is the initial electron concentration and  $\beta$  is avalanche ionization rate. Due to the time needed for electron acceleration, this process becomes noticeable when pulse duration starts to exceed 100 fs. However, when the pulse duration is increased to hundreds of fs, the range at which most of the modern amplified laser systems operate, it can become comparable or even exceed multiphoton ionization by the number of excited electrons. Also, there have to be some seed electrons for this process to occur. These could be either free electrons occurring due to impurities in the material or excited *via* other nonlinear processes [133, 134]. The efficiency of the process decreases with the shorter wavelengths (especially below 1  $\mu\text{m}$ ) [135] and



can be considered to scale linearly with  $I$  [135, 136].

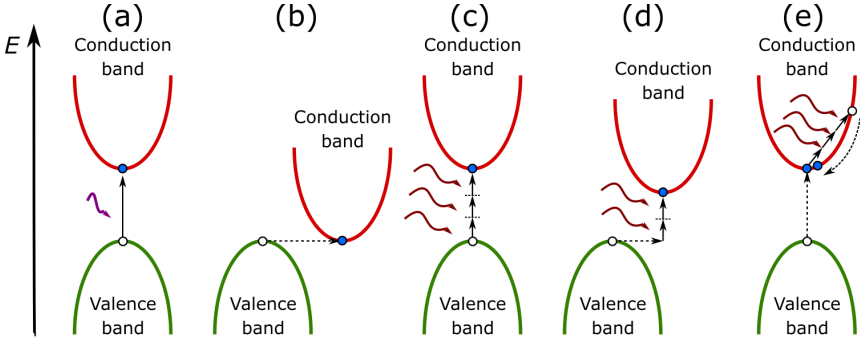


Figure 1.6: Simplified schematics of various excitation regimes found in laser material processing: (a) - one photon absorption, (b) - tunneling ionization, (c) - multiphoton excitation, (d) - hybrid between multiphoton and tunneling ionization, (e) - avalanche ionization.

### 1.3.2. Various Femtosecond Processing Examples

One of the key technological operations is cutting of the material. Throughout history, various mechanical cutting methods were developed. However, in simplified terms, in order to efficiently cut material of a given hardness, a harder material is needed. This is the basis of the Mohs scale, showing which minerals can scratch other substances. However, any mechanical processing results in tools getting dull over time and potentially introducing their own material to the cut. Laser light, on the other hand, interacts directly with the material on a quantum level and is contactless, meaning that there are no limitations in terms of the processable material and no tool induced contamination. For this reason, laser material processing gained huge popularity in a lot of different fields.

Ultrashort pulses introduce several key differences to the laser cutting process. First, as mentioned before, there is no need to directly target  $E_g$  with laser's  $\lambda$ , meaning that any material can be processed, including live tissue [137], polymers [138], metals [139], glasses [140] and crystals [141]. Furthermore, the time-frame of interaction between light and single atoms in the focal region becomes substantially shorter than heat dissipation from the affected region. Thus, heat effects can be highly localized and suppressed, leading to the so-called "cold processing" [Fig. 1.7], which can be used for great effect for ultra-clean cutting and drilling with feature sizes down to

$\mu\text{m}$  with minimal heat-induced damage to the surrounding area [8, 11, 142]. This allows fs-based cutting and drilling to exceed the precision of any other kind of direct machining technique.

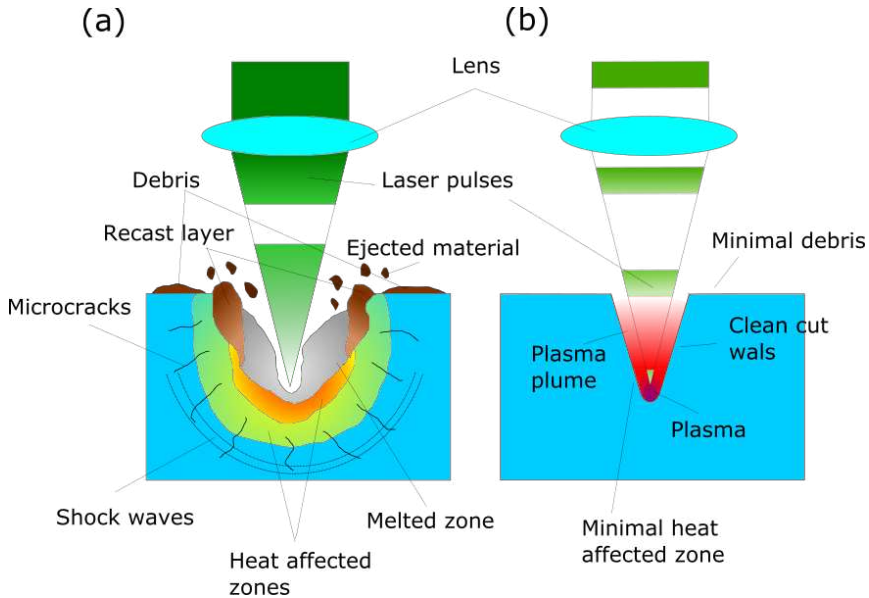


Figure 1.7: Schematics highlighting the differences in ablation using ns and fs pulses. Due to high light intensity in the focal point and superb control of thermal effects substantially better cut quality can be achieved with fs pulses.

Cutting is an example of a very straightforward interaction between fs laser and matter. However, more precise control of light parameters can yield true nanofeatures on a surface of the material with feature sizes down to nm [143]. While the formation of surface patterns can be induced with longer pulsed lasers as well [144], fs pulses excel in this role and allow to create of not only true nanopatterns but also more intricate hierarchical micro-nano textures [145]. It is the result of relative suppression of heat effects, present with longer laser pulses, and a possibility for material to have different interactions with Gaussian laser spot as it is translated on the surface [146]. In that case, the central high-intensity part is responsible for the creation of microfeatures while the periphery of the laser spot induces nanogratings [Fig. 1.8]. There are several kinds of surface ripples, resulting due to various light-matter interactions at the surface [147, 148, 149]. The orientation, depending on the prevailing mechanism, can be perpendicular

(in most cases) to the light polarization or parallel [147, 148, 149]. Patterning of this kind exceeds chemical or coating-based methods as there is more control of texture's shape, orientation and they can be made on virtually any material [150, 151, 152, 145]. For this reason, it is considered to be a key enabler in high volume production of functional surfaces needed for anti-fouling, anti-icing, and similar applications.

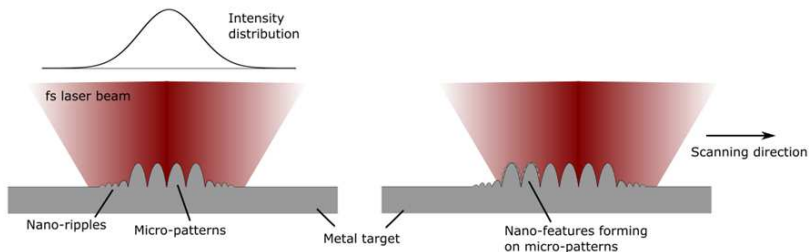


Figure 1.8: Formation of hierarchical surface patterns translating sample with fs-laser spot with Gaussian  $I$  distribution. The central part of the beam forms  $\mu\text{m}$  features. Subsequent exposure to the outer part of the laser spot that it is moving induces nanogratings on top of  $\mu\text{m}$  features.

Finally, the internal modifications of transparent medium *via* fs pulses should not be forgotten [Fig. 1.9]. It is a powerful tool to produce integrated functional elements inside transparent medium [153, 154]. Furthermore, the resulting modification can occur in the form of volume nanogratings which have useful functional properties for controlling the light passing through the sample [155, 156, 157]. Also, it was shown to greatly increase the rate at which modified volume is dissolved in etching solution [158]. Therefore, it can be used to create true embedded 3D glass and crystal structures *via* laser exposure and subsequent wet etching [Fig. 1.10] [159]. While it is applicable only for transparent mediums, it exceeds direct ablation in the flexibility of created 3D shapes. Direct material removal can be used for intricate 3D structure creation as shown with metal ablation [160], but etching allows to embed channels and similar objects into glass volume [159]. Furthermore, if experiment conditions are correct, taperless channel walls can be made with surface roughness down to sub- $\mu\text{m}$  [161]. For these reasons, laser-assisted selective etching (LASE) was used with great effect in the field of microfluidics, where precision and quality enabled by the LASE are very attractive for the functionality of the most advanced LOC systems.

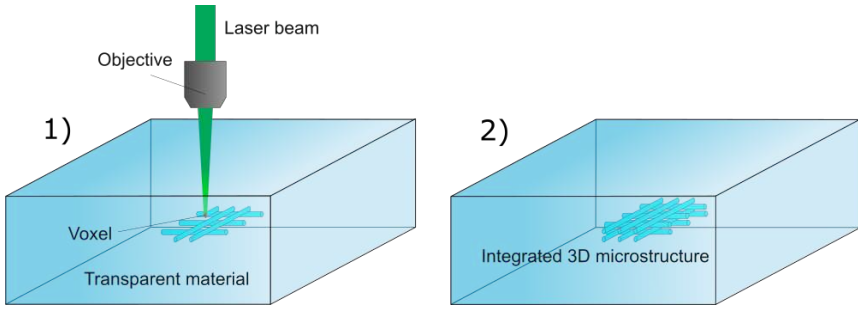


Figure 1.9: Principle of inscribing modified regions inside a bulk of the transparent medium. 1) - laser is focused into a volume, creating local modification. 2) - after laser exposure structure is ready to be used.

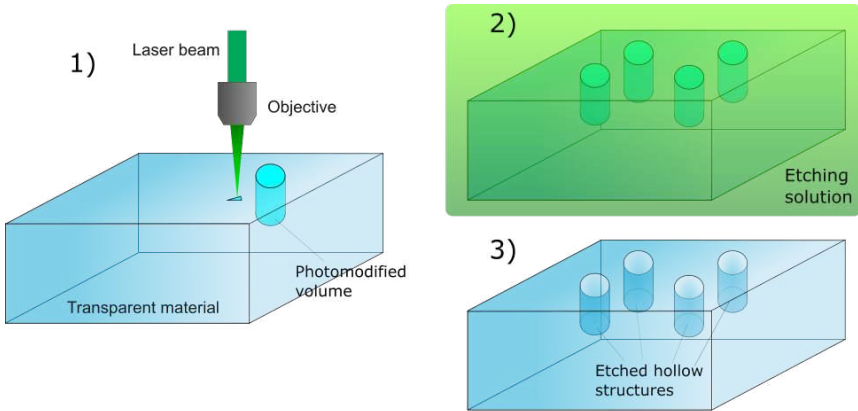


Figure 1.10: Steps needed for LASE: 1) - material modification, 2) - etching in acid, 3) - final structure.

### 1.3.3. Perspectives of Femtosecond Manufacturing Field

There was quite a substantial development of fs lasers over the last two decades. Both stand-alone oscillators and amplified systems are capable of covering a huge range of tunable parameters including  $\tau$ ,  $f$ ,  $P$ , and  $\lambda$ . Further developments will be associated with better understanding and exploitation of existing laser mediums (for example, Er [162] and Yb [163] doped mediums) as well as the adoption of some new materials [164]. A combination of DPSS lasers and fiber-based systems will allow to further

enhance the flexibility of such systems. Overall, the advances will be tightly tied to the requirements dictated by science and industry.

Further enhancement of throughput without compromising the structure quality is also highly desirable. Most of the discussed techniques are point-by-point DLW, making them inherently slow. Additionally, if a volume structure is formed (for instance, LASE and 3DLL cases), it increases the time needed for fabrication by the order of 3, making the volume fabrication slow. To remedy this, several solutions were proposed. If positioning precision can be relatively low, i.e.  $\mu\text{m}$  and more general translation velocities can reach m/s and more [165]. However, relatively fast (cm/s and more) and still very precise (down to nm level) positioning can be achieved with modern positioning systems relying on linear stages [166], galvo-scanners [167] or synchronization of both [168]. The last solution is very attractive as it allows to have unlimited working volume (needed for stitch-free printing) and nano precision while maintaining high translation velocities. Throughput can be further increased using multiple beams at once, which can be done using passive elements [169] or spatial light modulators [170]. In addition, spatial light shaping can also be used to create intricate laser beams [121] or correct deficiencies in focusing occurring due to specific processing regimes or materials [171]. One also should not forget possibility of using acousto-optical deflectors [172] which would basically eliminate mechanical inertia from the positioning and, thus, result in a massive increase in processing speed with minimal sacrifice in terms of resolution. Finally, modern fs laser development itself should not be overlooked. One of the approaches shown to potentially greatly increase structuring throughput is the usage of fs bursts. While it is a relatively new area primarily tried in subtractive machining [142], it already shows great promise in increasing overall throughput [173]. In conclusion, while fs are a well-established tool in material processing, the technology itself can be greatly improved for even more spectacular results.

## 1.4. 3D Laser Lithography

Lasers capable of generating fs pulses paved the way for entirely new thinking in material processing. At these pulse durations, the time of interaction between light pulse and the electrons is a lot shorter than the time needed to disperse the heat between electrons and atoms/ions [174, 175]. This made a massive impact on subtractive manufacturing. It was shown that reducing repetition rate [8] or delivering fs radiation in bursts [11] allows

minimizing the thermal effects enabling the so-called "cold processing". In the context of additive 3D manufacturing, ultrashort pulses and controlled thermal effects played an important role in both sintering and LIFT, yet the most prominent result was a development of fs-pulse initiated 3DLL [12]. It is based on the principle of point-by-point direct writing structures with the sharply focused laser beam. This allows printing with volume pixels (voxels) only where  $I$  exceeds the polymerization threshold intensity  $I_{th}$  required to induce non-reversible photo-modification [Fig. 1.11]. Combining unmatched flexibility in terms of materials, achievable 3D geometries, and applicable substrates, it enabled the entire generation of new functional devices as discussed next.

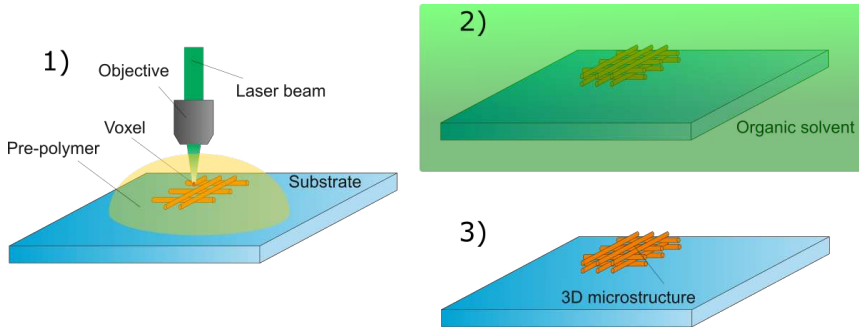


Figure 1.11: Schematics of 3DLL technology: 1) laser beam is tightly focused on pre-polymer material. Where  $I$  is equal or exceeds  $I_{th}$  photopolymerization reaction occurs, allowing point-by-point structuring of the arbitrary shaped 3D micro object. After that development 2) reveals final free-standing structure 3).

### 1.4.1. Photopolymerization *via* fs-Induced Non-Linear Light-Matter Interactions

In the case of standard lithography, the polymerization reaction is induced by the absorption of a single short-wavelength photon with an energy equal to or greater than the bandgap of the resin [Fig. 1.6 (a)]. It is a linear process not influenced by the intensity of the light and, therefore, is happening in the entire volume of the resin in which photons with the appropriate wavelength are present. However, a similar photoexcitation can be achieved *via* longer (visible or infrared) wavelength which has  $E_g$  insufficient for the direct absorption [133, 176, 177]. If such radiation is delivered in the form

of tightly-focused fs-pulses the  $I$  can reach the level of TW/cm<sup>2</sup>, which is more than sufficient for molecules to absorb two or more photons at the same time. In contrast to the one-photon absorption, the modification by MPA only occurs if the intensity  $I$  exceeds the threshold  $I_{th}$ . Then the concentration of modified cross-linked polymer chains exceeds what can be dissolved during the development process yielding building blocks for the final structure. This enables a precise control inside the volume (transparent) in which the process (polymerization, breakdown, thermal heating, etc.) occurs. The simplest case of MPA is a two-photon excitation which is credited as being the most prominent process in 3DLL. Nevertheless, while MPA can well explain most of the results acquired by 3DLL, there are some experimental data that could not be sufficiently described by such light-matter interaction. For instance, it was shown that pure (i.e. non-photosensitized) resins can be structured directly in a 3D fashion using laser pulses in the range of hundreds of fs [133, 178, 179, 34]. It is considered that MPA still plays an important role in processing, yet the effectiveness of the whole process is also influenced by the avalanche ionization.

In order to completely comprehend the dynamics and prevalence of each process, we will look at the rates of free electron generation in the pre-breakdown condition in the polymer when it interacts with the tightly focused ultrashort pulse. For now, we will discard any thermal effects that could alter the response of the material as it is appropriate for the excitation by ultra-short laser pulses. In this case, the combined density of electrons  $n_e$  generated by both MPA and avalanche ionization after the laser pulse is given as [180]:

$$\frac{dn_e}{dt} = n_a w_{mpi} + n_e w_{imp}, \quad (1.7)$$

where  $n_a$  is the density of molecules that could act as electron donors for photo-cleavage and  $w_{mpi}$  with  $w_{imp}$  denote the electron generation rates by MPA and impact (avalanche) ionization, respectively. If we consider that recombination is negligible and the initial condition is  $n_e(t=0)=n_{e0}$ , equation 1.7 has a solution that reads:

$$n_e(I, t) = \left\{ n_{e0} + \frac{n_a w_{mpi}}{w_{imp}} [1 - \exp(-w_{imp}t)] \right\} \exp(w_{imp}t), \quad (1.8)$$

with  $\lambda$  being the wavelength of light. The rates can be written as:

$$w_{mpi} \simeq \omega n_{ph}^{3/2} \left( \frac{\epsilon_{osc}}{2J_i} \right)^{n_{ph}}, \quad (1.9)$$

$$w_{imp} \simeq \frac{\epsilon_{osc}}{J_i} \frac{2\omega^2 \nu_{e-ph}}{(\nu_{e-ph}^2 + \omega^2)}, \quad (1.10)$$

here  $\omega$  is the light frequency,  $J_i = e\Delta E$  is the ionization potential ( $e$  - the electron charge,  $\Delta E$  - the bandgap of the host material),  $n_{ph}$  defines the number of photons required for ionization,  $\nu_{e-ph}$  is the electron-phonon momentum exchange rate which at the breakdown can be estimated to be  $6 \cdot 10^{14}$  1/s. The oscillation energy of an electron  $\epsilon_{osc}$  can be defined as a function of  $I$  and  $\lambda$ :

$$\epsilon_{osc}[eV] = 9.3 \left( \frac{I}{10^{14}[W/cm^2]} \right) \lambda_{\mu m}^2. \quad (1.11)$$

Using these formulas,  $w_{mpi}$  and  $w_{imp}$  can be estimated. Let us take the hybrid organic-inorganic zirconium SZ2080 [181] as an example. If PI Irgacure 369 (2-benzyl-2-dimethylamino-1-(4-morpholinophenyl)-butanone-1) is used for photosensitization, photosensitized SZ2080 has the maximum of absorption at  $\lambda_{abs} \approx 390$  nm with  $J_i \approx 3.18$  eV. Considering laser irradiation at typical near-IR wavelength 1030 nm and pulse duration 300 fs, one would need  $I \simeq 8.7$  TW/cm<sup>2</sup> for the structuring. In such experimental conditions,  $w_{mpi} = 0.81 \times 10^{12}$  1/s and  $w_{imp} = 91.1 \times 10^{12}$  1/s meaning that avalanche ionization is a more prevalent process and cleaves substantially more chemical bonds than MPA [182]. However, one should consider that for an efficient avalanche ionization sufficiently long (hundreds-of-fs) pulses are needed, as the time between impacts of electrons and atoms has a finite time [175]. Therefore, if the pulse duration is decreased to tens-of-fs or less, the total amount of electrons generated *via* MPA exceeds that of the avalanche. At the same time, if the pulse duration is relatively long (reaching several ps and more), ionization continues to the point of the material being optically damaged [183]. Overall, the exact balance between these two processes is greatly dependent on experimental conditions.

Finally, thermal effects should be discussed, as the temperature alter the bandgap of the material [133] and, in the case of high temperatures (hundreds of °C), can cause thermopolymerization [184]. The typical cooling duration of the focal volume could be estimated as  $t_c = d^2/D$ , where  $d$  is the diameter of the laser spot and  $D$  [cm<sup>2</sup>/s] is the thermal diffusivity of the polymer. Keeping in mind that  $d$  is in the range of laser wavelength and typical  $D$  for polymers is around  $10^{-3}$  cm<sup>2</sup>/s [185],  $t_c$  can be considered to be  $\sim 10$   $\mu$ s, meaning that all pulsed lasers operating above 0.1 kHz repetition rate should cause a thermal accumulation during the exposure



of spatially overlapping pulses. Thus, there is no surprise that strong thermal interaction was observed and employed for direct one-step polymerization of SU8 that otherwise should require two steps to cross-link: exposure and heating [186]. However, some of the experimental investigations show completely different results. For investigated parameters ( $\lambda = 810$  nm,  $\tau = 100$  fs, repetition rate  $f = 80$  MHz) a drastic increase (hundreds of °C) of temperature occurs only when the material is optically damaged [187]. Therefore, the severity of thermal effects in 3D laser nanoprinting is still a matter of heated discussion in the field.

### 1.4.2. Direct sub-Wavelength Fabrication

As it was established for the standard case, fs-lasers with  $E_g$  lower than the direct absorption band of the polymer induce polymerization *via* nonlinear processes; the lowest order, hence, the most efficient, among them are avalanche and TPA. One of the key aspects of any nonlinear process is that it has a threshold  $I_{th}$  below which the material is not sufficiently affected, enabling true point-by-point structuring with sub-diffraction limited resolution.

In classical optics,  $I$  distribution at the focus can be described as Gaussian:

$$I(r, z) = I_0 \frac{w_0^2}{w(z)^2} \exp\left(\frac{-2r^2}{w(z)^2}\right), \quad (1.12)$$

here  $r$  is the distance from the optical axis,  $z$  - distance from the focal plane parallel to the optical axis,  $w_0$  is the spot radius (waist),  $I_0$  - intensity at the center of the focus ( $r = 0$ ,  $z = 0$ ).

By substituting  $I_{th}$  in equation (1.12) we can determine the transverse  $D(r)$  and longitudinal  $L(z)$  dimensions of the voxel. For simplicity, we would consider that only MPA of  $n_{ph}$  is present [188]:

$$D(r) = w_0 \sqrt{2 \ln\left(\frac{I(r)}{I_{th}}\right) \frac{1}{n_{ph}}}, \quad (1.13)$$

$$L(z) = 2z_r \sqrt{\left(\frac{I(z)}{I_{th}}\right)^{\frac{1}{n_{ph}}} - 1}. \quad (1.14)$$

These formulas can be tailored to reflect light-matter interaction by use of phenomenological parameters to better reflect true experimental conditions. One should add the time of exposure  $t$  and  $\tau$  (which are not equal if the

structure is formed in a scanning fashion and/or by multiple pulses),  $f$ , focusing conditions (defined *via* NA), and the interaction between light and TPA constant of the polymer  $\beta$ . Therefore, the above equations read [188]:

$$D = \frac{\lambda}{NA} \sqrt{\ln \left( \frac{I_0^2 t \beta \tau f}{I_{th}} \right)}, \quad (1.15)$$

$$L = \frac{2z_R}{n} \sqrt{\exp \left( \frac{1}{2} \left( \frac{D \times NA}{\lambda} \right)^2 \right) - 1}. \quad (1.16)$$

These definitions are approximate and, at the moment, there is no precise method to calculate voxel size theoretically just by having experimental parameters as variables. However, the equations (1.12), (1.15) and (1.16) provide scaling insight into the dynamics of point-by-point polymerization. First, in the standard case, voxels are elongated in the longitudinal direction. The higher the NA and the lower  $I$ , the more spherical is the voxel [34]. Additionally, following this model, an increase in nonlinearity ( $n_{ph}$ ) should also reduce the aspect ratio of the voxel. Finally, looking from a completely theoretical standpoint, voxels with dimensions approaching zero should be possible if  $I$  is controlled with uncertainty  $\Delta I$  also approaching zero. In the real world, this is impossible due to the inherent instability of any laser source.

Polarization induced peculiarities in polymerization are also not factored formulas (Eq. 1.15, 1.16), although the precise polarization control at sharp focusing conditions allows tuning voxel size and aspect ratio on a nanometers scale [189]. It is noteworthy that if the right material is used and proper experimental parameters are applied for exposure, the voxels as small as 65 nm can be made *via* 3DLL. This was achieved with NA = 1.4 objective lens at a 520 nm wavelength and 1 kHz repetition rate with a laser generating  $\sim 100$  fs pulses and special acrylate-based polymer [190]. At the same time, if NA is relatively low (less than 0.4), voxels in the size range of tens-of- $\mu\text{m}$  were fabricated [35, 36]. It is relevant if relatively large structures (for instance, scaffolds for stem cell growth) are needed, and manufacturing them using a high NA immersion objective would be inefficient. By the combination of different focusing conditions for exposure of a single structure, fabrication for enhanced efficiency without sacrificing resolution was also demonstrated [61]. Overall, this proves the high flexibility of the O3DP when it comes to the selection of the voxel size best suitable for the specific application.

As it is difficult to predict the exact voxel size theoretically, several methods to determine them experimentally were proposed. The most common one is called resolution bridges [134, 191]. Strong supporting walls are made first. Then, suspended lines are produced perpendicularly to them. The sample is developed afterward and the width of lines is measured using scanning electron microscopy (SEM). This method provides the real size of 3D features fabricated during O3DP experiments. The main drawback is, however, that thinner lines might be destroyed during the liquid-bath development and rinse with a subsequent drying due to capillary forces of the evaporating liquid. Therefore, for the ultra-high resolution features 3D formed, a critical point dryer (CPD) should be applied [192]. This allows to totally avoid surface tension in a super-critical liquid, usually CO<sub>2</sub> and high fidelity reproduction of the nanoscale features.

### 1.4.3. Compatibility with Other Fabrication Methods

One of the key aspects of making 3DLL the technology of choice in many applications is the possibility to form 3D structures on (or in) functional substrates made by a variety of other methods. For instance, objects can be fabricated on the surfaces of structures made by other varieties of 3DP. As different 3DP techniques offer flexibility in terms of structuring resolution, combining 3DLL (which is the most accurate) with something as the fused deposition modeling (resolution from tens-to-hundreds of  $\mu\text{m}$ ) allows for a true mesoscale fabrication with a minimal amount of technological steps used [193, 62]. Another example of a tandem additive optical structuring is pairing 3DLL with LIFT, when 3DLL is used to produce a 3D scaffold that is subsequently seeded with live cells *via* LIFT, combining 3DLL provided freedom of structure design and selectability of cell seeding by LIFT [194].

The next step is a combination of additive and subtractive manufacturing. Microfluidics is the field where we can find the most of such examples. Glass is one of the materials that is relatively hard to process in an additive fashion but is highly desired in the fields like microfluidics or optics for being optically and chemically inert. At the same time, only subtractive fabrication is incapable of producing some of the microdevices that could be needed in microfluidic devices. Thus, a hybrid approach combining subtractive and additive manufacturing is used. First, subtractive methods, such as ablation or etching are applied to create the required channel system. Then, 3DLL is employed to integrate needed structures inside it [17, 18, 195]. Subtractive methods are generally faster and simpler in channel manufacturing

while 3DLL is unmatched in design freedom, flexibility, and printing resolution. By combining the two, one can bring the most desired features of both approaches for the best possible result.

While discussing the hybrid subtractive-additive fabrication it is important to understand that both approaches of structuring can be achieved with an amplified fs-laser source by varying light exposure parameters (focusing,  $I$  and  $f$ ). Therefore, a single laser manufacturing setup can be assembled by a combination of both O3DP with the other manufacturing technique such as ablation, selective etching, or welding [18]. The pairing of this kind is extremely attractive as it eliminates the need to have multiple setups dedicated to just one technological operation, thus greatly reducing investment in hardware needed for all-around functional micro- and nano-fabrication.

#### 1.4.4. Towards 4D Printing

3DLL enables 3D structuring of a wide variety of materials. Furthermore, the processing is straightforward and can be repeated numerous times on the same sample. If each time a different polymer is applied, multi-material printing of both 2D [51] and 3D structures [196] can be achieved. It introduces an additional dimension of material to the final object. Hence, in the case of a 3D object with varying composition, it can be considered as a 4D printing [197].

Possible applications start in the medical sector. Regenerative medicine is a fast-growing field where 3DLL promises the possibility to create 3D scaffolds that resemble the shape of the extracellular matrix. Despite the current success of this approach, single polymer scaffolds cannot mimic extracellular matrix closely as it consists of many different components. An answer to this problem could be multi-material scaffolds where different parts of the structure would be made from a diverse range of substances [16, 198]. As cell response to adjacent materials can differ from attraction to repulsion or being completely inert [16], 4D printing not only promises the scaffolds that could replicate extracellular matrix well but also a possibility to control cell migration in a well-defined environment. Further challenges in this field lie in the development of new and more efficient printing strategies that would enable multi-material printing of mm-sized scaffolds needed for true tissue regeneration.

Multi-material micromechanics is another promising area for 4D printing. Polymers react to the surrounding medium by either shrinking or expanding with the extent of this interaction depending on the polymer itself. This

can be exploited by creating the suspended bi-polymer micro-plates with movement depending on the surrounding medium creating either a passive sensor or actuator [196]. Alternatively, the same polymer with a varying cross-linking degree could be used to exploit divergence in thermal expansion as polymerization degree heavily influences this property [13]. True 3D free-form structuring capabilities of 3DLL and the ability to change exposure parameters on-the-fly allow to selectively expose material with the different laser power and create a 3D shape with segments of different cross-linking degree. It results in a varying microscopic expansion when the material is heated compensating itself (due to specific geometry) in macro-scale and subsequent negative thermal expansion coefficient of the overall structure. Varied polymerization degree can also be exploited in order to create gradient refractive index (GRIN) based optical elements [199].

## 1.5. Applications of 3D Laser Lithography

The flexibility to change the printing resolution and foot-print size, capability to fabricate on/in almost any substrate and a wide array of applicable materials made 3DLL a technology of choice in many fast-growing science and engineering fields.

In micromechanics, the freedom of design was exploited to create various movable structures [200, 201]. This is especially relevant for the creation of mechanical metamaterials, realizing macro-properties of the structure that are not found in nature, *via* a cleverly designed interconnected micro-lever systems. For instance, a negative Poisson coefficient can be achieved [192, 202]. A mechanical cloak was also demonstrated [203]. These results demonstrate that a combination of unrestricted 3D geometries and easily accessible micro- and nano-resolution is the key to develop objects with the preprogrammed and otherwise unachievable mechanical qualities/properties.

In the field of LOC, the dominant materials of choice are glasses and various elastomers, mainly PDMS. These materials are difficult to process in true 3D fashion in the scale below several- $\mu\text{m}$  while there is a need for functional 3D objects with such dimensions. Therefore, an approach of employing O3DP for structure integration inside LOC devices was proposed and tested [204]. Despite restraints given by the necessity to work in glass channels, structures with high fidelity and complex 3D geometries were integrated, ranging from various filters [17, 18] to channel separators [205] and valves [201]. What is more, the integration could be performed before

the channel is sealed [18] or afterward in the so-called “ship-in-the-bottle” fashion [17].

With regenerative medicine being one of the hot topics in current biomedical research, O3DP was used to great extent in this field as well. In contrast to most other types of scaffolds for cell growth, O3DP-fabricated ones have a well-defined 3D geometry that could be made to resemble extracellular matrix as closely as possible [15, 16, 198, 206, 207]. Furthermore, by tailoring feature size, any type of mammal cell can be accommodated by printed scaffolds. So far, a wide variety of O3DP processable materials were proven to be bio-compatible turning a green light for the *in – vivo* experiments [208, 209]. Cells showed a good proliferation on the laser fabricated 3D scaffolds as well. Until now, the research in this field reached the stage of the pre-clinical trials [15] which is a formidable achievement for this strongly regulated application.

As surface roughness of laser-made structures can be as small as several nm [34], O3DP was employed to produce micro-optical elements as well, where  $\lambda/20$  surface finish is achievable for the most demanding focusing and imaging applications. At the infancy of the technology, the capability to produce arbitrary shaped micro-optical elements on standard glass substrates was investigated [188, 210]. Further developments led to monolithic 3D elements, combining several functional micro-optical structures into one, for instance, an axicon and spiral phase plate (SPP) hybrid [211] or micro-objectives [100]. These were put on functional substrates, e.g., fiber tips [19, 212], nonlinear crystals [26] and CCD matrices [213]. Light manipulation with this kind of micro-optics enables applications in ultra-compact endoscopy [100] or foveated imaging [213]. The next frontier in this field is in making mesoscale components that are as large as millimeters still retaining nano-precision with nanoscale features and a complete 3D design freedom. Finally, it was shown that the optical damage threshold of some hybrid organic-inorganic photopolymers [181] is comparable with that of glass [38, 214] meaning that it could potentially be applied for applications dealing with high light intensities, like fiber lasers, communications, free space lidar, and filamentation.

The smallest features that are relatively easy (i.e. without any additional post-processing or other methods) to achieve *via* 3DLL is around several hundreds-of-nm which is sufficient for photonic applications [176]. Woodpile photonic crystal is the most simple case of 3DLL made 3D nano-optical elements and was proven to be an efficient way to influence the spatial distribution of incident beam [153]. Other complex 3D structures were

tested as well, for instance, chiral configuration [215]. Alongside direct 3DLL of polymeric photonic structures, metal ones were also acquired by making 3D templates *via* fs laser, then filling them with the metal, therefore acquiring nano-optical elements out of metals [216]. It is important to note that the lower limit of the printing resolution (several hundred nm) is still a limiting factor for shorter wavelength (for example, visible) photonic applications.

## 2. Experimental Section

### 2.1. Fabrication Setups

Two experimental setups were used in this work. The first workstation was located in Vilnius University Laser Research Center and is shown in Fig. 2.1. It was used for PI-free polymerization and optical resistance experiments. The fs-laser was "Pharos" (Light Conversion Ltd.) operating at 1030 nm fundamental wavelength, 300 fs pulse duration, and 200 kHz repetition rate. Power was controlled with two power control units consisting of  $\lambda/2$  waveplate and Brewster angle polarizer. Such two-stage power attenuation allowed to minimize fluctuations in laser output power and provided precise power control during the fabrication. 515 nm wavelength was used for 3D free-form polymerization. The laser beam was expanded by  $2\times$  magnification telescope in order to fill all the objective aperture. Structure fabrication was performed with a combination of Aerotech linear stages (ALS130-110-X,Y for positioning in XY plane, ALS130-60-Z for Z-axis) and galvo-scanner, operating in a synchronized regime. The sample was also illuminated by red LED which enabling to monitor the fabrication process in real-time using a CMOS camera. It was used for PI-free structuring and LIDT experiments.

Meso-scale samples were produced using the "Laser Nanofactory" (Femtika) setup [Fig. 2.2]. The main light source in this setup was fs-laser "Carbide" (Light Conversion Ltd.), outputting either fundamental (1030 nm) or second harmonic (515 nm) radiation at repetition rates in the range of 60 - 1000 kHz and pulse duration between 250 fs and 10 ps. Average power was controlled with an acousto optical element integrated into the laser as well. Laser light was guided to an automatic beam expander with a magnification range from 2x to 10x. This tunability was needed to precisely match laser beam diameter to the entrance aperture of the arbitrary objective. Finally, it was directed to the scanner system (AGV-10HPO (Aerotech Inc.)) and then to the focusing objective. Scanners worked in tandem with



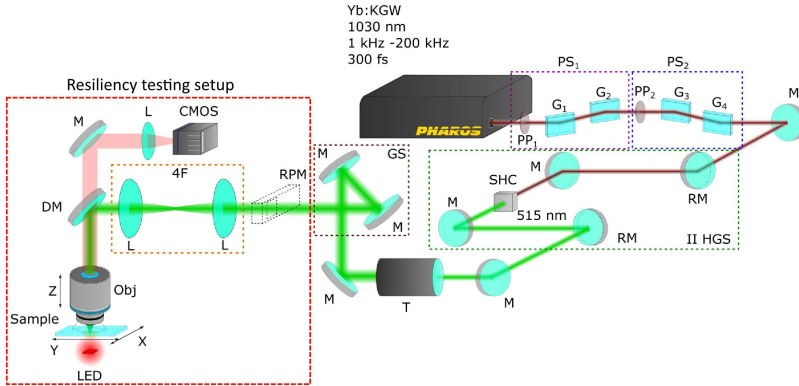


Figure 2.1: Schematics of setup used for fabrication and microlens degradation experiments: PS - power control stage, PP - phase plate, G - glass plate, M - mirror, RM - removable mirror, SHC - second harmonic crystal, T - telescope, GS - galvo-scanner, RPM - removable power meter, L - lens, 4F - lens system in 4F configuration, DM - dichroic mirror, CMOS - CMOS camera used to monitor fabrication process, Obj - objective lens, LED - LED used for sample illumination.

linear stages (ANT130XY-160 (Aerotech Inc.) for XY and ANT130LZS-060 (Aerotech Inc.) for Z axis) allowing synchronized positioning. The whole process was imaged through a built-in visualization system, employing a CMOS camera, variable focal length lens (needed for imaging with different objectives), and a red LED. Objectives used in this work: 63x 1.4 NA (Zeiss), 40x 0.95 NA (Zeiss), 20x 0.8 NA (Zeiss) and 20x 0.45 NA (Nikon). All the components in the system were controlled with 3DPoli software (Femtika).

One of the key novelties in this work was the application of synchronized linear-stages and galvo-scanners. While the idea of using synchronization of different positioning systems is not new [37] and this kind of synchronization was already used prior [15], it was never established what are the full capabilities of such positioning strategy. The principle behind synchronization can be explained in terms of distributing the translation movements between linear translation stages and scanners. Practically, the high inertia stages are responsible for long and continuous movement, while low inertia scanners perform fast yet small effective amplitude movements. It is used for correcting the positioning error of the linear stage movement. This way the linear stages have time to accelerate and decelerate without causing any defects that are noticeable in the produced structure. The de-

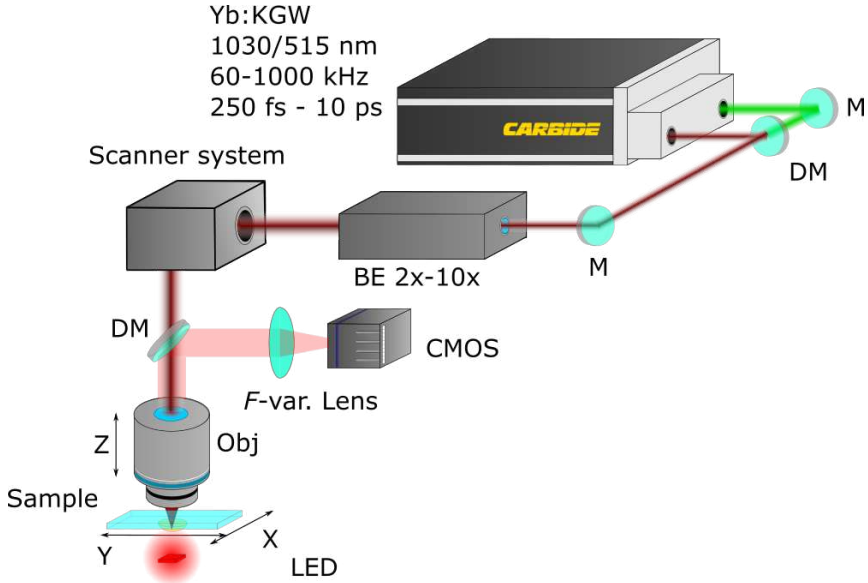


Figure 2.2: Schematics of Laser Nanofactory setup used in this work. Markings: M - mirror, DM - dichroic mirror, BE - automated beam expander, F-var lens - variable focal distance lens, Obj. - objective.

viations occurring for a set translation velocity and trajectory are compensated by the scanners *via* a closed-feedback loop. The positioning devices are commanded using a controller with a native trajectory rate of 48 kHz for galvo-scanners and linear stages. Thus, it corresponds to a trajectory update approximately every 20  $\mu$ s. At a scanning speed of 10 mm/s, it resulted in a trajectory of individual 0.2  $\mu$ m length segments. During large structure manufacturing, the command instructions for the controller were sent segment-by-segment using a compiler software installed on a personal computer to ensure that the internal memory is not overloaded. All the calculations of the distribution of movements and stage control were performed by the proprietary Aerotech software and controllers [217].

## 2.2. Materials and Characterization

The goal of this works was to find ways for rapid 3D manufacturing of mesoscale structures using 3DLL without compromising on structure quality or resolution. Furthermore, the optical resistance of fabricated objects

also needed to be tested. Thus, a purpose-driven choice of materials and equipment was made.

SZ2080 photoresist was acquired from FORTH (Heraklion, Greece) and, as its name implies, contained 20 wt% of inorganic and 80 wt% of organic parts. This material was chosen due to its low shrinkage [181] and high optical transmittance [38]. For some experiments, SZ2080 was photosensitized by mixing it with 1 wt% of a commercial PI Irgacure 369 (IRG). Samples were prepared by drop-casting one droplet of the material on a glass substrate and then pre-baking sample at 75°C for 45 min. The overall diameter of such drop can be as big as it needs to be, thus pre-polymer size in XY direction is not an issue. However, a single drop yields a layer height of  $\sim 250 \mu\text{m}$ . If a higher structure is needed, additional drops can be put on an already pre-baked sample. Then, each consecutive drop requires an additional 90 min of pre-bake time. Pre-polymer drop is homogeneous after such procedure, i.e. there are no seams between each material layer. After fabrication, samples were developed in isobutyl methyl ketone for 45 min.

Another material used in the work that required rigorous pre-fabrication protocol was SU8. It was used in the last chapter for LIDT experiments and was chosen due to its popularity in standard lithography. SU8 was pre-baked using a procedure, consisting of two pre-bake stages, 30 min on 60°C and 60 min on 90°C, then post-baked on similar temperatures but with half durations (15 and 30 min respectively) and development in propylene glycol methyl ether acetate (PGMEA) for 60 min. 1 mm and higher drop height can be easily acquired with SU8 with only a single material drop, thus multiple pre-bake steps were not needed.

The average laser power  $P$  was measured as the main laser radiation output parameter and subsequently recalculated to the peak intensity  $I_0$  at the center of the focal point using eq. 1.3.  $P/I_0$  in which there were no surviving structures due to insufficient cross-linking to carbonization of the material and subsequent destruction of the structure due to overexposure was considered fabrication window.  $P/I_0$  value in this range is directly responsible to mechanical [13] and optical [199] properties of the material,  $P/I_0$  in the whole work will be given as the position in the fabrication window unless the exact value is needed for the result evaluation.

Surface roughness was characterized using SEM TM-1000 (Hitachi) and atomic force microscope (AFM) Catalyst (Bruker) with an Au coated SiN-needle with a  $k=0.06 \text{ N/m}$  stiffness at  $FS=18 \text{ kHz}$  and with the tip diameter of 20 nm.

## 2.3. Laser Induced Damage Threshold Measurement

The Fig. 2.1 setup was also used to monitor the degradation of 3DLL made micro-optical elements in real-time. In such a case, a sample was microlenses on the glass slide illuminated by the LED from the bottom. The objective was placed at some defined distance from them resulting in a relatively large laser spot on the lenses. Exact values are listed in the text where it applies. This allowed to monitor lateral intensity distribution projected by the microlens and to shine onto them with fs laser light simultaneously.

Investigation of LIDT is well described by ISO 11254-1 and ISO 11254-2 standards [218]. It is designed for coated optical surfaces. Standards involve different LIDT measurement tests, which are commonly referred to as 1-on-1, R-on-1, and S-on-1. In this work, the statistical S-on-1 method with an fs-laser is designed to be as close to ISO testing protocol [218] as possible. It provided knowledge on both the damage topographies of the structures as well as statistically determined LIDT values. The principal scheme of LIDT evaluation is shown in Fig. 2.3. LIDT measurement was as follows: first, 3DLL formed objects were one by one exposed to the focused laser beam. The focal length of the lens used was  $f_l = 10$  cm, resulting in a beam waist of  $2\omega = 20$   $\mu\text{m}$ . The laser used - Yb:KGW laser "Pharos". The fundamental harmonic of such laser is 1030 nm, pulse duration - 300 fs, pulse repetition rate - 100 kHz. The experiment was observed in real-time by a CMOS camera integrated into the measurement setup. Each line in the 10 x 10 array was exposed to a different average laser power  $P$  for one minute (6 million laser pulses for each object).  $P$  was increased line-by-line. After all, components were exposed to the laser light, the sample was examined by an SEM and an optical microscope to see which components were damaged. Any modification in the object was considered as a sign of damage.

Every row contained 10 structures, for which statistical damage probability  $P$  was evaluated, by beginning with  $P = 0$ , when  $F$  was too low to cause damage to any of the irradiated structures, going to  $P = 1$  when  $F$  was high enough to damage every structure in the row.

Setup's built-in imaging system was used to deduce which structures were damaged during LIDT measurement. Counting them allowed to statistically deduce LIDT of the tested material. Moreover, this data was complemented by additional SEM inspection. It was necessary, as the optical damage

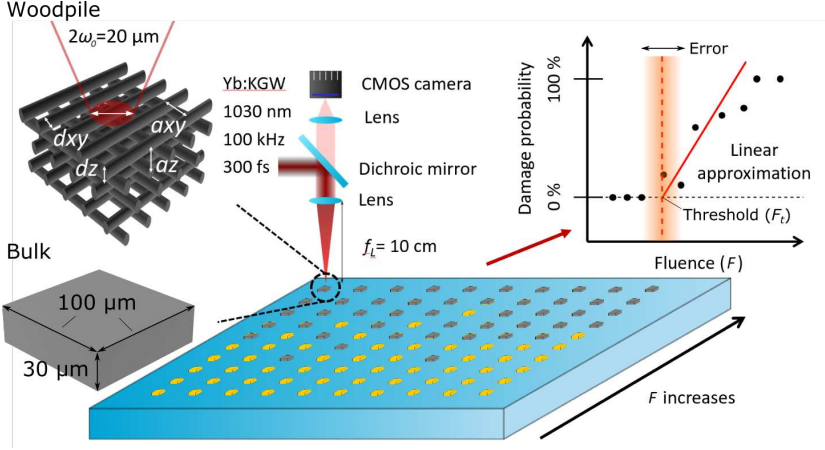


Figure 2.3: Schematics of LIDT measurement. A  $10 \times 10$  array of either bulks or woodpiles is exposed to 1030 nm 100 kHz 300 fs laser radiation. Both bulks and woodpiles were  $100 \mu\text{m} \times 100 \mu\text{m} \times 30 \mu\text{m}$  in size, with woodpile being arranged in fcc geometry. Each woodpile was also characterized by line width  $r$ , the distance between them  $axy$  and period  $az$ .  $F$  was changed from line to line, from no damage to all structures being damaged. This allowed plotting damage probability as a function of  $F$ . The linear approximation was then used to determine the  $F_t$ .

has different appearances depending on the different structure investigation methods. Here, we considered optical damage to be any laser radiation that caused a residual change in properties of the microstructure that can be observed using various inspection tools. For dielectric layers in ISO standard, the specific tool is specified as Nomarski type interference contrast microscope with objective magnification not less than 100x.

For LIDT calculation simple linear approximation of the dynamic range of the  $p$  was performed. Here we understand the dynamic range where  $0 < p < 1$ . In addition, the last  $p = 0$  and first  $p = 1$  points were taken. Linear approximation is done using the formula:

$$p = aF + b, \quad (2.1)$$

where  $a$  and  $b$  are slope and intersection coefficients. Then, keeping in mind condition that  $E_t \Rightarrow p = 0$  we get:

$$F_t = -\frac{b}{a}. \quad (2.2)$$

The error of LIDT measurement is a subject that gathered some interest and discussion in academia and is not straight-forward or trivial [219]. In accordance with practical considerations, the error's in LIDT measurement were considered to be single measurement step. Such an approach provides an adequate estimate while not complicating the mathematical mechanism of the investigation.

# 3. High-Throughput 3D Mesoscale Manufacturing

3DLL is a proven technology for a wide range of applications [5]. One of the final frontiers for widespread adoption of this technique is increasing its throughput without sacrificing the quality and spatial resolution of the structures produced. One of the most promising ways to achieve this is the usage of synchronized linear stage and galvo-scanner positioning. Despite it being a commercially available solution, there is very little understanding of how far it can be pushed in terms of translation velocities/accelerations without sacrificing structure resolution and/or mechanical quality. The challenge in using synchronized movements with sharp focusing (up to 1.4 NA objectives lies in the relatively small (down to 125  $\mu\text{m}$  square for 1.4 NA objective) working field. When the linear stages are moving at relatively high  $v$  (more than several mm/s), the galvo-scanners movement adjustments have to be made in an effectively limited field of view. In addition, faster change scanner deflection angles are needed to account for the same stage positioning errors in comparison to the case if the sample would not be moved by linear stages. In effect, it forces the galvo-scanners to move at elevated acceleration potentially pushing them to their precise movement limit. It makes the task of using synchronization for high-speed and high-precision manufacturing non-trivial.

In this section, it will be investigated to what extent synchronization can be employed for 3DLL, what are the main opportunities and considerations. Emphasis will be placed on how translation velocity, focusing conditions, and structuring strategy might influence the mechanical and optical functionality of the final object. This will be determined quantitatively, by investigating the functionality of formed structures and comparing them to the design requirements. Following the current trends of this technology, example 3D structures include micro-optical elements and various mechanical objects. Discussion on how their functionality can depend on print

quality and how synchronization can be critical in this regard.

The results presented in this section were published in III and IV articles of the approbation.

### 3.1. Comparison of Structuring Rates

The race to achieve industrial-level manufacturing throughputs pitted different kinds of optical 3DP methods against each other. While 3DLL has a superior resolution, other types of O3DP exceed 3DLL by the volume that can be structured in the same amount of time [220]. However, resolution/feature size and/or structuring flexibility had to be compromised to achieve it. As a result, when discussing the efficiency of printing, listing only  $v$  as the main throughput defining parameter is insufficient as it does not specify the size of formed features. Therefore, a lot more sensible way to talk about throughput is by defining the volume of a voxel and structuring rate in terms of voxels per second [167]. In order to calculate these values, we first produced a resolution bridge, where single lines were structured with translation velocities  $v$  of 1, 10, 100, 1000, and 10000  $\mu\text{m/s}$ , speeds. All of the scanning speed can be easily sustained using synchronized movement. Laser power was kept below 10% from the top of fabrication window [34]. Exposure conditions during the experiment were: 515 nm wavelength, 300 fs pulse duration, 200 kHz repetition rate. The transverse voxel size is labeled as  $D$ , while the longitudinal extension is  $L$ . Results are given in Fig. 3.1. The tendency for voxels to decrease in size by a factor of 13 when the  $v$  increases by four orders of magnitude is favorable for 3DP. A comparatively weak dependence of voxel size on scanning speed (exposure dose) results from the efficient combined crosslinking under single pulse exposure. Voxels' aspect ratio does not change and is in the range of 3-4, showing that the same scaling is observable in both transverse and longitudinal directions. Interestingly, other groups showed an opposite trend of the enlargement of the voxel when  $v$  is increased [221]. The primary difference from results presented here might lay in the higher repetition rate used by other group (80 MHz oscillator), which results in the negligible distance between pulses and reaction in the affected area of one fabricated line not being completely over when another nearby line is produced. Overall, achieved resolution is far from minimal of what can be achieved with this type of 3DLL system. With lower/optimized  $I$  feature size below 400 nm can be easily acquired [34]. However, as feature size reduction was not the aim of this study no experiments were performed in this direction.



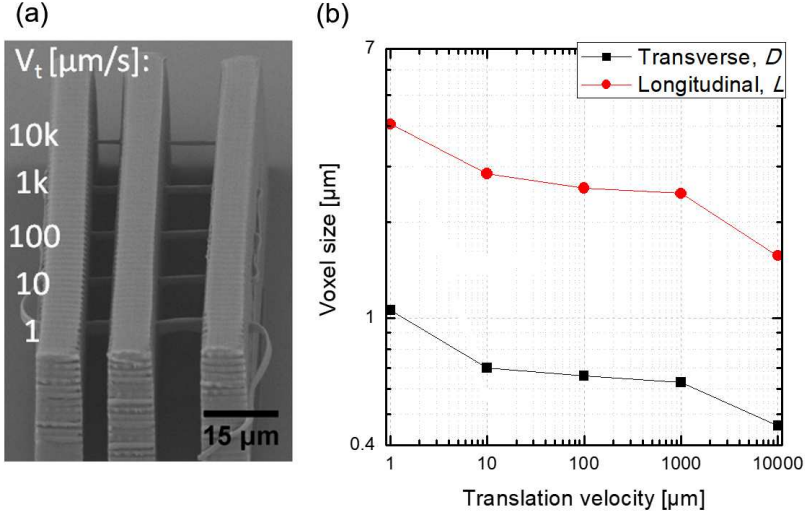


Figure 3.1: (a) The resolution bridge fabricated using different translation velocities  $v$  and measured line widths (b). The decrease in line dimensions is observable. However, the aspect ratio of voxels remains in the 3-4 range.

Acquired experimental results can be explained by varying pulse overlap  $\Delta d$  during printing [Fig. 3.2]. Indeed, if  $v_t = 1 \mu\text{m/s}$  the  $\Delta d = 0.005 \text{ nm}$  at  $f = 200 \text{ kHz}$  (the one used in this work). It is an extremely small distance, which is below even the positioning accuracy of the stages (which is in the range of  $\sim\text{nm}$ ). However, an increase in  $v$  by one order of magnitude to  $1000 \mu\text{m/s}$  reduces  $\Delta d$  to  $5 \text{ nm}$ . Then, it is already comparable to line width measurement error achievable with high-resolution SEM. With the highest tested  $v = 10000 \mu\text{m/s}$ ,  $\Delta d = 50 \text{ nm}$ . It is a rather significant distance, which becomes comparable to the spot size achievable with a 1.4 NA objective ( $2\omega \sim 500 \text{ nm}$ ). Thus, one might expect that the increase of  $v$  even further without changing  $f$  might result first in uneven lines and then to separate laser spots being formed. However, it should not be a problem, because modern amplified laser systems can achieve  $f$  in excess of  $1 \text{ MHz}$  with fs oscillators going as high as  $100 \text{ MHz}$ . In order to achieve  $\Delta d = 50 \text{ nm}$  with these systems,  $v$  should be increased as much as to  $50000 \mu\text{m/s}$  and  $5 \times 10^6 \mu\text{m/s} = 5 \text{ m/s}$  respectively. The first increase is still possible with scanners and, thus, high-resolution high-speed structuring with amplified laser systems might prove to have a fundamental limit determined by pulse

overlap. If oscillator [221] or fs-burst laser [173] is used even such positioning systems as polygon-scanners [222] or acousto optical deflectors [172] might be employed, provided related technical issues are resolved.

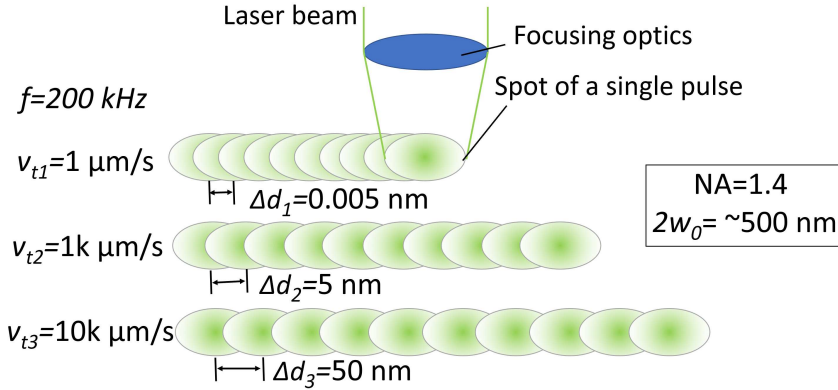


Figure 3.2: Schematic representation of differences in pulse overlap while varying  $v$ . Increase of  $v$  from  $1 \mu\text{m/s}$  to  $1 \text{cm/s}$  change  $\Delta d$  from  $0.0005 \text{ nm}$  to  $50 \text{ nm}$ , making it comparable to laser spot size  $2w_0 = \sim 500 \text{ nm}$ . Take note, that laser spots appear elliptical due to the isometric perspective of the drawing.

Due to the differences in pulse overlap, accumulated energy dose ( $E_t$ ) varies heavily from line to line. It is demonstrated by the numerical modeling [Fig. 3.3]. The results point out a considerable difference in threshold  $E_t$  in both cases ( $545.59 \text{ J/cm}^2$  vs  $1.98 \text{ J/cm}^2$ ). Interestingly, at  $1 \mu\text{m/s}$  the line width is substantially larger than the spot diameter ( $2w_0$ ), while in the case of  $10000 \mu\text{m/s}$  it is below the diffraction limit. This can be interpreted to be a result of continuous excitation of pre-polymer and expansion of polymerization volume in the low  $v$  case and highly contained energy absorption when high  $v$  is used. Also, radicals are generated for the increased amount of time during slower  $v$ , resulting in line broadening as radicals have an immense role in the writing resolution [178]. Finally, thermal accumulation might play a role as well, as the number of pulses to the same laser spot area increase by 4 order of magnitude. However, there is still a debate whether heating of the material takes place during 3DLL, even using laser oscillators with repetition rates up to tens of MHz [187]. Due to this uncertainty, thermal effects are left out of the discussion in this work.

In order to calculate the approximate volume of a voxel, we approxi-

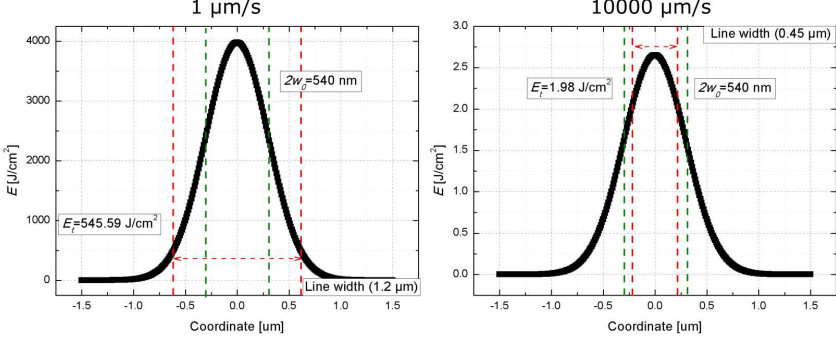


Figure 3.3:  $E_t$  in the center of the line during formation at  $v$  of  $1 \mu\text{m/s}$  and  $10000 \mu\text{m/s}$  and 10% below the damage threshold of the polymer. A substantial difference in  $E_t$  and the resulting decrease in line width as  $v$  is higher.

mate the shape of a voxel to the one of an ellipsoid in accordance with the dynamics of voxel formation. Then, the volume of a voxel  $V$  is [Fig. 3.4 (a)]:

$$V = \frac{4}{3}\pi abc = \frac{4}{3}\pi \frac{D}{2} \frac{D}{2} \frac{L}{2} = \frac{1}{6}\pi D^2 L. \quad (3.1)$$

Consequently, volume  $V$  decreases around 13.7 times when velocity  $v$  is increased from  $1 \mu\text{m/s}$  to  $10000 \mu\text{m/s}$  [Fig. 3.4 (b)] following dependencies shown in Fig. 3.1 (b). While this is a substantial decrease,  $v$  increases 4 orders of magnitude, completely mitigating the possible drop in structuring rate due to the consequentially smaller voxel volume. For instance, considering a cube of  $1 \times 1 \times 1 \text{ mm}^3$  size and half voxel overlap (usually used to make sure that the structure is mechanically strong and not layered), the fabrication time with  $1 \mu\text{m/s}$  and  $10000 \mu\text{m/s}$  would be 246903 and 174 hours respectively. It is more than 4 orders of magnitude faster in the case of the highest tested translation velocity. This can be explained by the increase of structuring rate  $R$  as  $v$  is raised.  $R$  is the volume of a line fabricated at a given translation velocity per second. In that case, voxel's  $D$  and  $L$  are taken to calculate the area of an ellipse resembling a cross-section of a voxel and then multiplied by the distance that focal point travels at the given speed ( $R=0.25\pi DLv$ ) [Fig. 3.4 (a, c)]. It allows estimating the overall structuring rate in terms of volume per time if it is multiplied by the projected structuring time and *vice versa*: dividing the overall volume of an object by  $R$  allows calculating manufacturing time of an object (making an

assumption that there is no overlap and/or unnecessary movements with closed shutter during fabrication). Similarly, if this quantity is divided by the volume of a single voxel, the rate in voxels per second can be calculated. This way,  $R$  is normalized to  $V$  giving the rate in voxels per second [Fig. 3.4 (d)], reaching more than  $\sim 32000$  voxels/s. The gain in throughput in terms of both  $R$  and voxels/s is still maintained regardless of the decreasing voxel size. Therefore, maximizing  $v$  is an effective way to enhance the overall yield of 3DLL printing. Nevertheless,  $V$  saturates at a high value of  $v$  as the polymerization reaction rate will be insufficient for the DLW. Nevertheless, after extrapolating  $V$  for high values of  $v$  it was noticed that this does occur only for tens of  $\sim \text{cm/s}$  or more (for SZ2080 pre-polymer), which are challenging values to achieve for most 3DLL setups even with synchronization.

While structuring rates of voxel volumes per time is a good indicator of the expected throughput of 3DLL, real fabrication of complex 3D structures requires some additional considerations. Namely, one must consider the voxel overlap required to produce a continuous structure as well as stage movement between different parts of the object.

In order to prove these considerations, we use gradient chain mail as a model structure. Such structure was chosen as it combines features from several  $\mu\text{m}$  to more than a hundred  $\mu\text{m}$  that are also intertwined, thus posing a considerable challenge to fabricate. Additionally, there is a lot of empty space between features forcing a substantial amount of movement with a closed shutter. The overall width of the structure is 1 mm, the internal radius of the largest ring is around 100  $\mu\text{m}$ , while the smallest is around 5  $\mu\text{m}$  [Fig. 3.5 (a)]. Support walls are needed in order to attach the ring structure to the glass substrate, yet they can be fabricated with different parameters than the rings (namely lower overlap in the vertical direction) and therefore will be excluded from the discussion.

The STL file of a 3D object is hatched in XY and sliced in Z coordinates, respectively. These can be independently set to proportional or different steps resulting in the directional fabrication accuracy/throughput. This is useful as structure fidelity for different parts of the object might be compromised for enhanced throughput. For this calculation, however, we will use the only chain. The volume of the chain structure is 1280410  $\mu\text{m}^3$ . The structuring rate using  $v = 10000 \mu\text{m/s}$  is 5667  $\mu\text{m}^3/\text{s}$ . Therefore, theoretically, in order to fill all the volume of the object (as shown in Fig. 3.5 (b)), it should take 225 seconds or around 3 and a half minutes. However, in order to achieve a continuous and relatively smooth surface, the

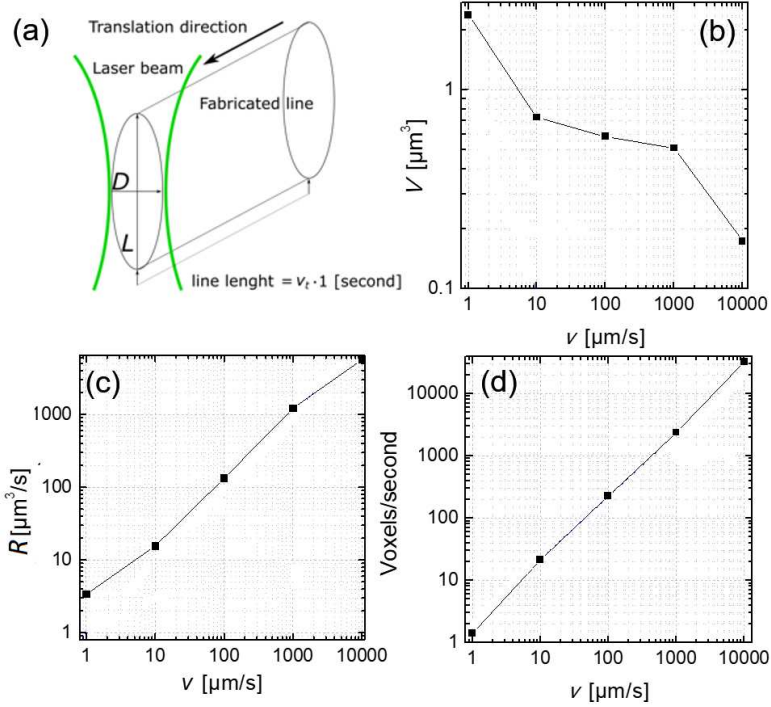


Figure 3.4: (a) – visualization of a single voxel, line and transverse  $D$  and longitudinal  $L$  dimensions of fabricated features; (b)-(d) are voxel volume  $V$ , structuring rate  $R$  and voxels/second dependencies on the translation velocity  $v$  respectively. While the  $V$  drops when  $v$  is increased, the  $R$  and voxels/second increase dramatically.

slicing and hatching steps of  $0.3 \mu\text{m}$  have to be used, increasing the real structuring duration. Furthermore, there are huge gaps between different parts of the structure that are covered by the positioning system with a closed laser shutter, creating a lot of movements that do not result in any volume polymerized. If this is done in a standard raster scanning fashion using translation stages and galvo-scanners, the time needed for fabrication is around 2 hours, although synchronization is on and  $v = 1 \text{ cm/s}$  is used. Further optimization is possible by applying the "traveling salesman" algorithm. It is a classical mathematical algorithm, allowing to deduce the fastest possible route between parts of the structure which needs to be produced with minimal unnecessary traveling between them [223]. After

applying it, stage movement is minimized and the fabrication time can be reduced to 26 minutes [Fig. 3.5 (c)]. Although this result is impressive, it is still substantially longer than the time given by theoretical calculation.

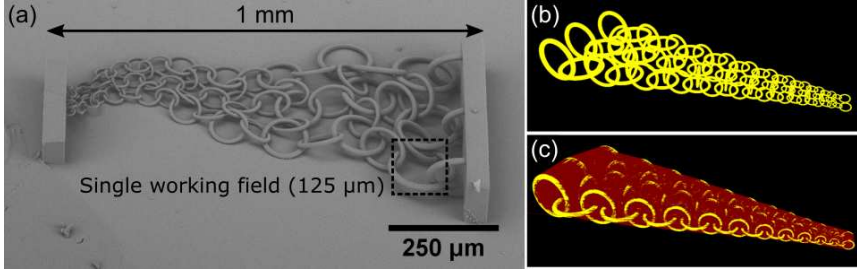


Figure 3.5: (a) SEM micrograph of 1 mm long gradient chain-mail (with support walls) showcasing the capability to produce a relatively smooth surface with features that range from  $\mu\text{m}$  to hundreds of  $\mu\text{m}$ . A single working field of NA=1.4 objective ( $125 \mu\text{m}$  square) is added for the reference, showcasing that the biggest rings would not fit in it. (b) Focal point movements if only the rings are fabricated. (c) Image showing all the movements needed to produce such structure, including ones with an open shutter (yellow) and with a closed shutter (red). As movements between different parts of the rings take up a significant portion of the laser beam repositioning between scanning, the time needed to create such structure is 26 minutes, in comparison to 3 and a half needed if only the volume is filled.

It is important to note that theoretically calculated and real fabrication durations converge when the complexity of the structure is decreased. For example, if the object is a simple cube, then the number of slicing and hatching steps is minimal. Furthermore, optimization of the production algorithm, for instance, making rings in chain-mail not by linear slicing, but by scanning in circular movements, can further decrease structuring duration. However, there are some inherent limitations. For example, the creation of continuous vertical rings by drawing circles in the Z direction is impractical as a shadowing effect would impinge the quality of the ring fragments, as the incident beam path would need to align with already exposed material resulting in beam distortion and overexposure [61].

In order to demonstrate the full potential of the presented structuring strategy, a benchmark meso-butterfly was produced [Fig. 3.6]. The goal behind the design of this structure was to combine all the relevant microstructures that can be produced using 3DLL at different size scales. The

overall wingspan of the structure reached 1.3 mm, making it clearly visible with a naked eye. Rhodamine was mixed into SZ2080 to make the material bright purple color, at the same time providing functional properties of high-yield fluorescence [224]. The 14  $\mu\text{m}$  thick microcantilever-like antennae were fixed to the head. Eyes consisted of an array of few- $\mu\text{m}$ -diameter functioning lenses arranged in a semi-random pattern, yet still showing high surface smoothness. Inspired by real butterflies, wings consisted of nanolattices, which in this case were arranged in the fcc geometry. The line width was  $\sim 650$  nm which meant that they do perform as photonic crystals and are just a demonstration of sub- $\mu\text{m}$  feature size in a structure with over-mm overall size. The  $v = 1$  cm/s, combined with dynamic slicing and hatching allowed to achieve a printing time of 2.5 hours. Overall, it shows true mesoscale capabilities of millimeter-sized structures out of functional material with true nanometre features and optical-quality level surface roughness in critical areas such as microlenses.

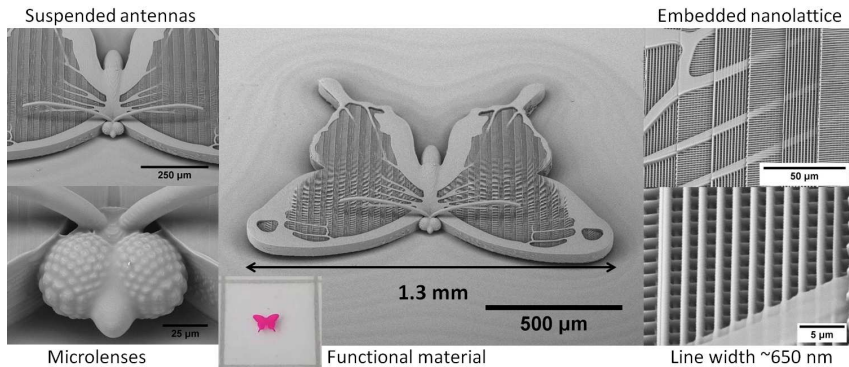


Figure 3.6: A meso butterfly, created to demonstrate true mesoscale capabilities of synchronized linear stages and galvo-scanners. With an overall wingspan of 1.3 mm it combines cantilever-like antennae that are a few  $\mu\text{m}$  thick and hundreds of  $\mu\text{m}$  long, functioning microlenses and woodpile nanolattices in wings with a single line width of 650 nm. It is made out of functional material: SZ2080 doped with Rhodamine fluorescent dye.

### 3.1.1. Expanding Throughput with Different Focusing Optics

Different 3DLL applications might require voxel with either higher-resolution or higher volume for faster structuring if feature size is not an issue. Simple modeling by using eq 1.12 shows that expanding voxel size, especially in the Z direction, is relatively easy just by changing the NA of the objective [Fig. 3.7]. This effect can be greatly exploited if higher structuring rates are needed.

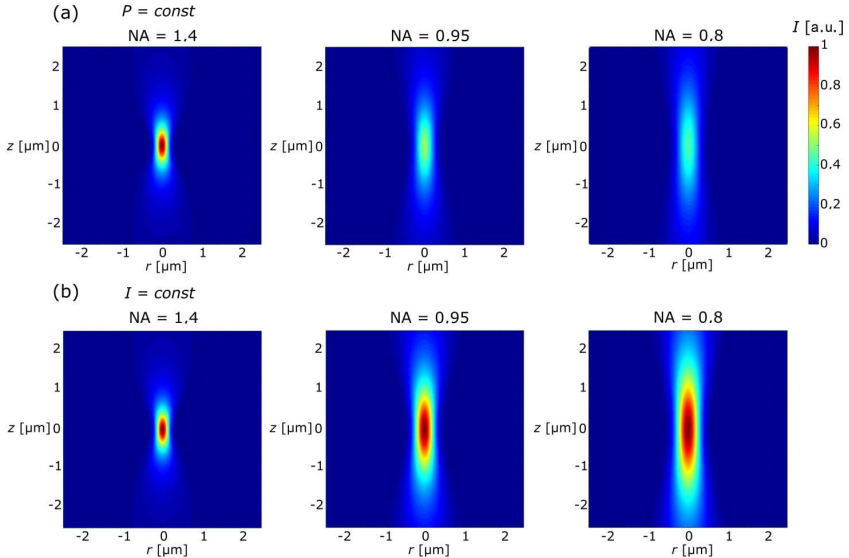


Figure 3.7: Theoretically modeled voxel sizes achievable with objectives with  $\text{NA}_1 = 1.4$ ,  $\text{NA}_2 = 0.95$ , and  $\text{NA}_3 = 0.8$ . (a) Shows distributions with  $P$  being constant, while (b) with  $I = \text{const}$ . Clear expansion of voxel, especially in the longitudinal direction, with the decrease of NA is visible.

Here we apply the resolution bridge technique [134] to measure feature sizes produced with 1.4, 0.95, 0.8, and 0.45 NA objectives [Fig. 3.8 (a)].  $P$  (after the objective) is used as the main laser radiation parameter. Other laser parameters:  $\lambda = 515$  nm,  $f = 1$  MHz,  $\tau = 250$  fs. While  $P$  does not say much about nonlinear process peculiarities, it is a lot easier to measure during an experiment and can be used directly in the setup for  $P$  dependant resolution calibration. Standard hybrid organic-inorganic pho-



topolymer SZ2080 with 1% w.t. IRG was used for the experiment [34]. Such measurement basically forms a calibration curve for size dependence on  $P$  and NA which is crucial from a structural engineering and fabrication strategy point of view. In all cases  $v = 1$  cm/s.

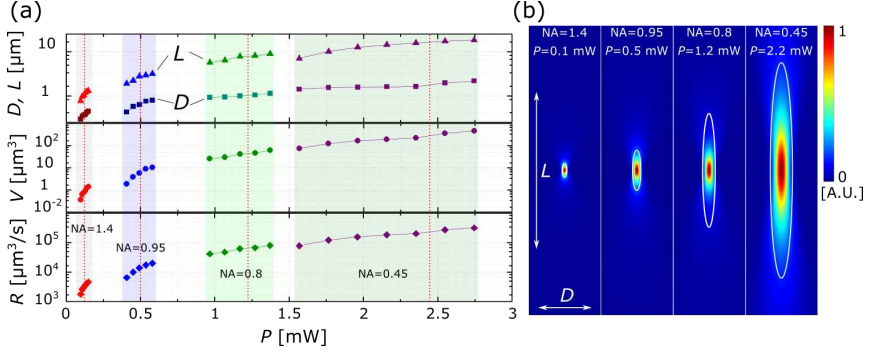


Figure 3.8: (a) - measured transverse ( $D$ ) and longitudinal ( $L$ ) dimensions of lines fabricated with 1.4, 0.95, 0.8, and 0.45 NA objectives and corresponding voxel volumes ( $V$ ) and structuring rates ( $R$ ). The smooth feature size transition between objectives with different NAs allows to easily choose the fabrication resolution/throughput combination needed for a particular experiment. The colored areas show fabrication windows of each objective. (b) - comparison between modeled  $I$  distributions in focal point with measured line dimensions (white oval). Distributions are normalized to the highest value in each case. Red dashed lines in part (a) shows what powers were used for modeling. These are also listed in part (b). A good agreement between theory and experiment is evident with  $I_{th} = 1.7 \pm 1$  TW/cm<sup>2</sup>.

Acquired results allow us to estimate that  $D$  can go from sub-wavelength  $0.3 \mu\text{m}$  with  $\text{NA} = 1.4$  while operating near the  $I_{th}$  to  $2.18 \mu\text{m}$  with  $\text{NA} = 0.45$  near the  $I_d$ . The resulting  $L$  values are respectively  $0.77 \mu\text{m}$  and  $18.32 \mu\text{m}$  highlighting the tendency for  $L$  to increase a lot more rapidly than  $D$ . Consequently,  $V$  varies in the range from  $0.036 \mu\text{m}^3$  to  $45.51 \mu\text{m}^3$  with  $R$  being from  $1809 \mu\text{m}^3/\text{s}$  to  $313312 \mu\text{m}^3/\text{s}$ . It means that varying NA from 1.4 to 0.45 and  $P$  in the entire fabrication window, it is possible to smoothly choose the  $V$  and  $R$  in the range of more than two orders of magnitude. This is due to the maximal feature size with a higher NA objective being about the same as the smallest lines with an objective with lower NA. However, care should be taken when fabricating same sized structures with varying objectives as while final feature size might be similar, polymer-

ization degree might differ due to different  $P$  needed to create same sized features. It might influence the mechanical and optical properties of the printed object [199, 13, 225].

Finally, the numerical modeling of intensity distributions with each objective was performed using standard Gaussian distribution and  $M^2$  value of 1.2 (as determined by the producer of the laser). The values were 0.1, 0.5, 1.2, and 2.2 mW for all the objectives from the highest to the lowest NA. The goal was to determine how accurately we can predict feature sizes before the fabrication using just the Gaussian formalism. As shown in [Fig. 3.8 (b)] modeling is relatively close to measured values, especially at smaller NAs. Also, this modeling showed, that it is safe to consider that  $I_{th} = 1.7 \pm 1$  TW/cm<sup>2</sup> for all the given cases. The error of  $\pm 1$  TW/cm<sup>2</sup> appears due to the fabrication window for each objective being different. Interestingly, in all cases, voxel expanded beyond the main focusing volume as the  $I$  at the border of measured  $D$  and  $L$  were in the range of W/cm<sup>2</sup>, i.e. more than ten orders of magnitude smaller. Therefore, it might be considered that when working in the upper part of the fabrication window and the polymer is photosensitized, the reaction easily expands beyond high- $I$  zone due to radical diffusion [178] and some defocusing of a laser beam by already produced polymeric features. However, with  $I$  closer to the bottom of the fabrication window, it is offset by the very small volume where radicals are generated and lower defocusing due to smaller difference between refractive indexes of pre-polymer and modified volume [199]. For this reason, non-photosensitized [34] or even photo-inhibited materials [178] are sometimes used in conjugation to minimal suitable  $I$  when extra-small features are needed. Finally, voxels expand more in the  $Z$  direction when NA is reduced. This can be again attributed to some degree of self-focusing, which was shown to sometimes influence laser material processing. Indeed, in special cases, it makes features extremely elongated [44, 62].

Presented results of feature sizes and  $R$  allow comparing 3DLL to SLA. Thinking conventionally, it should be obvious that 3DLL is superior in terms of resolution and SLA can make bigger objects faster. However, as this work showed with relatively small NA, 3DLL  $R_{3DLL}$  can be relatively high (up to 313312  $\mu\text{m}^3/\text{s}$  at  $v = 1$  cm/s). In comparison, micro-SLA can yield feature size of  $D_{SLA} = 7.5$   $\mu\text{m}$  and  $L_{SLA} = 20$   $\mu\text{m}$  at  $v = 500$  mm/s [70]. If we apply the same  $R$  formula, we get that  $R_{SLA} = 58875000$   $\mu\text{m}^3/\text{s}$ . So far nothing unexpected - due to bigger voxel and higher  $v$ ,  $R_{SLA}$  exceeds  $R_{3DLL}$  by two orders of magnitude. However, when dealing with SLA one must not forget the time needed to recast polymer after each structure layer is

made [5]. This means that after each layer is made there is approximately 2-10 seconds down time [226, 227]. Indeed, this is one of the main bottlenecks in SLA, sometimes taking up to 90% of overall printing time [227]. The exact value depends on the viscosity of the material and required layer thickness [227, 228] and can be expected to differ in some special cases. In contrast, the downtime between layers is not present in 3DLL where all material is present from the beginning of the fabrication. To demonstrate the implications of this, let's consider the fabrication of a  $100 \times 100 \times 100 \mu\text{m}$  cube. For simplicity, we will not consider voxel overlap for this example, although it is a very important parameter during 3DLL manufacturing. If we only consider the volume fabrication time, 3DLL should fill such volume in 3.19 s, SLA in 0.02 s. However, keeping in mind that  $L_{SLA} = 20 \mu\text{m}$ , 5 layer recasts will be needed which will last 25 s total if 5 s downtime is considered. In such a case, 3DLL will outpace SLA as it never stops. Interestingly, if the same volume would be fabricated with just one layer recast, the overall printing time would be almost the same. Thus, it means that SLA is benefiting from wide and low structures with minimal layer number, while in the 3DLL case there is no difference. However, if the structure size is increased to  $1 \times 1 \times 1 \text{ mm}$ , even considering 50 layer recasts SLA will be faster than 3DLL (267 s *vs* 3192 s). Therefore, currently, 3DLL can have a throughput edge only in sub-mm printing. The situation is not much different with DMD based SLA printers. On one hand, these 3D printers manufacture the whole layer in one exposure, eliminating scanning [5]. On the other hand, the exposure time of one layer can go from several to tens of seconds depending on how well the material is optimized for the process [229], adding to layer recast times. In contrast, with 3DLL, due to a very sharp and relatively aggressive energy introduction mechanism, even unoptimized materials can be structured relatively fast [230]. Finally, all polymers designed to be used in SLA and DMD have to be liquid for the already mentioned polymer layer recast. 3DLL can employ both liquid and hard materials. In the latter case, the material can act as a support (somewhat similar to SLM/SLS [5]) eliminating the need for supports. This is another area where 3DLL is superior to SLA/DMD. Therefore, it can be considered that currently, 3DLL with low NA objectives can outperform the throughput of SLA and DMD 3DP at sub-mm manufacturing while still being superior in terms of resolution and applicable geometries.

3DLL throughput is expected to grow in the future. Here, making voxels bigger is not an option due to the loss of one of the key advantages of 3DLL – very well-defined 3D structures. An option would be to increase

translation velocity up to m/s. Indeed, with translation velocity reaching 1 m/s and considering the same voxel dimensions as shown in this work  $R = 31331200$  (theoretically calculated value). Then 1 mm<sup>3</sup> cube can be fabricated in around 32 s, outpacing previously considered SLA where total fabrication time was 267 s. Even if layer recast downtime is not considered the result is close, as pure printing time with SLA, in that case, is around 17 s. Such  $v$  can be considered completely realistic for specialized 3DLL setups even now. Indeed, it was already shown that some positioning systems can support such translation velocities if relatively low-quality structures are acceptable (for instance, like biodegradable scaffolds for cell growth [231]). However, relatively slower cm/s level  $v$  is still required for highly complex high-quality structures. Further advances in hardware and software are needed to achieve better printing quality at  $v > 1\text{m/s}$ . New ways to project laser beam might be applied in the future for 3DLL, like polygon scanners [222] or acousto optical deflectors [172]. They might pose some limitations like limited flexibility for polygon scanners or temporal ultrashort pulse distortion in the case of acousto optical deflectors. However, the possibility to achieve translation velocities well into tens of m/s while still using high NA is extremely attractive, potentially transforming 3DLL into technology that is both more precise/flexible and faster than the standard single-photon absorption-based SLA/DLP.

The final question which needs to be addressed is the impact of the material used for fabrication, It can be considered, that at least some of the structure material is the limiting factor for the overall possible size of 3DLL made structures. Indeed, while there are numerous ways to increase throughput, mesoscale structures bring new challenges that are not as important in micro- and nanoscale. The first is shrinkage. All 3DLL processable materials shrink after fabrication due to changes in chemical composition and cross-linking. The variation is huge, going from tens of % [232] to just a few % [181]. This means a loss in shape precision, possible internal stress, and cracks. Nevertheless, for some applications, like biology, it is not an issue, as even deformed structures can still perform their designed task. Another consideration is the structure height. As we saw talking about SLA/DLP the material layer thickness in these technologies has to be only as thick as the thickness of the layer which needs to be fabricated. However, in all cases of 3DLL usage, all of the material needed to print has to be present during the manufacturing process. This means, that for viscous materials a reservoir has to be constructed, while hard gels, like SZ2080 used in this work, multi-layer pre-bake has to be realized. At the

same time, one has to take into consideration that high NA objectives have relatively short working distance. For instance, the 1.4 NA objective used in this work has a working distance of only  $\sim 360 \mu\text{m}$  [233]. Thus, higher structures have to be fabricated segment by segment in the Z direction and then somehow joined, or liquid resin used, which allows to use so-called dip-in technique [202] or add-ons which allow submerging objectives into pre-polymer [234]. Finally, even if working distance is sufficient aberrations that appear due to sharp focusing to transparent medium might pose voxel deformations further compromising fabrication. Then, something like optics with dynamic aberration correction [235, 236] or spatial light shaping [237, 238] might be needed. Thus, in conclusion, while linear stage and galvo-scanner synchronization bring the possibility to expand 3DLL into mesoscale, further challenges regarding fabrication at this scale, especially related to the height of the structures, will need to be addressed.

## 3.2. Functional 3D Mesoscale Structures

Before going into example structures proving the effectiveness of continuous writing in mesoscale 3DLL fabrication we first have to discuss the main considerations separating it from segment-based manufacturing. Stitching is quite a controversial topic in the field of 3DLL. The problem lies in a somewhat different view by various groups to what exactly should and should not be considered stitch. While it mostly refers to seams between segments fabricated using scanners, it is important to realize that on the technical level it can be considered to go beyond it. Technically, all serial production, to some extent, is based on it. In fact, pulsed laser-based point-by-point manufacturing has multiple levels of stitching. First, single overlapped pulses of laser join together to form a line. Then, lines are joined together. Finally, layers are formed one by one. However, while all of these joining points can be considered "stitches", practically it has minimal impact. When fs laser is used for 3DLL, distance traveled between pulses rarely exceed 10% of a laser spot, forming continuous line [168]. Line and layer overlap depends on the application and has to be in accordance with the functionality of an object [239].

Thus, what is the difference between all of the discussed cases and stitching between segments made in a single working field? The answer lies in the material shrinkage and shadowing of a laser beam by already produced structure [Fig. 3.9]. While there are materials with minimal shrinkage, it is rarely smaller than 1-2% [181]. Therefore, when a segment is produced,

it shrinks in the volume of pre-polymer deviating from the desired shape. This happens even if the formed segment is attached to the glass substrate. Such deviations in segments start to accumulate and become visible in the form of stitches. If continuous scanning is applied, the whole layer shrinks together. It still results in some sort of deformation and/or internal stress in the final structure, but in that case, it is distributed more equally in the structure and is not concentrated at the edges of segments. Furthermore, when a high enough segment is produced, it has the potential to block part of focused laser light when another segment is made close by. This effect is called "shadowing", and was observed when using 3DLL to integrate structures to channels [240] or producing different parts of an object in consecutive manner [241]. Additionally, refractive index mismatch between polymerized and unpolymerized resin starts to play a role in the severity of the effect. It is in sharp contrast to continuous writing where the refractive index of the material before and after structuring does not influence the quality. The process is also more pronounced in objectives with higher NAs due to the focusing cone being blocked by the surrounding segments. Overall, it means that additional steps have to be taken either designing the structure or optimizing the manufacturing algorithm in order to avoid these effects [30]. While it can sometimes be done in a relatively simple and generic way, it is still an additional operation that has to be performed in an otherwise relatively straightforward fabrication process. Finally, stitching can be realized by making all the segments of a single layer, i.e. avoid block stitching and shadowing. However, then the inertia of mechanical axes becomes a limiting factor yet again. In comparison, during synchronized manufacturing, the whole layer is produced in one run with minimal segmenting and inertia while maintaining maximal possible speed. Thus, shadowing is completely averted and shrinkage is distributed through the whole structure.

But are there general guidelines when inter-segment stitching becomes unacceptable? The answer depends on whether the stitching compromises the functionality of an object. Indeed, scanners still offer an advantage of faster and simpler fabrication if mass production of relatively small objects is required or stitching-associated defects are not an issue. However, in some cases, stitching can completely compromise the functionality of an object. This is extremely relevant for optics [32, 33] and for micromechanics [29]. In the latter case, the stitching would create mechanical weaknesses in the structure. In order to demonstrate that, an example structure of 3D gyroid was made. In the stitched structure, clear cracks are visible [Fig. 3.10

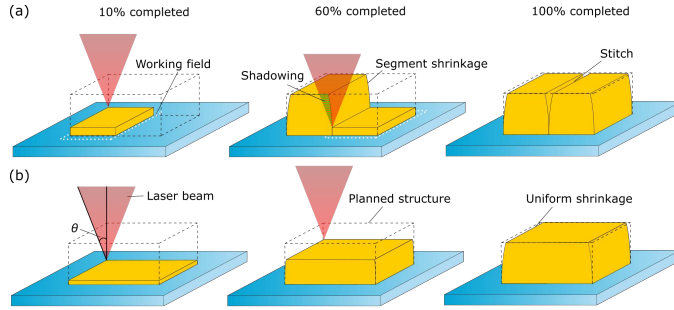


Figure 3.9: Schematics explaining how shadowing and shrinkage influence the severity of stitching defects. The simple bulk structure will be considered, with the pre-fabrication model denoted in black dashed lines. Using only scanners two segments have to be produced due to the limited working field (shown as white dotted lines) (a). After the first segment is produced it is blocking some of the laser beam needed to properly structure the bottom of the next segment. This effect is called "shadowing" and is marked as green dashes on the laser beam. The severity of shadowing depends on  $n$  mismatch between polymerized and unpolymerized resin, the height of the first segment, and particular objective (as  $NA = n \sin\theta$ ). Furthermore, each segment shrinks independently from the previous one making their connection harder. In the continuous writing case (b) layers produced after each other do not obstruct the light and the shrinkage happens uniformly. Thus, while sides of the structure might be somewhat distorted depending on how much the material shrinks, the overall structure has a lot better quality. Also, if all other parameters are chosen appropriately structure's quality is not inherently influenced by such parameters as refractive index mismatch or the NA of the objective.

(a)], undermining the main idea behind 3D printed gyroid structure - extreme mechanical resilience with minimal weight [242]. This applies to all other objects tested in this work. Therefore, stitching has a tendency to severely undermine mesoscale structures. Stitches are nm- $\mu$ m level defects that potentially prevent structures from having some highly desirable functionality. On the other hand, continuous writing provides a good quality structure that does not have any inherent manufacturing-induced defects [Fig. 3.10 (b)]. Thus, the usage of synchronized positioning for continuous writing is a powerful way to supplement galvo-scanners that can be used alone if a structure is small or printing speed is more important than

possible mechanical defects. This is especially true because each system equipped with both scanners and linear stages can always be used in an unsynchronized manner, meaning that the user can freely choose between using just scanners for higher speed or scanners synchronized with linear stages for a higher quality of mesostructures. The second option should be used when stitching induced defects would be detrimental for application.

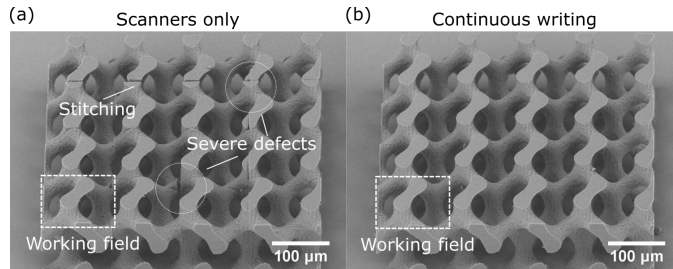


Figure 3.10: A 3D gyroid structure printed with scanners (a) and using continuous writing *via* synchronized linear stages and galvo-scanners (b) at  $v = 1$  cm/s. Objective - 63x 1.4 NA, working field ( $125 \times 125 \mu\text{m}^2$ ) is marked as a white dashed rectangle. Clear stitching is visible in part (a) with some defects resulting in the near breaking of the objects. These appear due to segment shrinkage and shadowing of already made parts of the structure. It completely compromises 3D gyroid structure because it should be extremely mechanically strong. In contrast, using continuous writing, there are no such defects and the structure is of superb quality.

We will show several examples of mesoscale structures that could not perform their functionalities if stitching would be present. The choice of the structures is motivated by their applicability for two highly promising fields - micro-optics and micromechanics. We will aim at demonstrating their functionality (i.e. focusing properties for micro-optics, the movement for micromechanics) as it is the best proof that continuous writing can be considered suitable for 3DLL structure fabrication.

### 3.2.1. Refractive Optics

While integrated micro-optics is one of the main driving forces behind 3DLL, most of the structures presented so far in the literature do not exceed a few hundred of  $\mu\text{m}$  in size [100, 243]. The limiting factors preventing an increase in size are a combination of necessity to use high layer overlap



during printing, which is needed to achieve surface roughness sufficient for optical use, and demand for homogeneity of a structure, as any internal defects, for instance, stitching, would be unacceptable [33]. With continuous scanning both of these problems are eliminated because high layer overlap in the lens does not cause a massive increase in printing time as the translation velocity can be in the range of  $\sim$ mm/s, depending on the quality requirements. Furthermore, stage synchronizations (including in the Z axis) assure that the structure is homogeneous. SEM analysis showed no significant defects on the surfaces of these objects [Fig. 3.11 (a)].

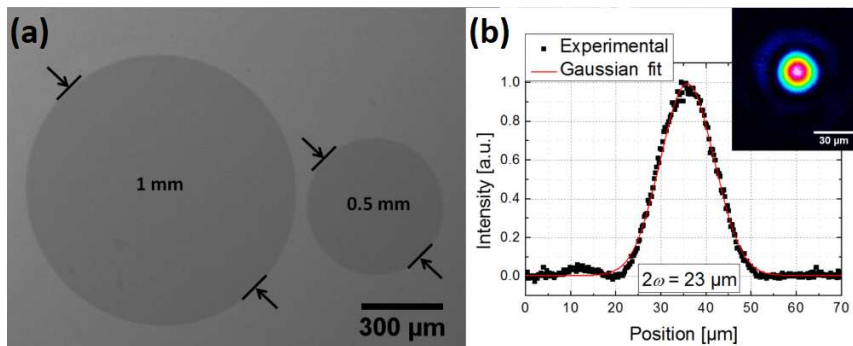


Figure 3.11: (a) - SEM images of 0.5 and 1 mm diameter lenses showing a good surface finish. (b) - intensity distribution in the focal point of 0.5 mm lens showing the good, theory matching Gaussian distribution. The surrounding low-intensity ring is a result of diffraction from the lens sides, as testing HeNe laser beam diameter was 3 mm.

To truly assess if the fabrication was successful focusing properties of the lens were measured. Indeed, while the surface and shape of the lens might seem adequate, internal stresses or some other polymerization related defects might have compromised its focusing properties. After measuring focusing properties, it was noted that the laser beam formed by such lens in the focal plane is Gaussian-like [Fig. 3.11 (b)]. However, while increasing the size of the lens, other fabrication unrelated problems occur. All the polymers used in 3DLL have some degree of inherent shrinkage during fabrication. The material used in this study, SZ2080, was specifically designed with minimal shrinkage [181], yet at these scales, even this material could not avoid all the associated problems. The 1-2% of shrinkage can be more or less ignored in lenses that are tens-of- $\mu$ m in size because deformation caused by this effect is in the range of tens to hundreds of nm - smaller

than the voxel used for fabrication. In mm-sized objects, the deformation might exceed the  $\mu\text{m}$  range, which means that it becomes an issue that has to be addressed.

Due to shrinkage considerations, a further question was how big the lens can be made before shrinkage compensation becomes mandatory. The same combination of SEM analysis and focusing measurement was used. It turned out that at 2 mm diameter lens started to have severe signs of astigmatism [Fig. 3.12]. What is more, with increased printing time ( $\sim 12$  hours) repeatability becomes an issue due to possible random vibrations of the system as it was not tuned to have any special vibration dampening. Such defects are enlarged by the shrinkage and are more prominent in bigger lenses. Therefore, for mm-sized lens fabrication specialized setup with advanced shrinkage compensation is necessary. It was beyond the scope of this study.

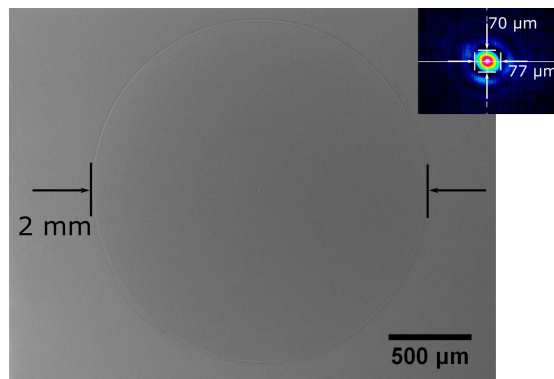


Figure 3.12: SEM images of 2 mm lens. While the lens quality seems good (no defects on the surface), testing of focusing relieved astigmatism. This is due to the shrinkage of the lens.

One way to minimize shrinkage deformations is by limiting the volume of the structure. In optics, this can be achieved by applying the Fresnel lens geometry [Fig. 3.13]. Then the volume of the optical element is minimized at the same time directing all the force of shrinkage towards the substrate. Zone height was set at  $5 \mu\text{m}$  to make it close to the height of 1.4. NA voxel. Then each zone can be produced with a single laser scan. Chosen focal distance -  $100 \mu\text{m}$ . As expected, the lens focused into relatively small spot sized  $\sim \mu\text{m}$  and the focal distance was measured to be  $\sim 100 \mu\text{m}$  corresponding well to one set in the lens design. In addition to the lowered influence of shrinkage repeatability of such elements was also improved in comparison to standard lenses as shrinkage was enlarging defects in standard lenses.

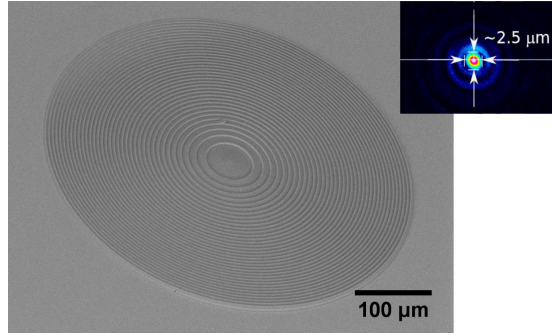


Figure 3.13: SEM image of 500  $\mu\text{m}$  diameter Fresnel lens. Good surface quality and focusing properties are observed.

### 3.2.2. Free-form Mechanical Structures

Polymers used in 3DLL can be considered rigid unless special elastomer-based materials are used [244, 245]. However, downsizing 3D features and applying special geometries can yield deformable 3D printed structures. This was exploited in micromechanics [14, 196] and metamaterials [13, 246]. Yet objects of this kind demonstrated by other groups are in the size range of  $\sim 100 \mu\text{m}$  as it fits into a single working field of a standard high NA objective. The goal of this investigation is to determine what are the peculiarities of producing 3D meso-mechanical structures.

We began our investigation by fabricating an mm-sized 3D spring. Springs are used in a huge variety of different fields and the possibility to print them on demand at any size is an interesting prospect for the technology as it expands possible applications to mm-sized actuators with the necessity for a component to return to its original position. We chose 1.5 mm diameter, 0.7 mm height, and single helix two-turn design with the helix itself being 0.5 mm tall,  $80 \mu\text{m}$  thick in the Z direction, and  $120 \mu\text{m}$  in the horizontal plane. With such parameters, 20x 0.45 NA objective was used as the resolution requirements were not high. Continuous writing was also employed to avoid any weak points in the supporting disk or the helix. The print was successful, with spring showing good quality [Fig. 3.14 (a)]. At the same time, the distinction of each printed layer was visible. We call it "layering". It appears due to the relatively big slicing step (in this case  $9 \mu\text{m}$ , which is close to 50% of  $L$ ) allowing to maintain maximal possible  $R$ . A deformation experiment with the spring was performed to test if layering has any adverse impact on the structural integrity of the element [Fig. 3.14

(b) and (c)]. Deformation of up to  $100\ \mu\text{m}$  (20% of the overall height of the helix) was shown to have no negative impact on the mechanical quality of the structure. Furthermore, deformation was repeated 10000 consecutive times. Even after such a huge amount of compressions spring showed no signs of damage. Therefore, we showed that layering does not have an inherently destructive effect on the 3DLL made springs and such objects can sustain enough deformation cycles to consider them useful for real world applications. Interestingly, the demonstrated spring is a good example of layering having minimal impact on the performance of the object. It has clear layering (i.e. "stitching" in the Z direction) but it has no negative impact on the mechanical functionality showing the possible flexibility of 3DLL making a compromise between structuring time and some of the qualities of the structure. In contrast, such layering would not be acceptable in microoptics [20, 168].

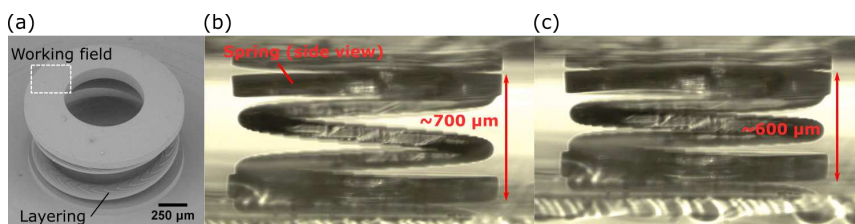


Figure 3.14: (a) - an SEM image of a 1.5 mm diameter spring with a working field of  $\text{NA} = 0.45$  objective shown. Layering in the spring is visible.  $100\ \mu\text{m}$  compression (from  $700\ \mu\text{m}$  in (b) to  $600\ \mu\text{m}$  in (c)) can be carried out 10000 times without any adverse effect to the structure, showing that layering is not a severe problem in such structures.

Deformation of 3DLL structures is a widely exploited phenomena for micromechanical applications [13, 14, 196, 246]. However, the next step is the introduction of special intertwined 3D geometries allowing movement of different parts of the object after it is printed [247, 248]. 3DLL is a superb manufacturing method of such structures as these could be of any required shape, produced at specific sample positions, and have precision down to tens of nm [189]. It was used to produce various rotors [247] or assembly-ready components [248]. Nevertheless, most of these structures are still less than a hundred of  $\mu\text{m}$  in overall size. Here we present hinge-based micromechanical structures with overall size up to millimeters, while relying on micro-sized features for movement and keeping the whole object

together. The motivation to produce these structures comes from the needs of the field of micro-robotics as well as biomimetics.

First, a spider structure was printed. It had 8 legs attached to the glass substrate (the body was free hanging), each consisting of 3 segments, joined together by micro-hinges. Because SZ2080 is a hard gel, different parts that are not joined together or to the glass substrate can be printed without additional supports. This is somewhat similar to SLS/SLM where unused metal powder acts as the support for features that are being printed. Therefore, the whole manufacturing process is extremely straightforward. No special attachment optimization or supports are needed creating a sharp contrast to cases where liquid resin is used. As structures had to be freely movable after printing, 1.4 NA objective was chosen because it provides the voxel with the lowest and best defined  $L$ . Nevertheless,  $P$  of 80% of fabrication window was chosen to exploit the highest  $R$  achievable with 1.4 NA. The distance between separated parts of the hinge was put apart by  $5\ \mu\text{m}$  in the model to ensure easy development and to increase the range of movement. The SEM of the acquired structure is shown in [Fig. 3.15 (a) and (b)]. As the working field of the  $\text{NA} = 1.4$  objective is a  $125\ \mu\text{m}$  square even a single leg segment would not fit into it [Fig. 3.15 (a)], meaning that scanner-only printing could potentially yield stitching in critical parts of the object. During post-development manipulation, a probe was used to push the spider's body and proved that it is movable [Fig. 3.15 (c)]. Due to the chosen hinge geometry and the angle between legs, only limited (tens of  $\mu\text{m}$ ) movement was possible, making it barely visible with optical imaging. Spider broke during more aggressive manipulation.

Next, a structure with more moving parts was modeled - a 2 mm long squid with 8 tentacles, attached to the substrate at the body [Fig. 3.16 (a) and (b)]. The same 1.4 NA objective was applied with gaps in hinges in the Z direction being no smaller than  $5\ \mu\text{m}$ . For more convenient printing, tentacles were modeled to be straight. The tentacles were held together by  $10\ \mu\text{m}$  pins, allowing free and highly articulated movement. Additionally, gecko-inspired suction cup-like structures were modeled on the legs. It shows that different types of potentially functional geometries at different size scales can be produced on the same object during the same fabrication step. After development, the squid was left in the developer, and the probe was used to create meniscus which in turn moved the structure [Fig. 3.16 (d)]. Tentacles proved to be highly articulated and strong enough to survive the manipulation without breaking. Finally, the same model was stretched by the factor of 4.5, making the overall printed length 10 mm [Fig. 3.16

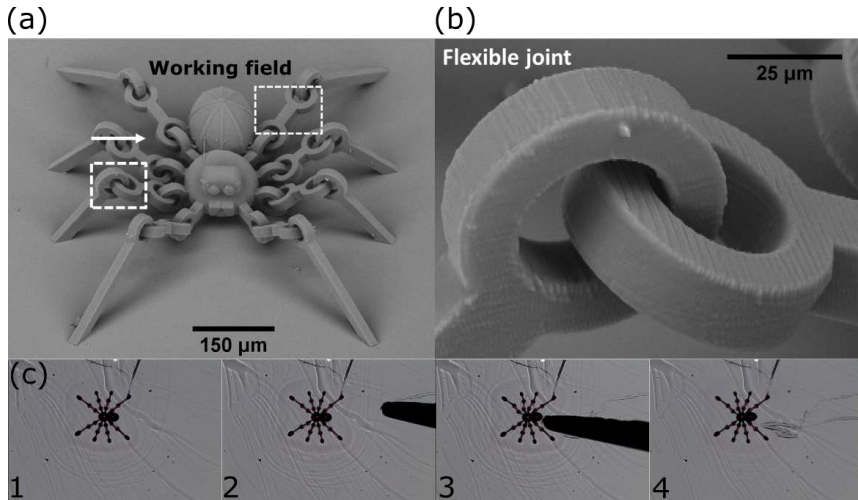


Figure 3.15: (a) - an overall view of the movable spider with flexible joint enlarged in (b). (c) shows the slight movement of the spider after it is pushed with a metal probe. Movement distance is in tens of  $\mu\text{m}$ , best visible at the slight difference at the bend of the top left leg. The working field of a  $\text{NA} = 1.4$  objective (side length -  $125 \mu\text{m}$ ) is also provided, showing that even a single leg fragment would not fit into it if only scanners would be applied.

(c)]. In order to compensate for the sharp increase in the volume of the structure, the objective was changed to  $20\times 0.45$ . Due to uniform scaling, the gap in the model in the  $Z$  direction grew from  $5 \mu\text{m}$  to  $22.5 \mu\text{m}$ .  $L$  at the parameters used was  $15 \mu\text{m}$  which was sufficient to avoid different segments of the tentacles being attached to each other during structuring. Working fields of the  $\text{NA} = 1.4$  and  $\text{NA} = 0.45$  were plotted on SEM images of both squids [Fig. 3.16 (b) and (c)]. In both cases, even a single segment of tentacle would not fit into it. Thus, we can conclude that continuous writing strategy achieved *via* synchronizing galvo-scanners and linear stages is mandatory for defect-free 3DP of mesoscale mechanical structures.

There were numerous attempts to apply 3DLL for microrobotics [249, 250]. Straightforward manufacturing of intertwined structures puts an interesting prospect in the field as these hard objects can act as a "bone" structure for a complex microrobot that could then be propelled by some other means. Therefore, due to the 4D structuring capability of 3DLL [16, 196], elastic materials could be printed on such hard parts, creating a bio-mimicking

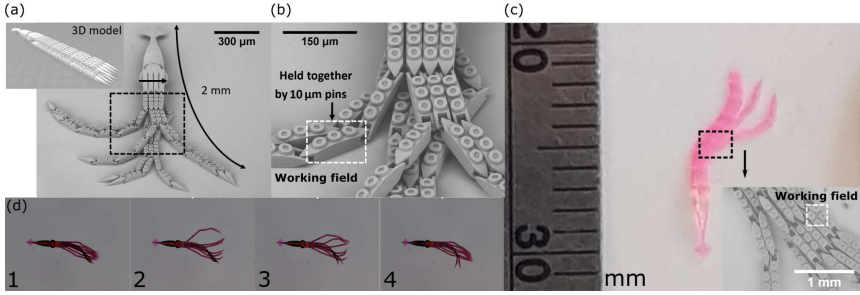


Figure 3.16: (a) - an overall view of the movable 2 mm long squid with flexible tentacles with gecko-like suction cups held together by 10  $\mu\text{m}$  pins (b). Inset in part (a) shows the 3D model used for fabrication. (c) - 10 mm squid printed using the same model but stretched *via* the software 4.5 times. Inset shows an enhanced view of tentacles proving very good manufacturing quality. (d) shows floating of squid tentacles after they are moved by meniscus formed in a thin layer of liquid. Working fields of  $\text{NA} = 1.4$  and  $\text{NA} = 0.45$  objectives (side length - 125  $\mu\text{m}$  and 350  $\mu\text{m}$  respectively) are also shown in part (b) and (d) as white rectangles. It is evident that a single segment of tentacle barely fits in them for both small and big squid.

system. Having in mind fast developments in the field of photostructurable artificial muscles [251, 252, 253], it points to a very powerful future application of the technology. As shown in this work, sub-cm stitches 3D meso-printing with the on-demand resolution is easy to realize in the current state of the art 3DLL systems.

### 3.3. Conclusions

1. Usage of linear stages with synchronized galvo-scanners that rapidly correct positioning error of the linear stages allows employing 1.4 NA objectives to fabricate stitch-free mesoscale structures with single feature size down to several hundred nm and structuring rate of  $\sim 1800 \mu\text{m}^3/\text{s}$  ( $\sim 32000$  voxels/s).
2. Single-pulse overlap can reach up to 10% of laser spot size and more if cm/s level  $v$  is used with a sub-MHz fs laser, potentially limiting a further increase in throughput if amplified laser systems are used.
3. By reducing NA to 0.45 it is possible to expand  $R$  up to  $\sim 31300 \mu\text{m}^3/\text{s}$

which is more than two orders of magnitude higher than what can be achieved with  $\text{NA} = 1.4$  objectives.

4. The synchronization method allows mitigating the stitching defects that are typically based on writing field alignment error and exposed polymer shrinking effects enabling fabrication of highly-complex micro-optical and micro-mechanical 3D mesoscale structures.



## 4. 3D Laser Lithography of Non-Photosensitized SZ2080

In the previous section of the work, it was shown that 3DLL is a powerful tool to produce functional 3D mesoscale structures, including micro-optics. Indeed, it is an extremely active field at the moment [212, 19, 100, 243]. However, one of the key questions concerning the widespread of these elements is their LIDT. Before we could measure it, one additional topic had to be investigated - 3DLL of non-photosensitized material. Indeed, it was shown that in thin-film case such material should be substantially more resilient to laser light [214, 38] and that it is processable with 3DLL [179]. On the other hand, precise quantification on how well it can be structured in comparison to standard material is lacking. Thus, this section of the work is dedicated to answering these questions.

The results presented in this section were published in I and II and articles from approbation.

### 4.1. Fabrication Window and Resolution

In 3DLL, a well-chosen PI can improve fabrication throughput and structure qualities for a material used [254, 255, 256, 257]. The set of parameters needed for structuring material is generally referred to as the *fabrication window*. In essence, when all other experimental parameters are fixed, it is an empirically determined intensity range  $\Delta I$  between irreversible polymerization threshold  $I_t$  and  $I_d$  at which material is optically damaged due to overexposure:  $\Delta I = I_d - I_t$ . In simplified terms, this can be considered to be a range of  $I$  at which structures survive the whole fabrication process, including development. We chose  $I$  (calculated using expression (eq. 1.3)) as the main parameter to quantify the *fabrication window* instead of translation velocity/writing speed  $v$  because changes caused by the former are substantially less noticeable during experimentation than the deviations in

structuring properties induced by even modest variations in the  $I$ . Conventional thinking would let us believe that foregoing photosensitization would lead to the absence of absorption completely preventing photopolymerization or hindering it to the point of inefficient crosslinking and narrow  $\Delta I$ . To determine if that is the case, we designed an experiment in which an array of identical structures was fabricated by varying the  $v$  and  $P$  as these are the two parameters that are the most practical to change during fabrication. The structure chosen for this experiment was a hollow cube with the integrated suspended single lines. With such configuration, it is possible to determine several important factors. First, such an array provides information about the size of  $\Delta I$  by showing which structures are present after the whole fabrication procedure dependent on the set of parameters used. The cube shows if it is possible to produce true 3D structures. Single lines give the possibility to measure fabricated  $D$  and  $L$ . For this reason, it is called a *resolution array*. The outlined result showing  $\Delta I$  achieved with such experiment is shown in Fig. 4.1.

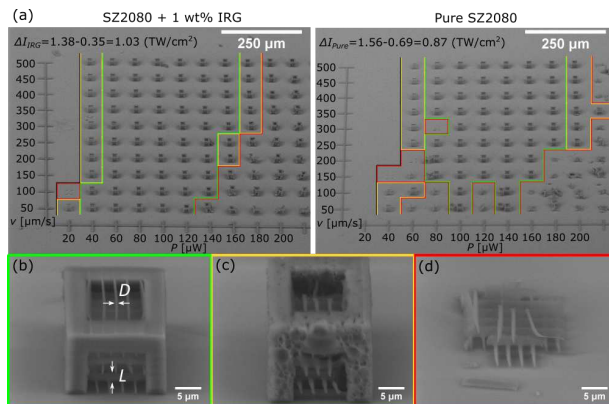


Figure 4.1: (a) SEM images of resolution arrays of photosensitized (left) and non-photosensitized (right) SZ2080. Structures with severe structural damage (red), poor (yellow), and good (green) quality are outlined. The object is considered to have good structural quality if internal single lines are observable and the shape of the cube is not distorted and/or cracked. Average laser powers of the bottom and the top of the  $\Delta I$  are recalculated to the peak intensity  $I_p$  (shown at the top). (b) One of the good quality structures in the array is shown in greater detail;  $L$  and  $D$  marks longitudinal and transverse sizes of the lines. (c) The example of the poor quality structure and (d) the failed one.

Here we discuss the 3DLL of pure materials in detail. The hypothesis

used to explain this interaction is as follows: first, fs laser photopolymerization of an SZ2080 with IRG PI is considered. Light breaks the weak single bonds of the PI molecule, which then creates two radicals PI\* [Fig. 4.2 (a) (1)-(2)] [133]. These radicals then react with pre-polymer molecules *via* double bonds creating the radicalized monomer SZ\* [Fig. 4.2 (a) (3)-(4)]. This initiates a chain reaction and growth of an intertwined polymer matrix, which does not dissolve in the organic solvent. In the case of an SZ2080 without PI, such a reaction is induced when nonlinear absorption occurs. The double bond is broken in the pre-polymer [Fig. 4.2 (b) (1)-(2)], which otherwise would be broken by reaction with PI molecule. Large excitations can build up in the intermediary states because the laser-induced multiphoton excitation rate of pre-polymer species is high in comparison to the thermalization rate, which can be as long as  $\mu\text{s}$  [258]. Photochemical (photolytic) processes are dominant compared to photothermal phenomena due to the absence of detectable thermal effects, such as sample vaporization, boiling, or thermal expansion, which is ensured by the closure of the reaction volume by the surrounding material. High irradiance exposure is sufficient to directly break chemical bonds of pre-polymerized SZ2080 organic constituents, which initialize the formation of an insoluble and rigid organic-inorganic composite.

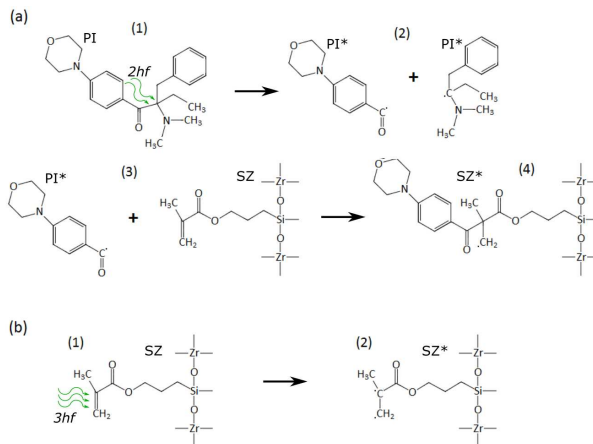


Figure 4.2: (a) Polymerization reactions initiated by nonlinear absorption of PI molecule and subsequent chemical pathways resulting in a cross linked SZ2080. (b) SZ2080 cross linking without PI.  $hf$  is the photon energy.

Data provided in Fig. 4.1 shows several important features of pure SZ2080

in comparison to Data provided in Fig. 4.1 shows several important features of pure SZ2080 in comparison to that containing PI.  $I_t$  required to polymerize pure material is higher by  $\Delta I_t = I_{(t \text{ pure})} - I_{(t \text{ IRG})} = 0.34 \text{ TW/cm}^2$ . The width of  $\Delta I_{IRG}$  is only  $1.03 - 0.87 = 0.16 \text{ (TW/cm}^2)$  (15.5%) wider than  $\Delta I_{\text{pure}}$ . By counting sectors in which structures are of adequate quality, we conclude that pure material provides only a 12.5% lesser survival rate compared to that of the photosensitized polymer. Also, the PI containing polymer provides structures that maintain initial structural features even if parts of the object are greatly affected by the defects caused by the overexposition, while in the case of objects formed from the pure material completely collapse if non-optimal parameters are used [Fig. 4.3 (a)]. This hints that without PI the crosslinking process is not as efficient and provides the final polymer matrix that is considerably mechanically weaker and more brittle. This result coincides well with other works showing that the degree of crosslinking during 3DLL is essential for mechanical and optical properties of finished structures [13, 178, 199]. However, despite this, if fabrication parameters are within the  $\Delta I$ , even advanced micro-optical elements, like suspended microlenses on a tip of the optical fiber, can be fabricated out of pure material [Fig. 4.3 (b)].

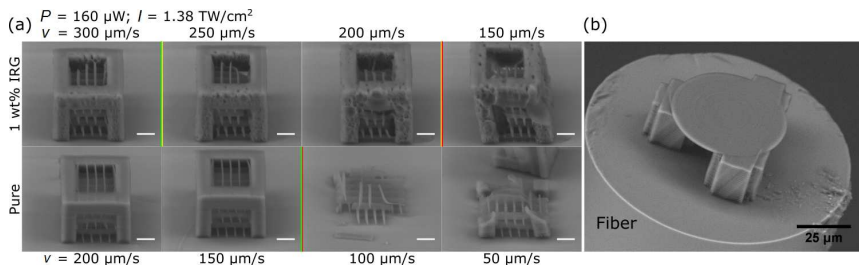


Figure 4.3: (a) Reduction of structural quality in case of photosensitized and pure SZ2080. IRG containing cubes degrade slower and in a more progressive fashion. On the contrary, the structures out of non-photosensitized material break completely as soon as parameters for fabrication are not in the  $\Delta I$ . All scales are  $5 \mu\text{m}$ . (b) Monolithic 3D element on a tip of the optical fiber fabricated out of non-photosensitized SZ2080.

The fact that material can be structured without PI with a  $\Delta I$  comparable to that of photosensitized material is a promising discovery for other scientific fields as well. Earlier studies dedicated to pure material structuring by fs-laser pulses [179, 259] have proved to be complicated and slow. As such pure material can be processed at a relatively high speed ( $\sim\text{mm/s}$ ),

it would become suitable for biomedical applications, where structure dimensions are in the range of mm-cm [15]. Pure material would guarantee superb biocompatibility, which is a key requirement for tissue engineering, especially taking into account biodegradable implants.

Dimensions of the lines inside cubes were measured. Case of  $v = 250 \mu\text{m/s}$  was chosen as it is in the middle of the tested range in both photosensitized and non-photosensitized materials. It revealed that both  $D$  and  $L$  are smaller in pure SZ2080 than in photosensitized polymer [Fig. 4.4 (a)]. This correlates well with earlier findings [133]. It also reveals that  $D$  acquired while using photosensitized material exceeds the calculated spot size. On the other hand,  $D$  of lines produced out of pure SZ2080 are all about the same size as the focus spot. This can be explained by the fact that photochemical chain reactions, in the case of photosensitized material, can expand more easily out of the volume in which nonlinear absorption took place. This is the result of the easier radical generation when PI is present. In the case of pure resist, such a process is less prominent. Also, the aspect ratios of formed voxels are very similar [Fig. 4.4 (b)], thus, showing that non-photosensitized material does not provide any benefit in the control of the aspect ratio of a voxel. This leads to a conclusion that the order and nature of nonlinearity (MPA vs avalanche ionization) do not influence the aspect ratio. It is experimental proof that equations 1.15 and 1.16 are incomplete and does not represent voxel scaling well. To better illustrate this, we provide data for the line aspect ratio for  $500 \mu\text{m/s}$  writing speed in Fig. 4.4 (b) as well.

## 4.2. Structure Quality with Various Focusing Conditions

Considering the application of SZ2080 for micro-optics another important parameter is the surface roughness of the final structures. There are several ways to quantify this property using data from precision measurement tools such as the AFM or very high magnification ( $>50\text{k}$  times) SEM. The most common way to evaluate measured surface elevations is the standard root mean square (RMS) which was chosen for this study. It is common knowledge that if the surface roughness of material is higher than  $\lambda/8$ , it is considered that surface quality is insufficient for use in optics. On the other hand, if the roughness is smaller than  $\lambda/20$ , such material is considered to be suitable for optical applications. We are assuming micro-optical

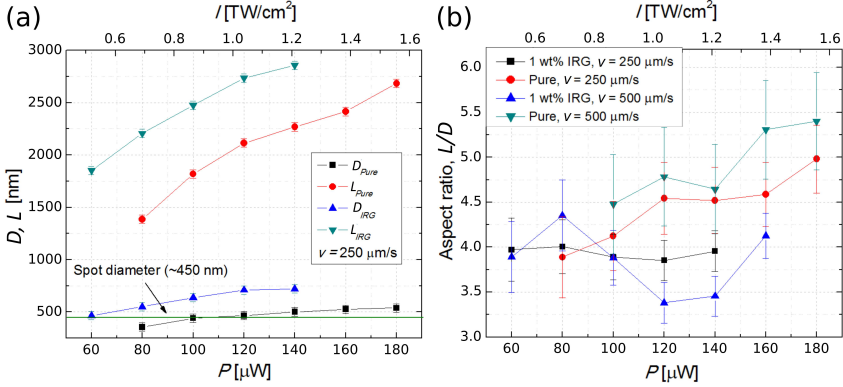


Figure 4.4: (a) Feature width  $D$  and height  $L$  measured in the resolution array at writing speed of  $250 \mu\text{m/s}$ . (b) The aspect ratio of lines produced for cases of  $250 \mu\text{m/s}$  and  $500 \mu\text{m/s}$  speeds. Results show that achieving smaller features is easier with less photoactive pure SZ2080. On the other hand, the voxel aspect ratio does not depend on the material composition showing that the nature of the nonlinear process does not influence this parameter.

elements to be designed for use in the visible part of the spectrum, thus, the lowest operational  $\lambda$  was chosen as  $400 \text{ nm}$ . AFM was employed to measure the surface profile of both pure and photosensitized SZ2080 samples. The geometry was of a flat square slab with a side length of  $100 \mu\text{m}$  [Fig. 4.5 (a)]. Several different values of transverse voxel overlap ( $dx$ ) were used to establish at which condition it was sufficient to achieve optical grade quality of the finished structure. It is important to note that our goal was to determine if optical grade surface quality can be achieved at all with parameters similar to those applied in microlens fabrication and, if so, is it easier to obtain it with photosensitized or pure polymer. For a control/comparison, we used slab produced with one photon polymerization *via* homogeneous radiation of IV harmonic of Nd:YAG laser ( $\lambda = 266 \text{ nm}$ ) - similar to the one used in previous LIDT experiments by our group [38, 214]. After UV exposure samples were also submerged to the developer, following the same protocol as a laser produced samples. It ensured that any difference in the surface profile is a result of the polymerization method and not the sample preparation.

Both polymers had surface acceptable for optical applications. The IRG containing material allows to achieve surface roughness of  $\text{RMS} < 20 \text{ nm}$  with smaller voxel overlap ( $dx = 300 \text{ nm}$ ,  $\text{RMS} = 17.1 \text{ nm}$ ), while in case

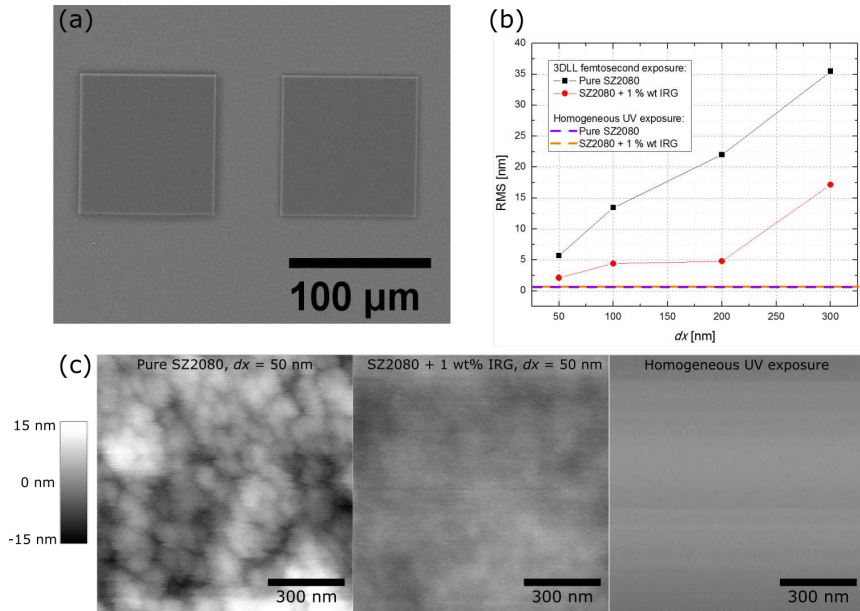


Figure 4.5: (a) SEM micrograph of the measured square polymerized structures. (b) RMS calculated for surfaces fabricated with different  $dx$  for SZ2080 containing PI and in without it. (c) AFM images of surfaces of the pure and photosensitized polymer obtained with the highest voxel overlap ( $dx = 50$  nm) as well as one which was produced via homogeneous UV exposure.

of pure polymer required  $dx$  is 100 nm (RMS = 13.5 nm) [Fig. 4.5 (b)]. The fs laser structured pure SZ2080 is rougher when fabrication parameters are comparable. Even at  $dx = 50$  nm, when surface details of photosensitized SZ2080 become smooth, a non-photosensitized resist still exhibits clear nanofringes [Fig. 4.5 (c)]. This could be explained by the fact that with the non-photosensitized SZ2080 the polymerization mechanism is more chaotic due to different and random process initiation pathways (TPA dominated process *vs* avalanche dominated process), compared to photosensitized sample [179]. It would also explain why such microstructures lose mechanical integrity a lot quicker when applied parameters are out of  $\Delta I$ . It should be noted that difference in roughness is induced by employing 3DLL as control samples of both IRG containing and pure SZ20820 polymerized by UV radiation showed the same flatness with RMS being less than 1 nm.

As mentioned previously, changing NA allows a fast and simple way to tune the voxel shape in accordance with the quality/throughput requirements of the structure. When using the NA = 1.4 objective, the mechanical

quality transition from adequate to destroyed structure is extremely rapid. Thus, the question was if pure material can still be structured with a lower NA objective. In order to answer this question, 3D scaffold manufacturing using two objectives was carried out. Such scaffolds should be relevant for medical applications where bigger features are needed for the robustness of the object while small pores accommodate the cells. Objective usage order: at first the outer part was manufactured using  $NA = 0.45$  objective, after that the inner part was formed with  $NA = 1.4$  objective. The whole structure was fabricated out of SZ2080. In [Fig. 4.6] we see that scaffolds are of high quality with no tearing or other artifacts that could occur during manufacturing processes.

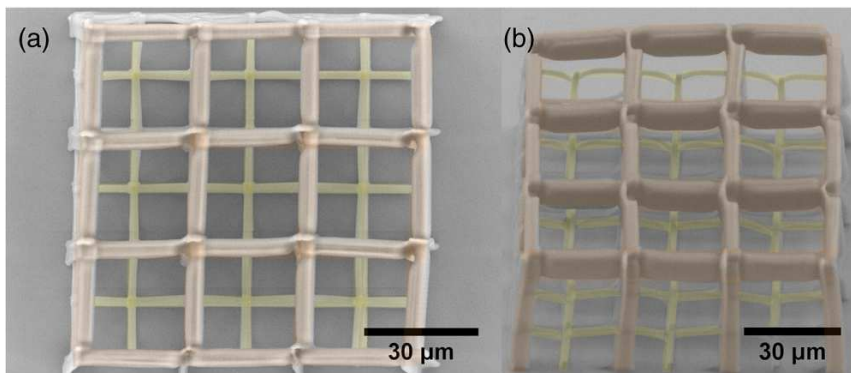


Figure 4.6: 3D scaffold, fabricated using two objectives. (a) Top view; (b) - side view. The outer structure (light brown) was formed first using  $NA = 0.45$  objective. Inner scaffold (yellow) was manufactured afterward using  $NA = 1.4$  objective.

After the manufacturing of the 3D scaffold, we focused on microfluidic element fabrication. Contemporary microfluidic systems are becoming increasingly complex, with 2D structures slowly becoming obsolete. Thus, there is a drive towards true multi-layer 3D microfluidics. 3DLL is a great candidate to produce structures for such applications. Two types of this kind of structures were produced - vertical and horizontal tubes with integrated filters. Systems like that could be used to filter various particles acting as passive microfluidic sorters [17]. The vertical tube is shown in [Fig. 4.7]. The filter was manufactured first, using  $NA = 1.4$  objective, the tube was formed using  $NA = 0.45$  objective afterward. The second microfluidic structure was a horizontal canal on the platform with an integrated filter.



During the manufacturing process, the filter was also fabricated prior to the canal. Objectives used in fabrication: for the filter  $NA = 1.4$ , for the canal  $NA = 0.45$ . The structure can be seen in [Fig. 4.8]. The suspended channel shows superb robustness while the pore size in the filters is  $1 \mu\text{m}$  which is small enough to filter blood cells and even large biomolecules.

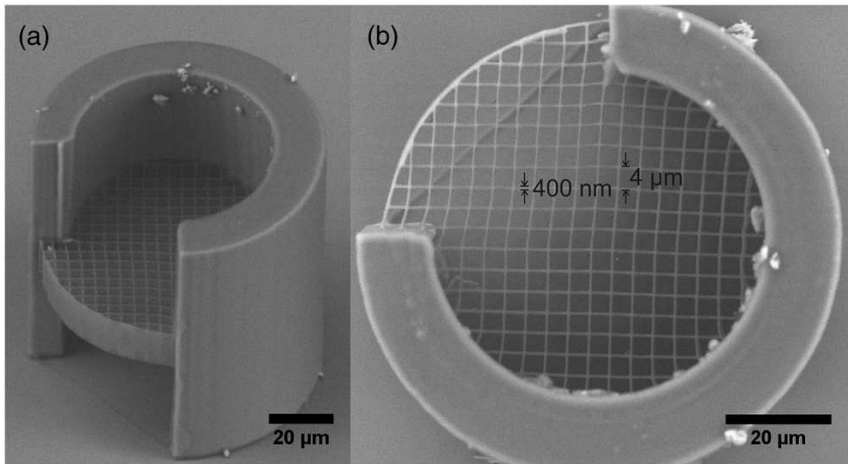


Figure 4.7: Vertical microfluidic tube with integrated filter fabricated using two objectives. (a) - side view; (b) - top view. The filter was formed first using  $NA = 1.4$  objective. The tube was manufactured after that using  $NA = 0.45$  objective. Filter period -  $4 \mu\text{m}$ , thread width -  $0.4 \mu\text{m}$ .

The required fabrication time for horizontal 3D canal using  $NA = 0.45$  objective was  $\sim 10$  minutes. If  $NA = 1.4$  is used, this time would increase to more than an hour. On the other hand, if only  $NA = 0.45$  objective is used, it would be impossible to form a high spatial resolution filter. This shows that two objective usage is a powerful tool that during fabrication of certain structures allows to highly reduce manufacturing time without sacrificing the quality of the fine details of the structure.

The results presented in this chapter give some important insights into PI-free structuring using 3DLL. If hybrid photopolymer SZ2080 is used fabrication window is comparable to the same photopolymer with IRG. At the same, due to lower photosensitivity and fewer radicals, achieving smaller features is a lot easier using pure material. It is an important discovery that is relevant for such fields as photonics as it relies on high-resolution 3DLL. Structures made out of pure SZ2080 were also shown to be strong enough

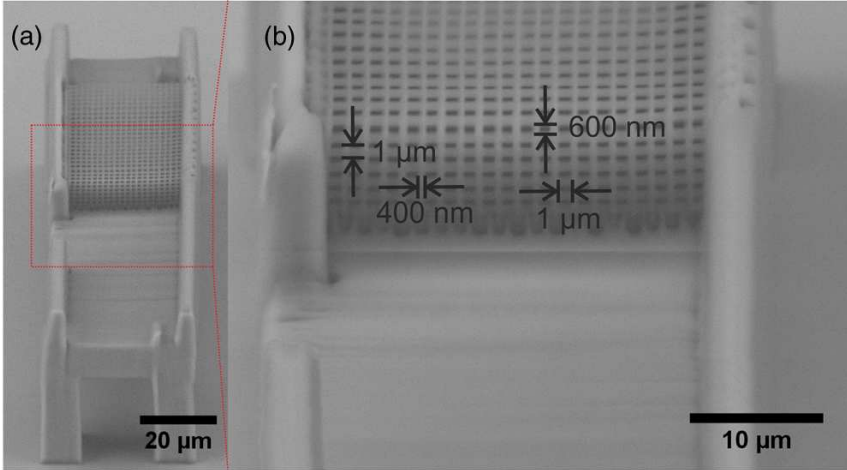


Figure 4.8: A Horizontal microfluidic canal with an integrated filter fabricated using two objectives. (a) - side view; (b) - enlarged filter view. Filter was fabricated before the canal using the  $NA = 1.4$  objective. The canal was formed using  $NA = 0.45$  objective. Filter period in horizontal direction -  $1 \mu\text{m}$ , thread width -  $0.4 \mu\text{m}$ . Period in vertical direction: -  $0.6 \mu\text{m}$ , thread height -  $1 \mu\text{m}$ .

to be made big enough for applications in such fields as biomedicine or microfluidics. Additionally, the efficiency of printing at these scales can be improved by using softer focusing  $NA = 0.45$  objectives as the reduction in  $NA$  has no adverse impact on the mechanical quality of the structure. On the other hand, if printing parameters are not well-chosen structures have a tendency to break down a lot easier than photosensitized counterparts. The reason for this was potentially revealed by AFM measurement. It turns out that after 3DLL structuring PI-free polymer consists of nanoclusters which potentially reduce the homogeneity of the material in comparison to what is achieved with photosensitized SZ2080. This also results in higher surface roughness without PI ( $RMS_{pure} = 5.5 \text{ nm}$  vs  $RMS_{IRG} = 2.4 \text{ nm}$ ) yet both values are optically acceptable  $\text{sub-}\lambda/20$  for all visible part of the spectrum. Overall, PI-free 3DLL can be viewed as advantageous in some situations like printing micro-optics with minimal absorption or bioscaffolds with minimal cytotoxicity. On the other hand, PI still yields on average higher  $R$  and potentially more mechanically robust structures. Thus, the choice of using or not using PI lies completely on what is more important - special qualities of final structure or higher  $R$  and ease of printing.

### 4.3. Conclusions

1. When processed with 515 nm, 300 fs and 200 kHz radiation SZ2080 without PI has a  $\Delta I_{IRG} - \Delta I_{pure} = 0.16 \text{ TW/cm}^2$  (15.5%) narrower fabrication window in comparison to photosensitized SZ2080 as the PI generates additional radicals at lower exposure doses.
2. Flat structures with and without PI fabricated with  $dx = 50 \text{ nm}$  (10% voxel overlay) have a sufficient surface roughness (below 10 nm RMS) and are suitable for micro-optical applications.
3. Usage of lower NA (down to 0.45) objectives has no adverse impact on PI-free structuring as long as appropriate fabrication parameters are used.

# 5. Optical Resiliency of Laser Made Structures

With questions about 3D, PI-free structuring answered LIDT investigation could commence. The main question here was how intense ( $\text{GW}/\text{cm}^2$ ) fs radiation is damaging various 3DLL made structures. It is important to note that the materials themselves were tested before [214, 38], but in the form of thin films. Refocusing, heat dissipation, and other effects potentially occurring when 3DLL made structures are exposed to laser radiation is not present during standard LIDT testing. Therefore, here we decided to test 3DLL made structures in form of microlenses, bulks, and woodpiles. Both qualitative and quantitative investigations were performed.

The results presented in this section were published in II and V papers from approbation.

## 5.1. Qualitative Investigation of Microlens Optical Resilience

The overall goal of these measurements was to determine how microlenses would operate under different irradiation conditions such as varied wavelength, exposure time, or pulse repetition rate. It is known that pure SZ2080 should have a higher optical damage threshold when tested as thin films characterized by standard LIDT [214, 38]. However, it is still unclear how this translates into the operation of standard microlenses both qualitatively and quantitatively.

First, the experiment was carried out with CW  $\lambda = 405$  nm laser operating at  $P \sim 17$  mW. Such laser was chosen as it should operate very close to the one-photon absorption regime of SZ2080. Laser beam was focused to a  $w_0 \sim 250$   $\mu\text{m}$  spot onto 50  $\mu\text{m}$  diameter microlenses, resulting in average intensity  $I_A = P/\pi w^2 \sim 8.66$   $\text{W}/\text{cm}^2$ . Intense laser radiation might induce changes both in the volume and on the surface of the micro-optical

element. For this reason, focusing properties before and after exposure to a potentially damaging light irradiation were examined using a CCD camera to determine whether microlenses were affected. Microlenses were left in 405 nm light for 30 hours, thus making it similar to extremely elongated S-to-1 testing. The light source used to measure focusing properties of microlenses in this experiment was CW HeNe laser operating at  $\lambda = 633$  nm and  $P = 3$  mW. As shown in Fig. 5.1, with CW UV laser operating at 405 nm wavelength and exposing lenses for 30 hours, no significant effects on the microlens focusing were observed. Slight changes in the shape of the focal point can be attributed to refocusing of focusing setup before and after lenses were exposed to UV laser and are insignificant enough to be discarded as measurement irregularities. Thus, low power UV CW laser radiation was shown to be relatively harmless to SZ2080 microlenses with and without PI.

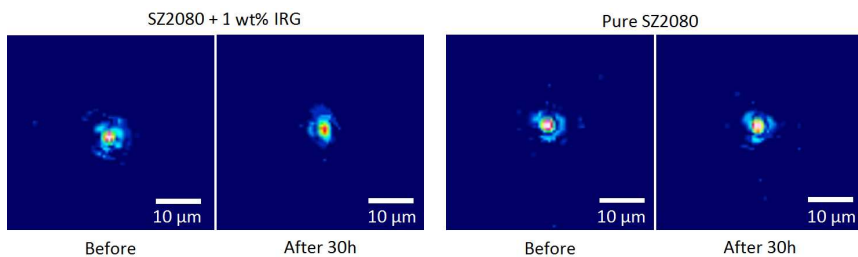


Figure 5.1: Images of microlens' focal plane before and after 30 h of exposure to 405 nm CW laser ( $P = 17$  mW). No significant change in the image at the focal point can be discerned. Slight changes in the shape of the focal point can be attributed to refocusing of the focusing setup before and after lenses were exposed to UV laser.

Next, microlenses were left for 20 hours exposed to the pulsed laser beam operating at 300 fs, 200 kHz, and 515 nm wavelength. The microfabrication setup was applied for this experiment because it offered the possibility of both controlling the fs laser beam irradiation parameters and simultaneously monitor the focusing of the microlenses *via* built-in microscope. 40x NA = 0.95 objective was employed for imaging microlenses as well as to provide focusing for 515 nm radiation. The LED was imaged through the lenses as an illumination source. The objective was off-set 85  $\mu\text{m}$  from being directly focused to the micro-optical elements, thus, allowing the laser beam to expand and to form a laser beam spot of  $\sim 250$   $\mu\text{m}$  radius and  $I_p = 0.85$   $\text{GW}/\text{cm}^2$ . Furthermore, it was deliberately offset in the transverse

direction by  $55\ \mu\text{m}$  from the center of microlenses in order to see if damage to microlenses is dependent on the  $I$  of the laser beam. Such prolonged exposure to fs laser pulses resulted in damaged microlenses that showed changes in focusing properties and overall integrity of the structure [Fig. 5.2]. This investigation of microlens focusing shows that a micro-optical element made out of pure SZ2080 was showing a less distorted image of LED and, thus, can be considered less damaged.

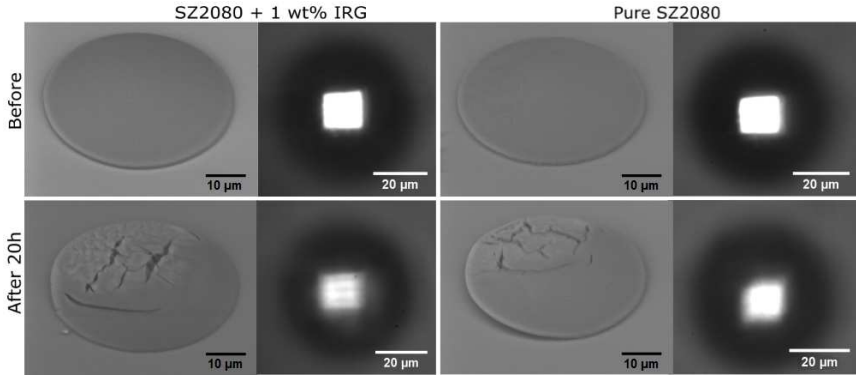


Figure 5.2: SEM images of microlenses before and after 20 h exposure to a loose focusing of 515 nm 300 fs laser radiation ( $I_p = 0.85\ \text{GW}/\text{cm}^2$ ) and image of a LED made by the lens. Degradation of lateral light distribution in the focal plane can be seen both in the structural quality of the lenses and degraded projected image. The PI containing microlenses were more degraded as the LED image in the focal plane is more distorted.

To determine whether micro-optical elements of pure SZ2080 are indeed more resilient to intense laser radiation, the following time-dependent experiment was carried out. We used 100x  $\text{NA} = 0.9$  objective to *in situ* monitor changes in the focal plane of the microlenses. As the objective was placed  $50\ \mu\text{m}$  from the microlenses,  $\sim 100\ \mu\text{m}$  radius laser beam spot was formed, with  $I_p = 1.91\ \text{GW}/\text{cm}^2$ . Such exposure resulted in fast degradation of the image [Fig. 5.3 (a)]. Two steps were discernible: when lens degradation becomes observable and when the LED image is completely obscured. In the case of lenses containing standard 1 wt% IRG, deterioration started after 20 s of irradiation and were destroyed 30 s. In the case of pure SZ2080 microlenses, the time till the beginning of deterioration was 60 s and 100 s to fully obscured LED image. As exposure dose  $E$  is proportional to the time of irradiation, microlens made out of pure SZ2080 can withstand a  $\sim 3$  times larger  $E$ . Furthermore, the damage to the mi-

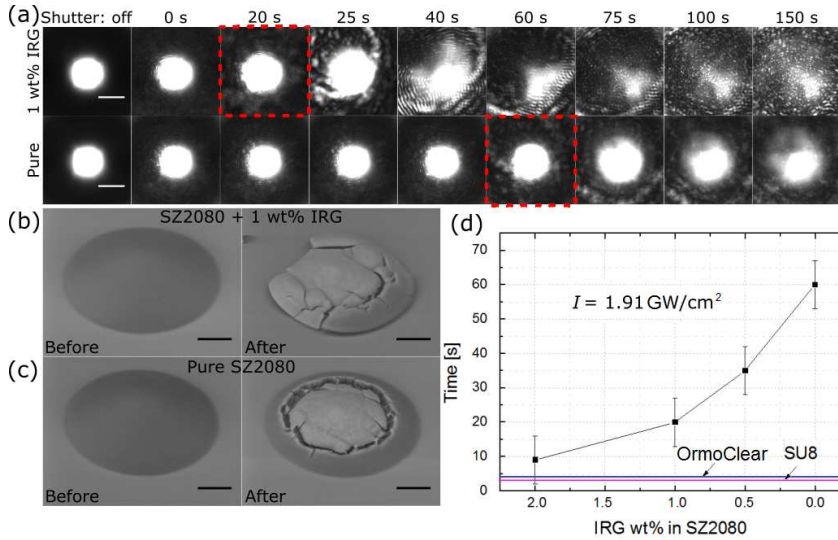


Figure 5.3: (a) Real-time monitoring of a lateral intensity distribution of LED through microlenses produced using photosensitized and pure SZ2080 during irradiation with 515 nm 300 fs pulses at 200 kHz with  $I_p = 1.91 \text{ GW/cm}^2$  (spot radius of  $100 \mu\text{m}$ ). Faster deterioration of SZ2080 containing 1 wt% IRG as compared with pure SZ2080 is evident, as an image at the focus starts to degrade after 60 and 20 s (marked by red dashed squares), respectively. (b) and (c) SEM micrographs of the tested lenses before and after exposure. The photosensitized element is destroyed, while the one produced out of pure SZ2080 exhibits relatively low damage. (d) Start of the microlens degradation for different concentrations of PI in SZ2080, as well as the time needed to damage SU8 and OrmoClear. All scale bars are  $10 \mu\text{m}$ .

microlenses differed. Entire microlens was structurally damaged in the case of SZ2080 with 1 wt% IRG [Fig. 5.3 (b)] resembling a thermomechanical failure, while pure SZ2080 lenses were damaged only in the central region by a homogeneous melting [Fig. 5.3 (c)]. Experiments were repeated several times and showed that the result deviated no more than 7 s from one experiment to another, which is in the range of tens-of-percent from the measured values. For better comparison, more tests were performed varying IRG concentrations (0.5 wt% and 2 wt%) and standard lithographic material SU8 [Fig. 5.3 (d)]. Results proved that increase in PI concentration leads to the lesser time needed before fs laser light damages the microlens, namely 9 s with 2 wt% IRG. Non-hybrid SU8 started to deteriorate just  $\sim 3$  s after

the shutter was opened with no noticeable deviations in time between the experiments. This shows that even with relatively high (2 wt%) IRG concentrations SZ2080 can withstand intense laser radiation at least 3 times better than SU8. Removal of PI increases this superiority to more than one order ( $\sim 20$  times), which agrees well with earlier findings in thin films [214]. Thus, in the case of intense continuous exposure, hybrid material without PI is the best for microlens fabrication in terms of optical resiliency.

Presented analysis show degradation of microlenses during exposure. However, the question remained if this is tied more to the  $I_p$  or accumulated dose. Thus, the next set of lenses was continuously exposed for 15 min  $I_p = 1.27 \text{ GW/cm}^2$  radiation while the other set was irradiated for a combined 15 min exposure delivered in 10 s light bursts followed by 10 s pauses (30 min total). This resulted in microlenses being severely damaged for both pure and photosensitized SZ2080 when exposed in a continuous manner [Fig. 5.4 (a)]. However, the multi-burst exposure of non-photosensitized microlenses showed no noticeable distortions, while the photosensitized lenses were degraded [Fig. 5.4 (b)]. To further explore this effect lenses were exposed to 5 min of continuous  $1.91 \text{ GW/cm}^2$  radiation with pulse repetition rates of 10, 100, and 200 kHz [Fig. 5.4 (b)]. With 10 kHz illumination, both pure and photosensitized SZ2080 samples showed no noticeable changes in lateral light distribution at the focal plane, while both types of microlenses were completely destroyed by 200 kHz radiation. For this reason, repetition rates below or over these values were not tested. The response to 100 kHz varied between non-photosensitized and IRG containing SZ2080 microlenses. The effect on the pure SZ2080 microlens was minimal while the IRG containing one displayed appreciable distortions. All these results clearly demonstrate that the most probable cause of damage is the heat accumulated in the volume of the lens and not the  $I_p$ . Better mitigation of heat load could solve thermal degradation of micro-optical elements.

## 5.2. Quantitative Investigation of LIDT for Laser Made 3D Structures

The results shown so far are more-less qualitative because they do not provide the exact value of LIDT of produced structures. However, this is extremely important if 3DLL made objects were to be used in fields where  $I > \text{GW/cm}^2$ . These include but are not limited to communications or fiber laser. Thus, a more quantitative investigation is needed.



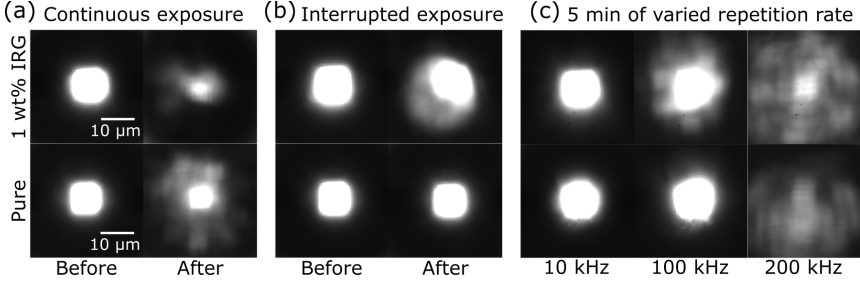


Figure 5.4: Focusing performance of microlenses after exposure to  $I_p = 1.27 \text{ GW/cm}^2$  515 nm 300 fs radiation in continuous (a) and multi-burst mode: 10 s exposure followed by a 10 s pause (b). (c) Lateral distribution at the focus of microlenses exposed to 5 min of continuous radiation at  $I_p = 1.91 \text{ GW/cm}^2$  achieved with repetition rates of 10, 100, and 200 kHz. 10 kHz case also serves as before image as there were no changes in focusing properties after such experiment.

We began by fabricating a 10x10 array of identical bulk structures with a size of  $100 \mu\text{m} \times 100 \mu\text{m} \times 30 \mu\text{m}$ . They were spaced apart by  $150 \mu\text{m}$ . An SEM image of a manufactured array of SZ2080 is shown in Fig. 5.5. All structures are identical. This is an important prerequisite - while testing somewhat minimized random errors *via* statistical nature, high repeatability of made structures also helped in that regard.

To reflect different types of materials used in 3DLL, various popular photopolymers were investigated. Thus, it should be sufficient to show general tendencies in terms of 3DLL processable material LIDT. Namely, the materials were a resin used in typical stereolithographic processes (PR48 from Autodesk), the popular epoxy-based resin SU8, and two hybrid organic-inorganic resins (OrmoClear and SZ2080) [181]. SZ2080 was used with either of the two following photoinitiators, 4,4'-bis(dimethylamino)benzophenone (BIS) or IRG. Furthermore, SZ2080 was used as is without a photoinitiator. In the following, these photoinitiators will be referred to by using abbreviations BIS and IRG, respectively. Experimental results of LIDT tests are shown in Fig. 5.6. The highly photoactive PR48 has the lowest LIDT value of  $F_t = 4 \pm 3 \text{ mJ/cm}^2$ . The second-lowest LIDT value belongs to SZ2080 with 1% wt BIS:  $F_t = 17 \pm 9 \text{ mJ/cm}^2$ . This result can partly be explained by the relatively long wavelength absorption of BIS that reaches into the visible part of the spectrum ( $\sim 520 \text{ nm}$  [260]). The LIDT value for SU8 is  $F_t = 36 \pm 6 \text{ mJ/cm}^2$  (absorption peak - 360 nm). SZ2080 with 1% wt. IRG and OrmoClear followed with

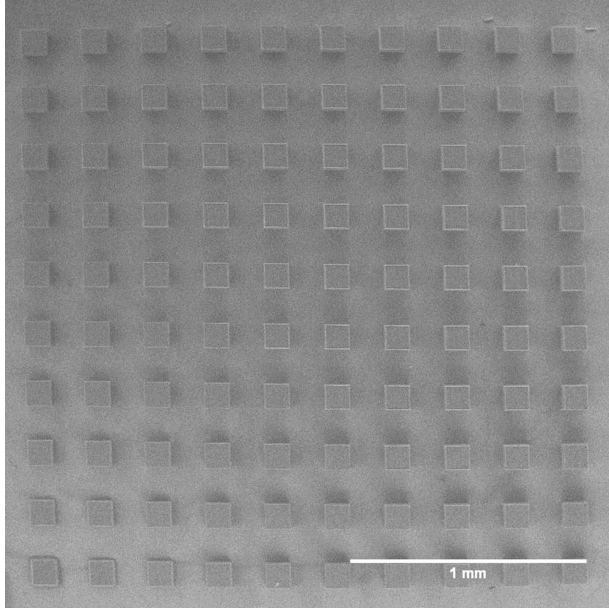


Figure 5.5: 10x10 3DLL produced bulk structure array before it was subjected to LIDT measurement.

$F_t = 42 \pm 15 \text{ mJ/cm}^2$  and  $F_t = 51 \pm 15 \text{ mJ/cm}^2$ , respectively. This can be expected as both of these materials are glassy hybrids with absorption in the UV ( $\sim 390 \text{ nm}$  [214, 260] and  $\sim 375 \text{ nm}$  [261] respectively). Finally, SZ2080 with no photoinitiator outperformed all other materials with a LIDT value of  $F_t = 169 \pm 15 \text{ mJ/cm}^2$ . The absorption spectrum of non-photosensitized SZ2080 starts as low as  $340 \text{ nm}$  [214, 260]). In all of these cases, absorption was measured in materials as if they were prepared for fabrication. With  $F_t$  plotted as a function of absorption, we can see a clear correlation. This can be tied with a lower order of nonlinearity for tested  $1030 \text{ nm}$  radiation as absorption peak moves to longer wavelengths. Furthermore, for all tested materials the tendency of hybrids to be more resilient than organic polymers at the same optical absorption values is also visible.

Besides absorption, another material characteristic that can influence damage mechanisms is its homogeneity. The linear regression shown in Fig. 5.6 is an indication of how homogeneous a fabricated microstructure is. All three worst-performing materials have damage dynamic ranges (i.e.  $E$  values when  $p = 0\%$  to  $p = 100\%$ ) that are relatively narrow (less than  $50 \text{ mJ/cm}^2$ ). On the contrary, SZ2080 with 1% wt. IRG and Or-

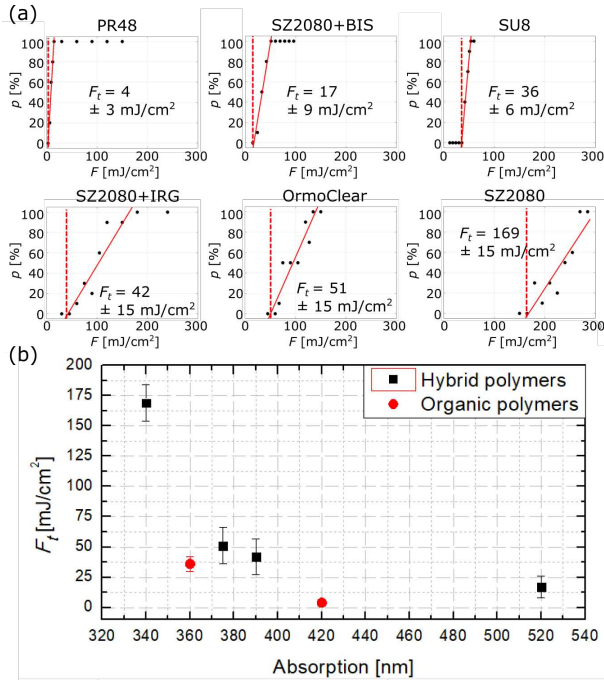


Figure 5.6: (a) LIDT values of bulks for all tested materials. Solid red lines represent linear approximation, red dashed lines - the threshold  $F$ . SZ2080 with no PI is the most resilient with  $F_t = 161.9 \pm 12.5$  mJ/cm<sup>2</sup>. (b)  $F_t$  depends on the absorption of the material. Hybrid polymers are also more resilient at the same absorption than pure organics for all tested materials.

moClear have damage dynamic ranges that cover 100 mJ/cm<sup>2</sup>. Therefore, the somewhat inhomogeneous (in terms of LIDT) nature of the material at the nano-scale can be considered. In such a case, different nano-constitutes/impurities of the material have varying LIDT [219]. The beginning of dynamic damage range starts when constitute having lower LIDT starts being damaged and reaches full 100% when even the more resilient part is being fully affected every time. In this case, the source of such inhomogeneity might be the photoinitiators and the composition of SZ2080 itself forming small conglomerates of lower  $F_t$  that reduce the overall LIDT value.

Some interesting aspects concerning damage dynamics and topography were also revealed. First, it was noted that some damage types can only be seen with a specific microscope (SEM *vs* Optical) [Fig. 5.7]. This was

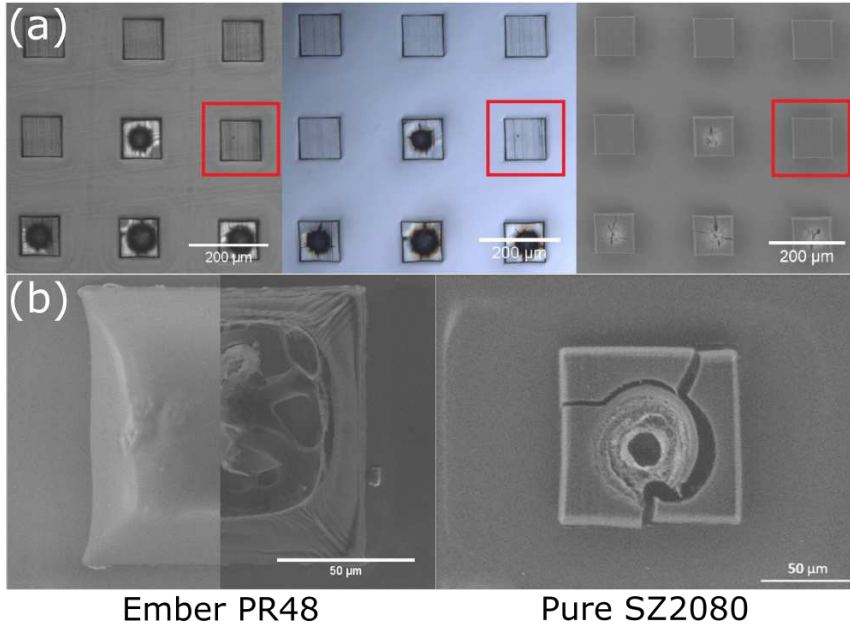


Figure 5.7: (a) - same damaged bulk objects are imaged with interference, optical, and SEM images. In the first two, the damage is visible, while in the SEM image - not. This highlighted the necessity to check samples after laser exposure with all the available imaging means as some damage types were not visible with one or another microscope. (b) - different damage topographies of purely organic Ember PR48 and hybrid organic-inorganic SZ2080. Organic material showed a tendency to burn, while hybrid to melt and crack.

the reason why it was decided to use both types of imaging. Furthermore, damage topography showed severe differences between organic and hybrid materials. Organic materials tended to burn, while hybrids - burn and shatter. This indicates that the damage mechanisms are to some extent different. It is further reinforced by the highly varying slope of each linear approximation. While organics showed relatively steep  $p$  distributions, hybrids exhibited more dispersed distribution over a higher range of  $F$ , meaning that hybrid materials are potentially less homogeneous on the nano-level.

Next, we evaluated woodpiles made out of SZ2080 and SZ2028+1% IRG. For easy fabrication and reproducibility, geometry parameters were  $az = 1.13 \mu\text{m}$ ,  $axy = 0.8 \mu\text{m}$ ,  $dxy = 0.35 \mu\text{m}$ . LIDT evaluations showed

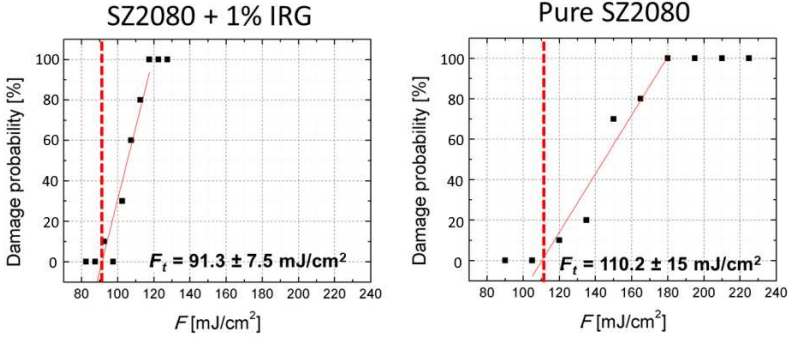


Figure 5.8: The LIDT measurement results of woodpiles made out of SZ2080 + 1% IRG and pure SZ2080. The  $F_t$  needed to damage such structures are  $91.3 \pm 7.5 \text{ mJ}/\text{cm}^2$  and  $110.2 \pm 15 \text{ mJ}/\text{cm}^2$  respectively showing the superiority of non-photosensitized material.

that pure material was better at sustaining high  $F$  with the threshold being  $F_t = 110.2 \pm 15 \text{ mJ}/\text{cm}^2$  [Fig. 5.8]. In comparison, photosensitized material had  $F_t = 91.3 \pm 7.5 \text{ mJ}/\text{cm}^2$ . Thus, while the general tendency of pure material being more resilient than photosensitized prevailed in the case of woodpiles, which is in accordance with previous findings, the discrepancy was not as large as in the case of bulks. Thus, an interplay between smaller absorbing volume and better heat dissipation can be considered to occur in the case of woodpiles. This is further proven by the substantial differences in the damage topography [Fig. 5.9]. If the fluence is just above the  $F_t$ , only the slight burning on the top of the woodpile appears. When laser power is increased the localized hole forms. Finally, a complete deformation of the structure happens if the laser intensity is several times higher than  $F_t$ .

The 3DLL made woodpile structures were shown to be possible candidates for a huge variety of photonic applications. While this is one of the main motivations behind testing LIDT of 3DLL made woodpiles, the photonic properties can potentially distort the measurement results. This is due to the fact that polymeric woodpiles can have very well pronounced photonic properties. Thus, if the tested wavelength coincides with a photonic bandgap, the LIDT might change unpredictably.

To clarify if this is not the case in this study, numerical modeling based on Finite-difference time-domain (FDTD) was performed. A woodpile configuration that could be fabricated using 3DLL was chosen. The constants

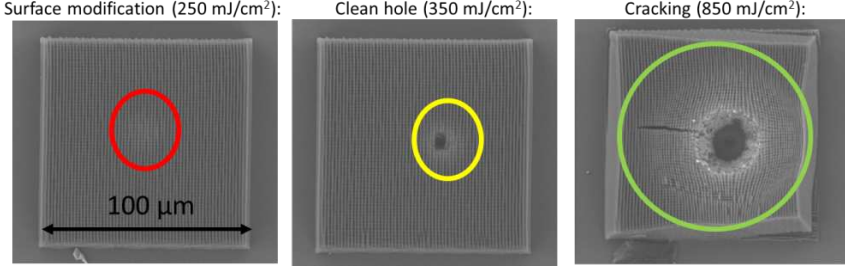


Figure 5.9: The laser-induced damage topographies in pure material with different  $F$ . Relatively localized damage is evident unless very high  $F$  is used.

were chosen to be  $axy = 800$  nm and  $az = 1130$  nm. The  $dxy$  was varied from 300 to 400 nm by 50 nm. Results show that while reflection and transmission properties change substantially from one case to another, in none of the investigated cases the shift between these two properties coincides with tested wavelength [Fig. 5.10 (a)]. When such woodpiles were produced out of non-photosensitized material their  $F_t$  did not vary a lot, increasing from  $99.4 \pm 15$  mJ/cm<sup>2</sup> at  $dxy = 300$  nm to  $116 \pm 15$  mJ/cm<sup>2</sup> at  $dxy = 400$  nm. This can be considered either a result of the statistical nature of the presented method or the porosity of the structure. Regardless, it is obvious that in the chosen experimental setup, reflection properties do not have a huge impact on the LIDT.

Next, surface area  $S$  and internal volume  $V$  of polymerized lines were calculated assuming lines to be ellipsoids [168]. It is known that surface defects are one of the primary reasons for optical damage [262]. Thus, the goal here was to check if relatively high  $S$  and small  $V$  would lead to lower LIDT. The calculation was done assuming the lines in woodpile to have an elliptical profile and calculating the internal volume and surface area of such rod. Having  $V$  allows to calculate fill factor ( $FF$ ), showing how much of volume is taken up by lines in comparison to full same sized bulk. Indeed, with a lot of volume in the structure taken up by air, the thermal diffusion should be minimized. Thus, if LIDT would depend on  $FF$  it would point out the strong thermal nature of the effect. LIDT values of woodpiles depend on changes in  $S/V$  and  $FF$  are shown in Fig. 5.11 (a). No clear dependency can be deduced, thus showing minimal LIDT dependence on woodpiles  $FF$  and  $S/V$  ratio with maximal LIDT value  $F_t = 139.5 \pm 15$  mJ/cm<sup>2</sup> at  $axy = 400$  nm.

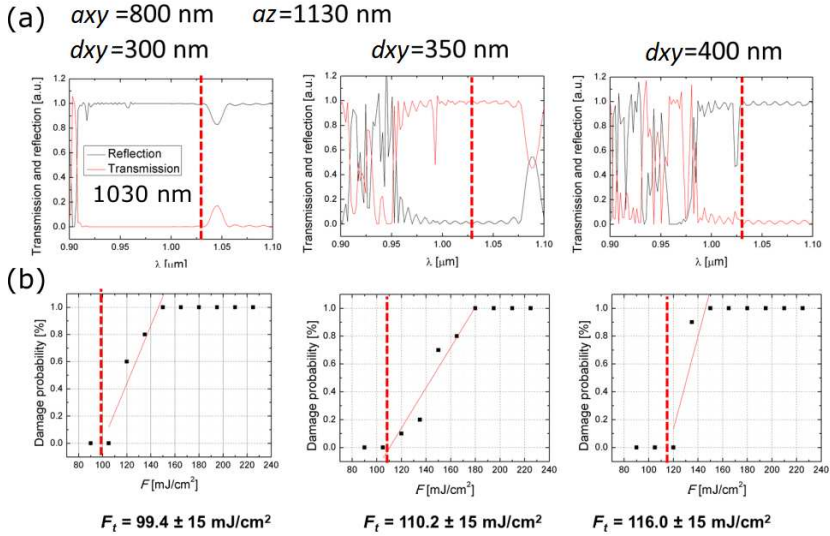


Figure 5.10: (a) - numerically derived transmission of reflection spectra for normal incidence of woodpiles with varied  $dxy$  ( $axy = 800$  nm,  $az = 1130$  nm). The wavelength used to induce damage (1030 nm, red dashed line) does not coincide with any photonic bandgaps. (b) - LIDT measurements of corresponding woodpiles. While LIDT shows a tendency to increase with  $dxy$ , the change is in the order of measurement error.

Due to the woodpile geometry, the strength of the electrical field  $E$  inside of such structure can have some nontrivial peaks. Mathematical modeling was performed in order to visualize it. Standard FDTD modeling procedure described in the literature was used [263]. Due to peculiarities of the mathematical model used only  $dxy = 500$  nm, 450 nm and 400 nm could be calculated. The modeling shows that changes in  $dxy$  can increase  $E^2$  value by  $\sim 23$  times comparing the lowest and the highest value [Fig. 5.11 (b)] at  $dxy = 400$  nm and  $dxy = 500$  nm respectively. These peaks are located inside of the woodpile lines, which denotes possible influence on LIDT. Geometries with such a significant increase in  $E^2$  also proved to have  $\sim 27.3\%$  lower LIDT. It is important to note that such a huge discrepancy between the estimated difference in  $E$  values and measured LIDT is the result of the approximate nature of FDTD modeling. Thus, while it is acceptable at showing the general principle of  $E$  confinement in the woodpile, it does not directly proportional to LIDT. Nevertheless, the relation between wood-

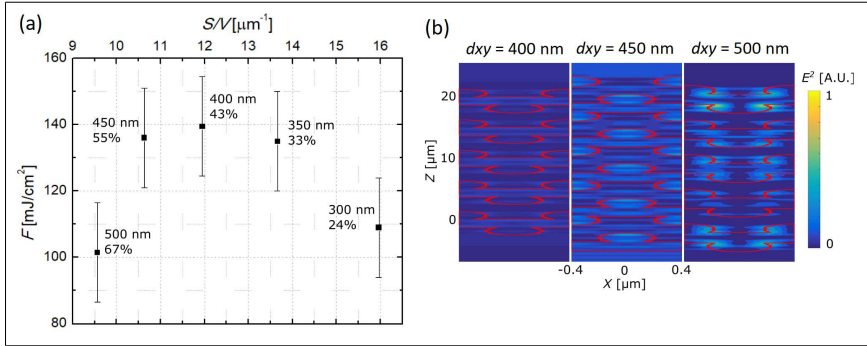


Figure 5.11: (a) LIDT dependency on  $S/V$  ratio and  $FF$  (written near each measured point alongside  $dxy$  value). No clear tendency can be seen. (b) - result of  $E^2$  modeling inside of woodpiles with the three thickest  $dxy$  values. Regions enclosed by the red line show the cut of internal features of the woodpile. Difference between the highest (at  $dxy = 500$  nm) and lowest (at  $dxy = 400$  nm)  $E^2$  is  $\sim 23$  times. This follows the tendency of increase in LIDT between these two cases by  $\sim 27.3\%$  showing that optical resiliency depends on photonic properties of the woodpile.

pile's photonic properties and its LIDT is evident. Care should be taken when using 3D woodpile type structures in high light intensities even if they should be transparent to usable wavelength, as internal distribution of  $E^2$  might yield some specific peaks that could consequently damage the structure.

The woodpile testing protocol was repeated with photosensitized woodpiles. The highest acquired LIDT was  $F_t = 105 \pm 7.5$   $\text{mJ}/\text{cm}^2$ . As expected, it was lower than LIDT of the most resilient non-photosensitized SZ2080 woodpile by  $\sim 24.8\%$ . On the other hand, it exceeded the value acquired with the same photopolymer composition in a bulk configuration. This shows that smaller  $V$  of absorbing woodpile outweighs potential phonic  $E^2$  confinement. Nevertheless, this was not noticed in a less absorbing pure material. At the same time, the LIDT difference is a lot smaller between woodpiles than between bulk objects ( $\sim 77.4\%$  difference) meaning that geometry is more important than material absorption in the case of woodpiles.

Overall the performed LIDT measurements point to the superiority of pure SZ2080. It is true for both bulk and woodpile structures [Fig. 5.12]. This can be attributed to the hybrid organic-inorganic nature of the material combined with minimal optical absorption in comparison to other tested



polymers. Paired with sufficient structurality with 3DLL this makes non-photosensitized SZ2080 an adequate candidate for relatively high optical resistance micro-optics.

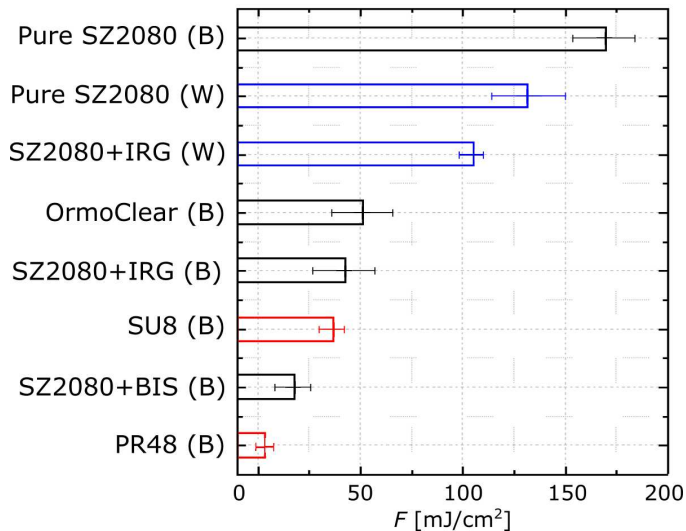


Figure 5.12: Direct comparison of LIDT between all the tested materials and geometries. Bulk is denoted by letter B and woodpiles by W (these values are also blue). The clear superiority of hybrid polymers (black values) over organic ones (red values) is evident for all the tested materials if the absorption of the materials is kept comparable. The best performing are woodpile and bulk structures made out of pure SZ2080 with the latter being the most resilient.

On the other hand, OrmoClear had a threshold that is only about 3 times lower which is comparable to pure SZ2080. Additionally, OrmoClear is liquid during structuring, meaning that it can be used in dip-in fashion [202], popular in fabricating some types of microoptics [100]. Therefore, even if a dip-in fabrication technique must be applied, suitable material exhibits LIDT higher than organic counterparts.

### 5.3. Conclusions

1. 3DLL made micro-lenses were shown to degrade less when exposed to either lower repetition rate (down to 1 kHz from 200 kHz) or to interrupted exposure (10 s of exposure followed by 10 s with closed

laser shutter) while maintaining the same  $I$  or  $E$  respectively, pointing out to thermo-accumulative nature of the induced damage during S-to-1 testing.

2. LIDT in 3DLL made structures depends on the optical absorption, composition (organic vs hybrid) of the material, and geometry (bulk vs woodpile) of the structure, with pure 3DLL made SZ2080 structures being the most resistant from all the tested ones at  $F_t=161.9$  mJ/cm<sup>2</sup>, which is around one order of magnitude lower than fused silica.
3. Due to the interplay between photonic effects and optical absorption, 3DLL made nano-woodpile geometry reduces LIDT of the pure SZ2080 structure by 31.25% in comparison to bulk object.

# Bibliography

- [1] H. Lasi, P. Fettke, T. Feld, H. M., *Industry 4.0, BISE* **6**(4), 239–242 (2014).
- [2] J.-M. Lehn, Toward self-organization and complex matter, *Science* **295**(5564), 2400–2403 (2002).
- [3] L. Wang, Q. Li, Stimuli-directing self-organized 3D liquid-crystalline nanostructures: From materials design to photonic applications, *Adv. Funct. Mater.* **26**(1), 10–28 (2015).
- [4] J. W. Stansbury, M. J. Idacavage, 3D printing with polymers: Challenges among expanding options and opportunities, *Dent. Mater.* **32**(1), 54–64 (2016).
- [5] L. Jonušauskas, S. Juodkazis, M. Malinauskas, Optical 3D printing: bridging the gaps in the mesoscale, *J. Opt.* **20**(5), 053001 (2018).
- [6] T. H. Maiman, Stimulated optical radiation in ruby, *Nature* **187**(4736), 493–494 (1960).
- [7] P. A. Franken, A. E. Hill, C. W. Peters, G. Weinreich, Generation of optical harmonics, *Phys. Rev. Lett.* **7**(4), 118–119 (1961).
- [8] B. N. Chichkov, C. Momma, S. Nolte, F. Alvensleben, A. Tünnermann, Femtosecond, picosecond and nanosecond laser ablation of solids, *Appl. Phys. A* **63**(2), 109–115 (1996).
- [9] D. Sola, J. Peña, Study of the wavelength dependence in laser ablation of advanced ceramics and glass-ceramic materials in the nanosecond range, *Materials* **6**(11), 5302–5313 (2013).
- [10] U. Keller, K. Weingarten, F. Kartner, D. Kopf, B. Braun, I. Jung, R. Fluck, C. Honninger, N. Matuschek, J. A. der Au, Semiconductor saturable absorber mirrors (SESAM's) for femtosecond to nanosecond pulse generation in solid-state lasers, *IEEE J. Sel. Top. Quantum Electron.* **2**(3), 435–453 (1996).
- [11] K.-H. Leitz, B. Redlingshöfer, Y. Reg, A. Otto, M. Schmidt, Metal ablation with short and ultrashort laser pulses, *Phys. Procedia* **12**, 230–238 (2011).

- [12] S. Maruo, O. Nakamura, S. Kawata, Three-dimensional microfabrication with two-photon-absorbed photopolymerization, *Opt. Lett.* **22**(2), 132–134 (1997).
- [13] J. Qu, M. Kadic, A. Naber, M. Wegener, Micro-structured two-component 3D metamaterials with negative thermal-expansion coefficient from positive constituents, *Sci. Rep.* **7**, 40643 (2017).
- [14] M. Power, A. J. Thompson, S. Anastasova, G.-Z. Yang, A monolithic force-sensitive 3D microgripper fabricated on the tip of an optical fiber using 2-photon polymerization, *Small* **14**(16), 1703964 (2018).
- [15] J. Mačiulaitis, M. Deveikytė, S. Rekštytė, M. Bratchikov, A. Darinskas, A. Šimbelytė, G. Daunoras, A. Laurinavičienė, A. Laurinavičius, R. Gudas, M. Malinauskas, R. Mačiulaitis, Preclinical study of SZ2080 material 3D microstructured scaffolds for cartilage tissue engineering made by femtosecond direct laser writing lithography, *Biofabrication* **7**(1), 015015 (2015).
- [16] B. Richter, V. Hahn, S. Bertels, T. K. Claus, M. Wegener, G. Delaittre, C. Barner-Kowollik, M. Bastmeyer, Guiding cell attachment in 3D microscaffolds selectively functionalized with two distinct adhesion proteins, *Adv. Mater.* **29**(5) (2017).
- [17] D. Wu, S.-Z. Wu, J. Xu, L.-G. Niu, K. Midorikawa, K. Sugiyoka, Hybrid femtosecond laser microfabrication to achieve true 3D glass/polymer composite biochips with multiscale features and high performance: the concept of ship-in-a-bottle biochip, *Laser Photonics Rev.* **8**(3), 458–467 (2014).
- [18] L. Jonušauskas, S. Rekštytė, R. Buividas, S. Butkus, R. Gadonas, S. Juodkakis, M. Malinauskas, Hybrid subtractive-additive-welding microfabrication for lab-on-chip (LOC) applications via single amplified femtosecond laser source, *Opt. Eng.* **56**(9), 094108 (2017).
- [19] C. Liberale, G. Cojoc, F. Bragheri, P. Minzioni, G. Perozziello, R. La Rocca, L. Ferrara, V. Rajamanickam, E. Di Fabrizio, I. Cristiani, Integrated microfluidic device for single-cell trapping and spectroscopy, *Sci. Rep.* **3**, 1258 (2013).
- [20] T. Gissibl, S. Thiele, A. Herkommer, H. Giessen, Two-photon direct laser writing of ultracompact multi-lens objectives, *Nat. Photonics* **10**(8), 554–560 (2016).
- [21] L. Maigyte, V. Purlys, J. Trull, M. Peckus, C. Cojocar, D. Gailevičius, M. Malinauskas, K. Staliunas, Flat lensing in the visible frequency range by woodpile photonic crystals, *Opt. Lett.* **38**(14), 2376–2378 (2013).

- [22] A. I. Aristov, M. Manousidaki, A. Danilov, K. Terzaki, C. Fotakis, M. Farsari, A. V. Kabashin, 3D plasmonic crystal metamaterials for ultra-sensitive biosensing, *Sci. Rep.* **6**(1), 25380 (2016).
- [23] C. W. Ha, P. Prabhakaran, K.-S. Lee, Versatile applications of three-dimensional objects fabricated by two-photon-initiated polymerization, *MRS Communications* 1–14 (2018).
- [24] M. Farsari, M. Vamvakaki, B. N. Chichkov, Multiphoton polymerization of hybrid materials, *J. Opt.* **12**, 124001 (2010).
- [25] C. Barner-Kowollik, M. Bastmeyer, E. Blasco, G. Delaittre, P. Muller, B. Richter, M. Wegener, 3D laser micro- and nanoprinting: Challenges for chemistry, *Angew. Chem. Int. Ed.* **56**(50), 15828–15845 (2017).
- [26] S. Lightman, R. Gvishi, G. Hurvitz, A. Arie, Shaping of light beams by 3D direct laser writing on facets of nonlinear crystals, *Opt. Lett.* **40**(19), 4460–4463 (2015).
- [27] R. Suriano, T. Zandrini, C. de Marco, R. Osellame, S. Turri, F. Bragheri, Nanomechanical probing of soft matter through hydrophobic AFM tips fabricated by two-photon polymerization, *Nanotechnology* **27**(15), 155702 (2016).
- [28] L. Yang, A. El-Tamer, U. Hinze, J. Li, Y. Hu, W. Huang, J. Chu, B. N. Chichkov, Parallel direct laser writing of micro-optical and photonic structures using spatial light modulator, *Opt. Lasers Eng.* **70**, 26–32 (2015).
- [29] J. S. Oakdale, R. F. Smith, J.-B. Forien, W. L. Smith, S. J. Ali, L. B. Bayu Aji, T. M. Willey, J. Ye, A. W. van Buuren, M. A. Worthington, S. T. Prisbrey, H. S. Park, P. A. Amendt, T. F. Baumann, J. Biener, Direct laser writing of low-density interdigitated foams for plasma drive shaping, *Adv. Funct. Mater.* **27**(43), 1702425 (2017).
- [30] S. Dehaeck, B. Scheid, P. Lambert, Adaptive stitching for meso-scale printing with two-photon lithography, *Additive Manufacturing* **21**, 589–597 (2018).
- [31] L. J. Jiang, J. H. Campbell, Y. F. Lu, T. Bernat, N. Petta, Direct writing target structures by two-photon polymerization, *Fusion Sci. Technol.* **70**(2), 295–309 (2016).
- [32] A. Accardo, M.-C. Blatché, R. Courson, I. Loubinoux, C. Thibault, L. Malaquin, C. Vieu, Multiphoton direct laser writing and 3D imaging of polymeric freestanding architectures for cell colonization, *Small* **13**(27), 1700621 (2017).

- [33] H. Ni, G. Yuan, L. Sun, N. Chang, D. Zhang, R. Chen, L. Jiang, H. Chen, Z. Gu, X. Zhao, Large-scale high-numerical-aperture super-oscillatory lens fabricated by direct laser writing lithography, *RSC Advances* **8**(36), 20117–20123 (2018).
- [34] L. Jonušauskas, D. Gailevičius, L. Mikoliūnaitė, D. Sakalauskas, S. Šakirzanovas, S. Juodkazis, M. Malinauskas, Optically clear and resilient free-form  $\mu$ -optics 3D-printed via ultrafast laser lithography, *Materials* **10**(1), 12 (2017).
- [35] P. Danilevičius, S. Rekštytė, E. Balčiūnas, A. Karaniauskas, R. Širmenis, D. Baltriukienė, M. Malinauskas, V. Bukelskienė, R. Gadonas, V. Sirvydis, A. Piskarskas, Direct laser fabrication of polymeric implants for cardiovascular surgery, *Mater. Sci.* **18**(2), 145–149 (2012).
- [36] P. Danilevičius, S. Rekštytė, E. Balčiūnas, A. Kraniauskas, R. Širmenis, D. Baltriukienė, V. Bukelskienė, R. Gadonas, V. Sirvydis, A. Piskarskas, M. Malinauskas, Laser 3D micro/nanofabrication of polymers for tissue engineering applications, *Opt. Laser Technol.* **45**, 518–524 (2013).
- [37] C. Rensch, S. Hell, M. Schickfus, S. Hunklinger, Laser scanner for direct writing lithography, *Appl. Opt.* **28**(17), 3754–3758 (1989).
- [38] A. Žukauskas, G. Batavičūtė, M. Ščiuka, Z. Balevičius, A. Melninkaitis, M. Malinauskas, Effect of the photoinitiator presence and exposure conditions on laser-induced damage threshold of ORMOSIL (sz2080), *Opt. Mater.* **39**, 224–231 (2015).
- [39] O. Abdulhameed, A. Al-Ahmari, W. Ameen, S. H. Mian, Additive manufacturing: Challenges, trends, and applications, *Adv. in Mech. Eng.* **11**(2), 1–27 (2019).
- [40] H. Paris, H. Mokhtarian, E. Coatanéa, M. Museau, I. F. Ituarte, Comparative environmental impacts of additive and subtractive manufacturing technologies, *CIRP Ann. Manuf. Technol.* **65**(1), 29–32 (2016).
- [41] A. Lasemi, D. Xue, P. Gu, Recent development in CNC machining of freeform surfaces: A state-of-the-art review, *Comput. Aided Des.* **42**(7), 641–654 (2010).
- [42] A. K. Dubey, V. Yadava, Laser beam machining—a review, *Int. J. Mach. Tools Manuf.* **48**(6), 609–628 (2008).
- [43] A. N. Samant, N. B. Dahotre, Laser machining of structural ceramics—a review, *J. Eur. Ceram. Soc.* **29**(6), 969–993 (2009).

- [44] S. Butkus, E. Gaižauskas, D. Paipulas, Ž. Viburyš, D. Kaškelyė, M. Barkauskas, A. Alesnikov, V. Sirutkaitis, Rapid microfabrication of transparent materials using filamented femtosecond laser pulses, *Appl. Phys. A* **114**(1), 81–90 (2013).
- [45] C. Hnatovsky, R. S. Taylor, E. Simova, V. R. Bhardwaj, D. M. Rayner, P. B. Corkum, Polarization-selective etching in femtosecond laser-assisted microfluidic channel fabrication in fused silica, *Opt. Lett.* **30**(14), 1867–1869 (2005).
- [46] D. Wortmann, J. Gottmann, N. Brandt, H. Horn-Solle, Micro- and nanostructures inside sapphire by fs-laser irradiation and selective etching, *Opt. Express* **16**(3), 1517–1522 (2008).
- [47] M. Hermans, J. Gottmann, F. Riedel, Selective, laser-induced etching of fused silica at high scan-speeds using KOH, *J. Laser Micro Nanoeng.* **9**(2), 126–131 (2014).
- [48] J. R. Tumbleston, D. Shirvanyants, N. Ermoshkin, R. Januszewicz, A. R. Johnson, D. Kelly, K. Chen, R. Pinschmidt, J. P. Rolland, A. Ermoshkin, E. T. Samulski, J. M. DeSimone, Continuous liquid interface production of 3D objects, *Science* **347**(6228), 1349–1352 (2015).
- [49] M. Wang, H. Zhang, Q. Hu, D. Liu, H. Lammer, Research and implementation of a non-supporting 3D printing method based on 5-axis dynamic slice algorithm, *Robot. Cim-Int Manuf.* **57**, 496–505 (2019).
- [50] M. O. Wang, C. E. Vorwald, M. L. Dreher, E. J. Mott, M.-H. Cheng, A. Cinar, H. Mehdizadeh, S. Somo, D. Dean, E. M. Brey, J. P. Fisher, Evaluating 3D-printed biomaterials as scaffolds for vascularized bone tissue engineering, *Adv. Mater.* **27**(1), 138–144 (2014).
- [51] M. Malinauskas, S. Rekštytė, L. Lukoševičius, S. Butkus, E. Balčiūnas, M. Pečiukaiytė, D. Baltriukienė, V. Bukelskienė, A. Butkevičius, P. Kucevičius, V. Rutkūnas, S. Juodkakis, 3D microporous scaffolds manufactured via combination of fused filament fabrication and direct laser writing ablation, *Micromachines* **5**(4), 839–858 (2014).
- [52] T. Campbell, C. Williams, O. Ivanova, B. Garrett, Could 3D printing change the world, *Technologies, Potential, and Implications of Additive Manufacturing* (2011).
- [53] H. Windsheimer, N. Travitzky, A. Hofenauer, P. Greil, Laminated object manufacturing of preceramic-paper-derived Si<sup>+</sup> SiC composites, *Adv. Mater.* **19**(24), 4515–4519 (2007).

- [54] J. Lipton, D. Arnold, F. Nigl, N. Lopez, D. L. Cohen, N. Norén, H. Lipson, Multi-material food printing with complex internal structure suitable for conventional post-processing, in *Solid Freeform Fabrication Symposium* (2010), 809–815.
- [55] T. Serra, J. A. Planell, M. Navarro, High-resolution PLA-based composite scaffolds via 3-D printing technology, *Acta Biomater.* **9**(3), 5521–5530 (2013).
- [56] F. Kotz, K. Arnold, W. Bauer, D. Schild, N. Keller, K. Sachsenheimer, T. M. Nargang, C. Richter, D. Helmer, B. E. Rapp, Three-dimensional printing of transparent fused silica glass, *Nature* **544**(7650), 337–339 (2017).
- [57] L. Hirt, S. Ihle, Z. Pan, L. Dorwling-Carter, A. Reiser, J. M. Wheeler, R. Spolenak, J. Vörös, T. Zambelli, Template-free 3D microprinting of metals using a force-controlled nanopipette for layer-by-layer electrodeposition, *Adv. Mater.* **28**(12), 2311–2315 (2016).
- [58] K. Henke, S. Treml, Wood based bulk material in 3D printing processes for applications in construction, *Eur. J. Wood Prod.* **71**(1), 139–141 (2013).
- [59] J. M. Taboas, R. D. Maddox, P. H. Krebsbach, S. J. Hollister, Indirect solid free form fabrication of local and global porous, biomimetic and composite 3D polymer-ceramic scaffolds, *Biomaterials* **24**(1), 181–194 (2003).
- [60] L. Koch, S. Kuhn, H. Sorg, M. Gruene, S. Schlie, R. Gaebel, B. Polchow, K. Reimers, S. Stoelting, N. Ma, P. M. Vogt, G. Steinhoff, B. Chichkov, Laser printing of skin cells and human stem cells, *Tissue Eng. Part C Methods* **16**(5), 847–854 (2009).
- [61] L. Jonušauskas, S. Rekštytė, M. Malinauskas, Augmentation of direct laser writing fabrication throughput for three-dimensional structures by varying focusing conditions, *Opt. Eng.* **53**(12), 125102 (2014).
- [62] L. Jonušauskas, E. Skliutas, S. Butkus, M. Malinauskas, Custom on demand 3D printing of functional microstructures, *Lith. J. Phys.* **55**(3), 227–236 (2015).
- [63] C. J. Hansen, R. Saksena, D. B. Kolesky, J. J. Vericella, S. J. Kranz, G. P. Muldowney, K. T. Christensen, J. A. Lewis, High-throughput printing via microvascular multinozzle arrays, *Adv. Mater.* **25**(1), 96–102 (2013).
- [64] D. Günther, B. Heymel, J. F. Günther, I. Ederer, Continuous 3D-printing for additive manufacturing, *Rapid Prototyping J.* **20**(4), 320–327 (2014).



- [65] G. Vizsnycizai, L. Kelemen, P. Ormos, Holographic multi-focus 3D two-photon polymerization with real-time calculated holograms, *Opt. Express* **22**(20), 24217–24223 (2014).
- [66] C. Schubert, M. C. Langeveld, L. A. Donoso, Innovations in 3D printing: a 3D overview from optics to organs, *Br. J. Ophthalmol.* **98**(2), 159–161 (2014).
- [67] C. Tröger, A. T. Bens, G. Bermes, R. Klemmer, J. Lenz, S. Irsen, Ageing of acrylate-based resins for stereolithography: thermal and humidity ageing behaviour studies, *Rapid Prototyping J.* **14**(5), 305–317 (2008).
- [68] C. E. Corcione, A. Greco, A. Maffezzoli, Photopolymerization kinetics of an epoxy-based resin for stereolithography, *J. Appl. Polym. Sci* **92**(6), 3484–3491 (2004).
- [69] Z. Wang, R. Abdulla, B. Parker, R. Samanipour, S. Ghosh, K. Kim, A simple and high-resolution stereolithography-based 3D bioprinting system using visible light crosslinkable bioinks, *Biofabrication* **7**(4), 045009 (2015).
- [70] J. Stampfl, S. Baudis, C. Heller, R. Liska, A. Neumeister, R. Kling, A. Ostendorf, M. Spitzbart, Photopolymers with tunable mechanical properties processed by laser-based high-resolution stereolithography, *J. Micromech. Microeng.* **18**(12), 125014 (2008).
- [71] C. Zhou, H. Ye, F. Zhang, A novel low-cost stereolithography process based on vector scanning and mask projection for high-accuracy, high-speed, high-throughput, and large-area fabrication, *J. Comput. Inf. Sci. Eng.* **15**(1), 011003 (2015).
- [72] N. Alharbi, R. Osman, D. Wismeijer, Effects of build direction on the mechanical properties of 3D-printed complete coverage interim dental restorations, *J. Prosthet. Dent.* **115**(6), 760–767 (2016).
- [73] C. Sun, N. Fang, D. M. Wu, X. Zhang, Projection micro-stereolithography using digital micro-mirror dynamic mask, *Sens. Actuators A Phys.* **121**(1), 113–120 (2005).
- [74] C. Y. Yap, C. K. Chua, Z. L. Dong, Z. H. Liu, D. Q. Zhang, L. E. Loh, S. L. Sing, Review of selective laser melting: Materials and applications, *Appl. Phys. Rev.* **2**(4), 041101 (2015).
- [75] S. F. S. Shirazi, S. Gharehkhani, M. Mehrali, H. Yarmand, H. S. C. Metselaar, N. A. Kadri, N. A. A. Osman, A review on powder-based additive manufacturing for tissue engineering: selective laser sintering and inkjet 3D printing, *Sci. Technol. Adv. Mater.* **16**(3), 033502 (2015).

- [76] M. Wehmöller, P. H. Warnke, C. Zilian, H. Eufinger, Implant design and production—a new approach by selective laser melting, in *Int. Congr.* (Elsevier, 2005), volume 1281, 690–695.
- [77] J. T. Rimell, P. M. Marquis, Selective laser sintering of ultra high molecular weight polyethylene for clinical applications, *J. Biomed. Mater. Res. Part A* **53**(4), 414–420 (2000).
- [78] J.-P. Kruth, L. Froyen, J. Vaerenbergh, P. Mercelis, M. Rombouts, B. Lauwers, Selective laser melting of iron-based powder, *J. Mater. Process. Technol.* **149**(1), 616–622 (2004).
- [79] B. Vandenbroucke, J.-P. Kruth, Selective laser melting of biocompatible metals for rapid manufacturing of medical parts, *Rapid Prototyping J.* **13**(4), 196–203 (2007).
- [80] H.-H. Tang, M.-L. Chiu, H.-C. Yen, Slurry-based selective laser sintering of polymer-coated ceramic powders to fabricate high strength alumina parts, *J. Eur. Ceram. Soc.* **31**(8), 1383–1388 (2011).
- [81] P. Bertrand, F. Bayle, C. Combe, P. Goeuriot, I. Smurov, Ceramic components manufacturing by selective laser sintering, *Appl. Surf. Sci.* **254**(4), 989–992 (2007).
- [82] S. Eosoly, N. E. Vrana, S. Lohfeld, M. Hindie, L. Looney, Interaction of cell culture with composition effects on the mechanical properties of polycaprolactone-hydroxyapatite scaffolds fabricated via selective laser sintering (SLS), *Mater. Sci. Eng. C* **32**(8), 2250–2257 (2012).
- [83] C. K. Chua, K. F. Leong, K. H. Tan, F. E. Wiria, C. M. Cheah, Development of tissue scaffolds using selective laser sintering of polyvinyl alcohol/hydroxyapatite biocomposite for craniofacial and joint defects, *J. Mater. Sci. Mater. Med.* **15**(10), 1113–1121 (2004).
- [84] F. S. Shirazi, M. Mehrali, A. A. Oshkour, H. S. C. Metselaar, N. A. Kadri, A. Osman, N. Azuan, Characterization and mechanical properties of calcium silicate/citric acid-based polymer composite materials, *Int. J. Appl. Ceram. Tec.* **12**(2), 371–376 (2015).
- [85] C. Yan, L. Hao, A. Hussein, D. Raymond, Evaluations of cellular lattice structures manufactured using selective laser melting, *Int. J. Mach. Tools Manuf.* **62**, 32–38 (2012).
- [86] R. J. Baseman, A. Gupta, R. C. Sausa, C. Progler, Laser induced forward transfer, *Mater. Res. Soc. Symp. Proc.* **101** (1987).
- [87] S. S. J., T. Lippert, M. Nagel, F. Nüesch, A. Wokaun, Red-green-blue polymer light-emitting diode pixels printed by optimized laser-induced forward transfer, *Appl. Phys. Lett.* **100**(20), 110 (2012).

- [88] P. Sopena, J. Arrese, S. González-Torres, J. M. Fernández-Pradas, A. Cirera, P. Serra, Low-cost fabrication of printed electronics devices through continuous wave laser-induced forward transfer, *ACS Appl. Mater. Interfaces* **9**(35), 29412–29417 (2017).
- [89] B. Hopp, T. Smausz, N. Kresz, N. Barna, Z. Bor, L. Kolozsvári, D. B. Chrisey, A. Szabó, A. Nógrádi, Survival and proliferative ability of various living cell types after laser-induced forward transfer, *Tissue Eng.* **11**(11-12), 1817–1823 (2005).
- [90] M. Duocastella, M. Colina, J. M. Fernández-Pradas, P. Serra, J. L. Morenza, Study of the laser-induced forward transfer of liquids for laser bioprinting, *Appl. Surf. Sci.* **253**(19), 7855–7859 (2007).
- [91] J. Shaw-Stewart, T. Lippert, M. Nagel, F. Nuesch, A. Wokaun, Laser-induced forward transfer of polymer light-emitting diode pixels with increased charge injection, *ACS Appl. Mater. Interfaces* **3**(2), 309–316 (2011).
- [92] R. Fardel, M. Nagel, F. Nüesch, T. Lippert, A. Wokaun, Fabrication of organic light-emitting diode pixels by laser-assisted forward transfer, *Appl. Phys. Lett.* **91**(6), 061103 (2007).
- [93] A. I. Kuznetsov, J. Koch, B. N. Chichkov, Laser-induced backward transfer of gold nanodroplets, *Opt. Express* **17**(21), 18820–18825 (2009).
- [94] F. J. Adrian, J. Bohandy, B. F. Kim, A. N. Jette, P. Thompson, A study of the mechanism of metal deposition by the laser-induced forward transfer process, *J. Vac. Sci. Technol. B* **5**(5), 1490–1494 (1987).
- [95] Z. Kantor, Z. Toth, T. Szörényi, Metal pattern deposition by laser-induced forward transfer, *Appl. Surf. Sci.* **86**(1-4), 196–201 (1995).
- [96] C. Boutopoulos, C. Pandis, K. Giannakopoulos, P. Pissis, I. Zergioti, Polymer/carbon nanotube composite patterns via laser induced forward transfer, *Appl. Phys. Lett.* **96**(4), 041104 (2010).
- [97] A. Doraiswamy, R. J. Narayan, T. Lippert, L. Urech, A. Wokaun, M. Nagel, B. Hopp, M. Dinescu, R. Modi, R. C. Y. Auyeung, D. B. Chrisey, Excimer laser forward transfer of mammalian cells using a novel triazene absorbing layer, *Appl. Surf. Sci.* **252**(13), 4743–4747 (2006).
- [98] A. I. Kuznetsov, R. Kiyan, B. N. Chichkov, Laser fabrication of 2D and 3D metal nanoparticle structures and arrays, *Opt. Express* **18**(20), 21198–21203 (2010).

- [99] J. Xu, J. Liu, D. Cui, M. Gerhold, A. Y. Wang, M. Nagel, T. K. Lippert, Laser-assisted forward transfer of multi-spectral nanocrystal quantum dot emitters, *Nanotechnology* **18**(2), 025403 (2006).
- [100] T. Gissibl, S. Thiele, A. Herkommer, H. Giessen, Two-photon direct laser writing of ultracompact multi-lens objectives, *Nat. Photon.* **10**(8), 554–560 (2016).
- [101] J. Wang, R. C. Y. Auyeung, H. Kim, N. A. Charipar, A. Piqué, Three-dimensional printing of interconnects by laser direct-write of silver nanopastes, *Adv. Mater.* **22**(40), 4462–4466 (2010).
- [102] D. P. Banks, C. Grivas, J. D. Mills, R. W. Eason, I. Zergioti, Nanodroplets deposited in microarrays by femtosecond Ti: sapphire laser-induced forward transfer, *Appl. Phys. Lett.* **89**(19), 193107 (2006).
- [103] A. Klini, P. A. Loukakos, D. Gray, A. Manousaki, C. Fotakis, Laser induced forward transfer of metals by temporally shaped femtosecond laser pulses, *Opt. Express* **16**(15), 11300–11309 (2008).
- [104] C. L. Sones, K. S. Kaur, P. Ganguly, D. P. Banks, Y. J. Ying, R. W. Eason, S. Mailis, Laser-induced-forward-transfer: a rapid prototyping tool for fabrication of photonic devices, *Appl. Phys. A* **101**(2), 333–338 (2010).
- [105] G. Comina, A. Suska, D. Filippini, PDMS lab-on-a-chip fabrication using 3D printed templates, *Lab Chip* **14**(2), 424–430 (2014).
- [106] J. L. Erkal, A. Selimovic, B. C. Gross, S. Y. Lockwood, E. L. Walton, S. McNamara, R. S. Martin, D. M. Spence, 3D printed microfluidic devices with integrated versatile and reusable electrodes, *Lab Chip* **14**(12), 2023–2032 (2014).
- [107] G. Comina, A. Suska, D. Filippini, Low cost lab-on-a-chip prototyping with a consumer grade 3D printer, *Lab Chip* **14**(16), 2978–2982 (2014).
- [108] A. Rios, M. Zougagh, M. Avila, Miniaturization through lab-on-a-chip: Utopia or reality for routine laboratories? A review, *Anal. Chim. Acta* **740**, 1–11 (2012).
- [109] V. C. Romao, S. A. M. Martins, J. Germano, F. A. Cardoso, S. Cardoso, P. P. Freitas, Lab-on-chip devices: Gaining ground losing size, *ACS Nano* **in press** (2017).
- [110] R. Sodian, M. Loebe, A. Hein, T. Lueth, D. P. Martin, E. V. Potapov, F. Knollmann, R. Hetzer, Application of stereolithography for scaffold fabrication for tissue engineering of heart valves, *ASAIO J.* **48**(1), 12–16 (2002).

- [111] R. Gauvin, Y.-C. Chen, J. W. Lee, P. Soman, P. Zorlutuna, J. W. Nichol, H. Bae, S. Chen, A. Khademhosseini, Microfabrication of complex porous tissue engineering scaffolds using 3D projection stereolithography, *Biomaterials* **33**(15), 3824–3834 (2012).
- [112] M. N. Cooke, J. P. Fisher, D. Dean, C. Rimmnac, A. G. Mikos, Use of stereolithography to manufacture critical-sized 3D biodegradable scaffolds for bone ingrowth, *J. Biomed. Mater. Res. Part B Appl. Biomater.* **64**(2), 65–69 (2003).
- [113] B. Dhariwala, E. Hunt, T. Boland, Rapid prototyping of tissue-engineering constructs, using photopolymerizable hydrogels and stereolithography, *Tissue Eng.* **10**(9-10), 1316–1322 (2004).
- [114] T. Rayna, L. Striukova, From rapid prototyping to home fabrication: How 3D printing is changing business model innovation, *Technol. Forecast. Soc. Change* **102**, 214–224 (2016).
- [115] E. Fogarassy, C. Fuchs, F. Kerherve, G. Hauchecorne, J. Perriere, Laser-induced forward transfer: A new approach for the deposition of high Tc superconducting thin films, *J. Mater. Res.* **4**(5), 1082–1086 (1989).
- [116] M. Duocastella, H. Kim, P. Serra, A. Piqué, Optimization of laser printing of nanoparticle suspensions for microelectronic applications, *Appl. Phys. A* **106**(3), 471–478 (2012).
- [117] G. Comina, A. Suska, D. Filippini, 3D printed disposable optics and lab-on-a-chip devices for chemical sensing with cell phones, in *Proc. SPIE* (2017), volume 10061, 100610E–1.
- [118] T. Kamal, R. Watkins, Z. Cen, W. M. Lee, Direct fabrication of silicone lenses with 3D printed parts, in *Proc. SPIE* (International Society for Optics and Photonics, 2016), volume 10013, 1001336.
- [119] A. Okunkova, M. Volosova, P. Peretyagin, Y. Vladimirov, I. Zhirnov, A. V. Gusarov, Experimental approbation of selective laser melting of powders by the use of non-gaussian power density distributions, *Physics Procedia* **56**, 48–57 (2014).
- [120] A. A. Okunkova, P. Y. Peretyagin, P. A. Podrabinnik, I. V. Zhirnov, A. V. Gusarov, Development of laser beam modulation assets for the process productivity improvement of selective laser melting, *Procedia IUTAM* **23**, 177–186 (2017).
- [121] D. J. Heath, M. Feinaeugle, J. A. Grant-Jacob, B. Mills, R. W. Eason, Dynamic spatial pulse shaping via a digital micromirror device for patterned laser-induced forward transfer of solid polymer films, *Opt. Mater. Express* **5**(5), 1129–1136 (2015).

- [122] R. C. Y. Auyeung, H. Kim, S. Mathews, A. Piqué, Laser forward transfer using structured light, *Opt. Express* **23**(1), 422–430 (2015).
- [123] L. Fertier, H. Koleilat, M. Stemmelen, O. Giani, C. Joly-Duhamel, V. Lapinte, J. J. Robin, The use of renewable feedstock in UV-curable materials—a new age for polymers and green chemistry, *Prog. Polym. Sci.* **38**(6), 932–962 (2013).
- [124] S. Kašėtaitė, J. Ostrauskaitė, V. Gražulevičienė, J. Svedienė, D. Bridžiuvienė, Photocross-linking of glycerol diglycidyl ether with reactive diluents, *Polym. Bull.* **72**(12), 3191–3208 (2015).
- [125] M. Schwentenwein, J. Homa, Additive manufacturing of dense alumina ceramics, *Int. J. of Appl. Ceram. Tec.* **12**(1), 1–7 (2015).
- [126] Z. C. Eckel, C. Zhou, J. H. Martin, A. J. Jacobsen, W. B. Carter, T. A. Schaedler, Additive manufacturing of polymer-derived ceramics, *Science* **351**(6268), 58–62 (2016).
- [127] J. N. Gonsalves, W. W. Duley, Cutting thin metal sheets with the cw CO<sub>2</sub> laser, *J. Appl. Phys.* **43**(11), 4684–4687 (1972).
- [128] H. Tonshoff, D. Hesse, J. Mommsen, Micromachining using excimer lasers, *CIRP Annals* **42**(1), 247–251 (1993).
- [129] A. Hideur, T. Chartier, M. Brunel, M. Salhi, C. Ozkul, F. Sanchez, Mode-lock, Q-switch and CW operation of an Yb-doped double-clad fiber ring laser, *Opt. Commun.* **198**(1-3), 141–146 (2001).
- [130] U. Morgner, F. X. Kärtner, S. H. Cho, Y. Chen, H. A. Haus, J. G. Fujimoto, E. P. Ippen, V. Scheuer, G. Angelow, T. Tschudi, Sub-two-cycle pulses from a Kerr-lens mode-locked Ti: sapphire laser, *Opt. Lett.* **24**(6), 411–413 (1999).
- [131] L. V. Keldysh, Ionization in the field of a strong electromagnetic wave, *Sov. Phys. JETP* **20**(5), 1307–1314 (1965).
- [132] C. B. Schaffer, A. Brodeur, E. Mazur, Laser-induced breakdown and damage in bulk transparent materials induced by tightly focused femtosecond laser pulses, *Meas. Sci. Technol.* **12**(11), 1784 (2001).
- [133] M. Malinauskas, A. Žukauskas, G. Bičkauskaitė, R. Gadonas, S. Juodkasis, Mechanisms of three-dimensional structuring of photopolymers by tightly focussed femtosecond laser pulses, *Opt. Express* **18**(10), 10209 (2010).
- [134] L. Jonušauskas, M. Lau, P. Gruber, B. Gokce, S. Barcikowski, M. Malinauskas, A. Ovsianikov, Plasmon assisted 3D microstructuring of gold nanoparticle-doped polymers, *Nanotechnology* **27**(15), 154001 (2016).

- [135] D. Arnold, E. Cartier, Theory of laser-induced free-electron heating and impact ionization in wide-band-gap solids, *Phys. Rev. B* **46**(23), 15102–15115 (1992).
- [136] B. C. Stuart, M. D. Feit, S. Herman, A. M. Rubenchik, B. W. Shore, M. D. Perry, Nanosecond-to-femtosecond laser-induced breakdown in dielectrics, *Phys. Rev. B* **53**(4), 1749 (1996).
- [137] P. S. Binder, Flap dimensions created with the IntraLase FS laser, *J. Cataract. Refract. Surg.* **30**(1), 26–32 (2004).
- [138] E. Garškaitė, L. Alinauskas, M. Drienovsky, J. Krajcovic, R. Cicka, M. Palcut, L. Jonušauskas, M. Malinauskas, Z. Stankeviciute, A. Kareiva, Fabrication of a composite of nanocrystalline carbonated hydroxyapatite (cHAP) with polylactic acid (PLA) and its surface topographical structuring with direct laser writing (DLW), *RSC Advances* **6**(76), 72733–72743 (2016).
- [139] K. Furusawa, K. Takahashi, H. Kumagai, K. Midorikawa, M. Obara, Ablation characteristics of Au, Ag, and Cu metals using a femtosecond Ti:sapphire laser, *Appl. Phys. A* **69**(7), S359–S366 (1999).
- [140] J. Kruger, W. Kautek, M. Lenzner, S. Sartania, C. Spielmann, F. Krausz, Laser micromachining of barium aluminium borosilicate glass with pulse durations between 20 fs and 3 ps, *Appl. Surf. Sci.* **127–129**, 892–898 (1998).
- [141] S. Xu, J. Qiu, T. Jia, C. Li, H. Sun, Z. Xu, Femtosecond laser ablation of crystals SiO<sub>2</sub> and YAG, *Opt. Commun.* **274**(1), 163–166 (2007).
- [142] C. Kerse, H. Kalaycıoğlu, P. Elahi, B. Çetin, D. K. Kesim, Ö. Akçaalan, S. Yavaş, M. D. Aşık, B. Öktem, H. Hoogland, R. Holzwarth, F. Ö. Ilday, Ablation-cooled material removal with ultrafast bursts of pulses, *Nature* **537**(7618), 84–88 (2016).
- [143] R. Jagdheesh, B. Pathiraj, E. Karatay, G. R. B. E. Roomer, A. J. H. in't Veld, Laser-induced nanoscale superhydrophobic structures on metal surfaces, *Langmuir* **27**(13), 8464–8469 (2011).
- [144] D. V. Ta, A. Dunn, T. J. Wasley, R. W. Kay, J. Stringer, P. J. Smith, C. Connaughton, J. D. Shephard, Nanosecond laser textured superhydrophobic metallic surfaces and their chemical sensing applications, *Appl. Surf. Sci.* **357**, 248–254 (2015).
- [145] S. Moradi, S. Kamal, P. Englezos, S. G. Hatzikiriakos, Femtosecond laser irradiation of metallic surfaces: effects of laser parameters on superhydrophobicity, *Nanotechnology* **24**(41), 415302 (2013).

- [146] M. Martínez-Calderon, A. Rodríguez, A. Dias-Ponte, M. C. Morant-Miñana, M. Gómez-Aranzadi, S. M. Olaizola, Femtosecond laser fabrication of highly hydrophobic stainless steel surface with hierarchical structures fabricated by combining ordered microstructures and LIPSS, *Appl. Surf. Sci.* **374**, 81–89 (2016).
- [147] J. E. Sipe, J. F. Young, J. S. Preston, H. M. van Driel, Laser-induced periodic surface structure. I. Theory, *Phys. Rev. B* **27**(2), 1141–1154 (1983).
- [148] A. Borowiec, H. K. Haugen, Subwavelength ripple formation on the surfaces of compound semiconductors irradiated with femtosecond laser pulses, *Appl. Phys. Lett.* **82**(25), 4462–4464 (2003).
- [149] J.-W. Yao, C.-Y. Zhang, H.-Y. Liu, Q.-F. Dai, L.-J. Wu, S. Lan, A. V. Gopal, V. A. Trofimov, T. M. Lysak., High spatial frequency periodic structures induced on metal surface by femtosecond laser pulses, *Opt. Express* **20**(2), 905 (2012).
- [150] T. Baldacchini, J. E. Carey, M. Zhou, E. Mazur, Superhydrophobic surfaces prepared by microstructuring of silicon using a femtosecond laser, *Langmuir* **22**(11), 4917–4919 (2006).
- [151] A. Milionis, D. Fragouli, F. Brandi, I. Liakos, S. Barroso, R. Ruffilli, A. Athanassiou, Superhydrophobic/superoleophilic magnetic elastomers by laser ablation, *Appl. Surf. Sci.* **351**, 74–82 (2015).
- [152] S. F. Toosi, S. Moradi, S. Kamal, S. G. Hatzikiriakos, Superhydrophobic laser ablated PTFE substrates, *Appl. Surf. Sci.* **349**, 715–723 (2015).
- [153] D. Gailevičius, V. Koliadenko, V. Purlys, M. Peckus, V. Taranenko, K. Staliunas, Photonic crystal microchip laser, *Sci. Rep.* **6**, 34173 (2016).
- [154] M. Martínez-Calderon, J. J. Azkona, N. Casquero, A. Rodríguez, M. Domke, M. Gómez-Aranzadi, S. M. Olaizola, E. Granados, Tailoring diamond’s optical properties via direct femtosecond laser nanosstructuring, *Sci. Rep.* **8**(1), 14262 (2018).
- [155] W. Cai, A. R. Libertun, R. Piestun, Polarization selective computer-generated holograms realized in glass by femtosecond laser induced nanogratings, *Opt. Express* **14**(9), 3785–3791 (2006).
- [156] R. Taylor, C. Hnatovsky, E. Simova, Applications of femtosecond laser induced self-organized planar nanocracks inside fused silica glass, *Laser Photonics Rev.* **2**(1-2), 26–46 (2008).



- [157] M. Beresna, M. Gecevičius, P. G. Kazansky, T. Gertus, Radially polarized optical vortex converter created by femtosecond laser nanostructuring of glass, *Appl. Phys. Lett.* **98**(20), 201101 (2011).
- [158] C. A. Ross, D. G. MacLachlan, D. Choudhury, R. R. Thomson, Optimisation of ultrafast laser assisted etching in fused silica, *Opt. Express* **26**(19), 24343–24356 (2018).
- [159] J. Gottmann, M. Hermans, J. Ortmann, Microcutting and hollow 3D microstructures in glasses by in-volume selective laser-induced etching (ISLE), *J. Laser. Micro. Nanoeng.* **8**(1), 15–18 (2013).
- [160] A. Žemaitis, M. Gaidys, P. Gečys, G. Račiukaitis, M. Gedvilas, Rapid high-quality 3D micro-machining by optimised efficient ultrashort laser ablation, *Opt. Lasers Eng.* **114**, 83–89 (2018).
- [161] Y. Bellouard, A. Said, M. Dugan, P. Bado, Fabrication of high-aspect ratio, micro-fluidic channels and tunnels using femtosecond laser pulses and chemical etching, *Opt. Express* **12**(10), 2120–2129 (2004).
- [162] Y. Zhang, S. Fan, L. Yan, L. Zhang, X. Zhang, W. Guo, S. Zhang, H. Jiang, Robust optical-frequency-comb based on the hybrid mode-locked Er: fiber femtosecond laser, *Opt. Express* **25**(18), 21719–21725 (2017).
- [163] F. Lesparre, J. T. Gomes, X. Délen, I. Martial, J. Didierjean, W. Pallmann, B. Resan, M. Eckerle, T. Graf, M. A. Ahmed, F. Druon, F. Balembos, P. Georges, High-power Yb:YAG single-crystal fiber amplifiers for femtosecond lasers in cylindrical polarization, *Opt. Lett.* **40**(11), 2517–2520 (2015).
- [164] F. V. Potemkin, B. G. Bravy, V. I. Kozlovsky, Y. V. Korostelin, E. A. Migal, Y. P. Podmarkov, A. A. Podshivalov, V. T. Platonenko, V. V. Firsov, M. P. Frolov, V. M. Gordienko, Toward a sub-terawatt mid-IR (4–5 $\mu\text{m}$ ) femtosecond hybrid laser system based on parametric seed pulse generation and amplification in Fe<sup>2+</sup>:ZnSe, *Laser Phys. Lett.* **13**(1), 015401 (2015).
- [165] J. Dudutis, J. Pipiras, R. Stonys, E. Daknys, A. Kilikevičius, A. Kasparaitis, G. Račiukaitis, P. Gečys, In-depth comparison of conventional glass cutting technologies with laser-based methods by volumetric scribing using bessel beam and rear-side machining, *Opt. Express* **28**(21), 32133–32151 (2020).
- [166] J. Torgersen, A. Ovsianikov, V. Mironov, N. Pucher, X. Qin, Z. Li, K. Cicha, T. Machacek, R. Liska, V. Jantsch, J. Stampfl, Photosensitive hydrogels for three-dimensional laser microfabrication in the presence of whole organisms, *J. Biomed. Opt.* **17**(10), 105008 (2012).

- [167] A. Vyatskikh, S. Delalande, A. Kudo, X. Zhang, C. M. Portela, J. R. Greer, Additive manufacturing of 3D nano-architected metals, *Nat. Commun.* **9**(1), 593 (2018).
- [168] L. Jonušauskas, D. Gailevičius, S. Rekštytė, T. Baldacchini, S. Juodkazis, M. Malinauskas, Mesoscale laser 3D printing, *Opt. Express* **27**(11), 15205–15221 (2019).
- [169] Y. Nakata, Y. Matsuba, N. Miyanaga, Sub-micron period metal lattices fabricated by interfering ultraviolet femtosecond laser processing, *Appl. Phys. A* **122**(5), 532 (2016).
- [170] L. Yang, A. El-Tamer, U. Hinze, J. Li, Y. Hu, W. Huang, J. Chu, B. N. Chichkov, Parallel direct laser writing of micro-optical and photonic structures using spatial light modulator, *Opt. Lasers Eng.* **70**, 26–32 (2015).
- [171] P. S. Salter, M. Baum, I. Alexeev, M. Schmidt, M. J. Booth, Exploring the depth range for three-dimensional laser machining with aberration correction, *Opt. Express* **22**(15), 17644–17656 (2014).
- [172] G. R. B. E. Romer, P. Bechtold, Electro-optic and acousto-optic laser beam scanners, *Phys. Procedia* **56**, 29–39 (2014).
- [173] A. Žemaitis, P. Gečys, M. Barkauskas, G. Račiukaitis, M. Gedvilas, Highly-efficient laser ablation of copper by bursts of ultrashort tunable (fs-ps) pulses, *Sci. Rep.* **9**(1), 12280 (2019).
- [174] K. Sugioka, Progress in ultrafast laser processing and future prospects, *Nanophotonics* **6**(2), 393–413 (2017).
- [175] D. Tan, K. N. Sharafudeen, Y. Yue, J. Qiu, Femtosecond laser induced phenomena in transparent solid materials: Fundamentals and applications, *Prog. Mater. Sci.* **76**, 154–228 (2016).
- [176] J. Serbin, A. Egbert, A. Ostendorf, B. N. Chichkov, R. Houbertz, G. Domann, J. Schulz, C. Cronauer, L. Fröhlich, M. Popall, Femtosecond laser-induced two-photon polymerization of inorganic–organic hybrid materials for applications in photonics, *Opt. Lett.* **28**(5), 301–303 (2003).
- [177] M. T. Raimondi, S. M. Eaton, M. M. Nava, M. Laganà, G. Cerullo, R. Osellame, Two-photon laser polymerization: from fundamentals to biomedical application in tissue engineering and regenerative medicine, *J. Appl. Biomater. Biomech.* **10**(1), 55–65 (2012).
- [178] I. Sakellari, E. Kabouraki, D. Gray, V. Purlys, C. Fotakis, A. Pikulin, N. Bityurin, M. Vamvakaki, M. Farsari, Diffusion-assisted high-resolution direct femtosecond laser writing, *ACS Nano* **6**(3), 2302–2311 (2012).

- [179] R. Buividas, S. Rekštytė, M. Malinauskas, S. Juodkazis, Nano-groove and 3D fabrication by controlled avalanche using femtosecond laser pulses, *Opt. Mater. Express* **3**(10), 1674–1686 (2013).
- [180] E. G. Gamaly, *Femtosecond Laser-Matter Interaction: Theory, Experiments and Applications* (CRC Press, 2011).
- [181] A. Ovsianikov, J. Viertl, B. Chichkov, M. Oubaha, B. MacCraith, I. Sakellari, A. Giakoumaki, D. Gray, M. Vamvakakian, M. Farsari, C. Fotakis, Ultra-low shrinkage hybrid photosensitive material for two-photon polymerization microfabrication, *ACS Nano* **2**(11), 2257–2262 (2008).
- [182] M. Malinauskas, M. Farsari, A. Piskarskas, S. Juodkazis, Ultrafast laser nanostructuring of photopolymers: A decade of advances, *Phys. Rep.* **553**, 1–31 (2013).
- [183] J. Galinis, G. Tamošauskas, I. Gražulevičiūtė, E. Keblytė, V. Jukna, A. Dubietis, Filamentation and supercontinuum generation in solid-state dielectric media with picosecond laser pulses, *Phys. Rev. A* **92**(3), 033857 (2015).
- [184] A. Žukauskas, M. Malinauskas, G. Seniutinas, S. Juodkazis, *Rapid Laser Optical Printing in 3D at a Nanoscale* (Wiley-Blackwell, 2016).
- [185] J. Morikawa, A. Orié, T. Hashimoto, S. Juodkazis, Thermal diffusivity in femtosecond-laser-structured micro-volumes of polymers, *Appl. Phys. A* **98**(3), 551–556 (2010).
- [186] D. T. T. Nguyen, Q. C. Tong, I. L.-Rak, N. D. Lai, One-step fabrication of submicrostructures by low one-photon absorption direct laser writing technique with local thermal effect, *J. Appl. Phys.* **119**(1), 013101 (2016).
- [187] J. B. Mueller, J. Fischer, Y. J. Mange, T. Nann, M. Wegener, In-situ local temperature measurement during three-dimensional direct laser writing, *Appl. Phys. Lett.* **103**(12), 123107 (2013).
- [188] M. Malinauskas, H. Gilbergs, A. Žukauskas, V. Purlys, D. Paipulas, R. Gadonas, A femtosecond laser induced two-photon photopolymerization technique for structuring microlenses, *J. Opt.* **12**(3), 035204 (2010).
- [189] S. Rekštytė, T. Jonavičius, D. Gailevičius, M. Malinauskas, V. Mizeikis, E. G. Gamaly, S. Juodkazis, Nanoscale precision of 3D polymerization via polarization control, *Adv. Opt. Mater.* **4**(8), 1209–1214 (2016).

- [190] W. Haske, V. W. Chen, J. M. Hales, W. Dong, S. Barlow, S. R. Marder, J. W. Perry, 65 nm feature sizes using visible wavelength 3-D multiphoton lithography, *Opt. Express* **15**(6), 3426–3436 (2007).
- [191] M. Malinauskas, P. Danilevičius, S. Juodkazis, Three-dimensional micro-/nano-structuring via direct write polymerization with picosecond laser pulses, *Opt. Express* **19**(6), 5602–5610 (2011).
- [192] S. Hengsbach, A. D. Lantada, Direct laser writing of auxetic structures: present capabilities and challenges, *Smart Mater. Struct.* **23**(8), 085033 (2014).
- [193] M. Malinauskas, L. Lukoševičius, D. Mackevičiūtė, E. Balčiūnas, S. Rekštytė, D. Paipulas, Multiscale 3D manufacturing: combining thermal extrusion printing with additive and subtractive direct laser writing, in *Proc. SPIE* (International Society for Optics and Photonics, 2014), 91350T–91350T.
- [194] A. Ovsianikov, M. Gruene, M. Pflaum, L. Koch, F. Maiorana, M. Wilhelm, A. Haverich, B. Chichkov, Laser printing of cells into 3D scaffolds, *Biofabrication* **2**, 014104 (2010).
- [195] T. Tičkūnas, M. Perrenoud, S. Butkus, R. Gadonas, S. Rekštytė, M. Malinauskas, D. Paipulas, Y. Bellouard, V. Sirutkaitis, Combination of additive and subtractive laser 3D microprocessing in hybrid glass/polymer microsystems for chemical sensing applications, *Opt. Express* **25**(21), 26280–26288 (2017).
- [196] S. Rekštytė, D. Paipulas, M. Malinauskas, V. Mizeikis, Microactuation and sensing using reversible deformations of laser-written polymeric structures, *Nanotechnology* **28**, 124001 (2017).
- [197] Z. X. Khoo, J. E. M. Teoh, Y. Liu, C. K. Chua, S. Yang, J. An, K. F. Leong, W. Y. Yeong, 3D printing of smart materials: A review on recent progresses in 4D printing, *Virtual Phys. Prototyp.* **10**(3), 103–122 (2015).
- [198] F. Klein, B. Richter, T. Striebel, C. M. Franz, G. Freymann, M. Wegener, M. Bastmeyer, Two-component polymer scaffolds for controlled three-dimensional cell culture, *Adv. Mater.* **23**(11), 1341–1345 (2011).
- [199] A. Žukauskas, I. Matulaitienė, D. Paipulas, G. Niaura, M. Malinauskas, R. Gadonas, Tuning the refractive index in 3D direct laser writing lithography: towards GRIN microoptics, *Laser Photon. Rev.* **9**(6), 706–712 (2015).

- [200] Q. Sun, S. Juodkazis, N. Murazawa, V. Mizeikis, H. Misawa, Free-standing and movable photonic microstructures fabricated by photopolymerization with femtosecond laser pulses, *J. Micromech. Microeng.* **20**, 035004 (2010).
- [201] C. Schizas, V. Melissinaki, A. Gaidukevičiūtė, C. Reinhardt, C. Ohrt, V. Dedoussis, B. N. Chichkov, M. F. C. Fotakis, D. Karalekas, On the design and fabrication by two-photon polymerization of a readily assembled micro-valve, *Int. J. Adv. Manuf. Technol.* **48**, 435–441 (2010).
- [202] T. Bückmann, N. Stenger, M. Kadic, J. Kaschke, A. Frölich, T. Kennerknecht, C. Eberl, M. Thiel, M. Wegener, Tailored 3D mechanical metamaterials made by dip-in direct-laser-writing optical lithography, *Adv. Mater.* **24**(20), 2710–2714 (2012).
- [203] T. Bückmann, M. Thiel, M. Kadic, R. Schittny, M. Wegener, An elasto-mechanical unfeelability cloak made of pentamode metamaterials, *Nat. Commun.* **5**, 4130 (2014).
- [204] B. B. Xu, Y. L. Zhang, H. Xia, W. F. Dong, H. Ding, H. B. Sun, Fabrication and multifunction integration of microfluidic chips by femtosecond laser direct writing, *Lab Chip* **13**(9), 1677–1690 (2013).
- [205] Y. He, B.-L. Huang, D. X. Lu, J. Zhao, B. B. Xu, R. Zhang, X. F. Lin, Q. D. Chen, J. Wang, Y. L. Zhang, H. B. Sun, “overpass” at the junction of a crossed microchannel: An enabler for 3D microfluidic chips, *Lab Chip* **12**(20), 3866–3869 (2012).
- [206] P. Danilevičius, R. A. Rezende, F. D. A. S. Pereira, A. Selimis, V. Kasyanov, P. Y. Noritomi, J. V. L. da Silva, M. Chatzinikolaïdou, M. Farsari, V. Mironov, Burr-like, laser-made 3D microscaffolds for tissue spheroid engagement, *Biointerphases* **10**(2), 021011 (2015).
- [207] P. Timashev, D. Kuznetsova, A. Koroleva, N. Prodanets, A. Deiwick, Y. Piskun, K. Bardakova, N. Dzhoyashvili, S. Kostjuk, E. Zagaynova, Y. Rochev, B. N. Chichkov, V. Bagratashvili, Novel biodegradable star-shaped polylactide scaffolds for bone regeneration fabricated by two-photon polymerization, *Nanomedicine* **11**(9), 1041–1053 (2016).
- [208] M. Malinauskas, D. Baltrikienė, A. Kraniauskas, P. Danilevičius, R. Jarasienė, R. Sirmenis, A. Žukauskas, E. Balčiūnas, V. Purlys, R. Gadonas, V. Bukelskienė, V. Sirvydis, A. Piskarskas, In vitro and in vivo biocompatibility study on laser 3D microstructurable polymers, *Appl. Phys. A* **108**(3), 751–759 (2012).
- [209] V. Melissinaki, A. A. Gill, I. Ortega, M. Vamvakaki, A. Ranella, J. W. Haycock, C. Fotakis, M. Farsari, F. Claeysens, Direct laser writing of

- 3D scaffolds for neural tissue engineering applications, *Biofabrication* **3**, 245005 (2011).
- [210] M. Malinauskas, A. Žukauskas, V. Purlys, K. Belazaras, A. Momot, D. Paipulas, R. Gadonas, A. Piskarskas, H. Gilbergs, A. Gaidukevičiūtė, I. Sakellari, M. Farsari, S. Juodkazis, Femtosecond laser polymerization of hybrid/integrated micro-optical elements and their characterization, *J. Opt.* **12**(12), 124010 (2010).
- [211] A. Žukauskas, M. Malinauskas, E. Brasselet, Monolithic generators of pseudo-nondiffracting optical vortex beams at the microscale, *Appl. Phys. Lett.* **103**(18), 181122 (2013).
- [212] A. Žukauskas, V. Melissinaki, D. Kaškelytė, M. Farsari, M. Malinauskas, Improvement of the fabrication accuracy of fiber tip microoptical components via mode field expansion, *JLMN* **9**(1), 68–72 (2014).
- [213] S. Thiele, K. Arzenbacher, T. Gissibl, H. Giessen, A. M. Herkommer, 3D-printed eagle eye: Compound microlens system for foveated imaging, *Sci. Adv.* **3**(2), e1602655 (2017).
- [214] A. Žukauskas, G. Batavičiūtė, M. Ščiuka, T. Jukna, A. Melninkaitis, M. Malinauskas, Characterization of photopolymers used in laser 3D micro/nanolithography by means of laser-induced damage threshold (LIDT), *Opt. Mater. Express* **4**(8), 1601–1616 (2014).
- [215] A. Radke, T. Gissibl, T. Klotzbücher, P. V. Braun, H. Giessen, Three-dimensional bichiral plasmonic crystals fabricated by direct laser writing and electroless silver plating, *Adv. Mater.* **23**(27), 3018–3021 (2011).
- [216] J. K. Gansel, M. Thiel, M. S. Rill, M. Decker, K. Bade, V. Saile, G. Freymann, S. Linden, M. Wegener, Gold helix photonic metamaterial as broadband circular polarizer, *Science* **325**(5947), 1513–1515 (2009).
- [217] *Aerotech 3200 Manual* (Aerotech Inc., USA, 2019).
- [218] ISO21254-2:2011, *Test methods for laser-induced damage threshold-Part 2: Threshold determination* (2011).
- [219] G. Batavičiūtė, P. Grigas, L. Smalakys, A. Melninkaitis, Revision of laser-induced damage threshold evaluation from damage probability data, *Rev. Sci. Instrum.* **84**(4), 045108 (2013).
- [220] X. Chen, W. Liu, B. Dong, J. Lee, H. O. T. Ware, H. F. Zhang, C. Sun, High-speed 3D printing of millimeter-size customized aspheric imaging lenses with sub 7 nm surface roughness, *Adv. Mater.* **30**(18), 1705683 (2018).

- [221] E. Waller, G. Freymann, Spatio-temporal proximity characteristics in 3D  $\mu$ -printing via multi-photon absorption, *Polymers* **8**(8), 297 (2016).
- [222] R. D. Loor, Polygon scanner system for ultra short pulsed laser micro-machining applications, *Phys. Procedia* **41**, 544–551 (2013).
- [223] D. J. Rosenkrantz, R. E. Stearns, P. M. Lewis, Approximate algorithms for the traveling salesperson problem, in *15th Annual Symposium on Switching and Automata Theory* (IEEE, 1974), 33–42.
- [224] A. Žukauskas, M. Malinauskas, L. Kontenis, V. Purlys, D. Paipulas, M. Vengris, R. Gadonas, Organic dye doped microstructures for optically active functional devices fabricated via two-photon polymerization technique, *Lith. J. Phys.* **50**(1), 55–61 (2010).
- [225] P. Prabhakaran, Y. Son, C.-W. Ha, J.-J. Park, S. Jeon, K.-S. Lee, Optical materials forming tightly polymerized voxels during laser direct writing, *Adv. Eng. Mater.* **20**(10), 1800320 (2018).
- [226] S. Beke, B. Farkas, I. Romano, F. Brandi, 3D scaffold fabrication by mask projection excimer laser stereolithography, *Opt. Mater. Express* **4**(10), 2032–2041 (2014).
- [227] D. T. Pham, C. Ji, A study of recoating in stereolithography, *Proc. Inst. Mech. Eng.* **217**(1), 105–117 (2003).
- [228] K. Renap, J. Kruth, Recoating issues in stereolithography, *Rapid Prototyp. J.* **1**(3), 4–16 (1995).
- [229] E. Skliutas, S. Kašetaitė, L. Jonušauskas, J. Ostrauskaitė, M. Malinauskas, Photosensitive naturally derived resins toward optical 3-D printing, *Opt. Eng.* **57**(04), 1 (2018).
- [230] M. Lebedevaitė, J. Ostrauskaitė, E. Skliutas, M. Malinauskas, Photoinitiator free resins composed of plant-derived monomers for the optical  $\mu$ -3D printing of thermosets, *Polymers* **11**(1), 116 (2019).
- [231] P. E. Petrochenko, J. Torgersen, P. Gruber, L. A. Hicks, J. Zheng, G. Kumar, R. J. Narayan, P. L. Goering, R. Liska, J. Stampfl, A. Ovsianikov, Laser 3D printing with sub-microscale resolution of porous elastomeric scaffolds for supporting human bone stem cells, *Adv. Health. Mater.* **4**(5), 739–747 (2014).
- [232] S. Pashneh-Tala, R. Owen, H. Bahmaee, S. Rekštytė, M. Malinauskas, F. Claeysens, Synthesis, characterization and 3D micro-structuring via 2-photon polymerization of poly(glycerol sebacate)-methacrylate - an elastomeric degradable polymer, *Front. Phys.* **6**, 41 (2018).

- [233] <https://www.micro-shop.zeiss.com/en/us/shop/objectives/420782-9900-000/objective-plan-apochromat-63x-1.4-oil-dic-m27> (2021 January 22).
- [234] K. Obata, A. El-Tamer, L. Koch, U. Hinze, B. N. Chichkov, High-aspect 3D two-photon polymerization structuring with widened objective working range (WOW-2PP), *Light Sci. Appl.* **2**(12), e116–e116 (2013).
- [235] S. Bonora, Y. Jian, P. Zhang, A. Zam, E. N. Pugh, R. J. Zawadzki, M. V. Sarunic, Wavefront correction and high-resolution in vivo OCT imaging with an objective integrated multi-actuator adaptive lens, *Opt. Express* **23**(17), 21931–21941 (2015).
- [236] L. Li, D. Wang, C. Liu, Q.-H. Wang, Zoom microscope objective using electrowetting lenses, *Opt. Express* **24**(3), 2931–2940 (2016).
- [237] P. S. Salter, M. Baum, I. Alexeev, M. Schmidt, M. J. Booth, Exploring the depth range for three-dimensional laser machining with aberration correction, *Opt. Express* **22**(15), 17644 (2014).
- [238] G. Kontenis, D. Gailevičius, L. Jonušauskas, V. Purlys, Dynamic aberration correction via spatial light modulator (SLM) for femtosecond direct laser writing: towards spherical voxels, *Opt. Express* **28**(19), 27850–27864 (2020).
- [239] Z. He, Y.-H. Lee, D. Chanda, S.-T. Wu, Adaptive liquid crystal microlens array enabled by two-photon polymerization, *Opt. Express* **26**(16), 21184–21193 (2018).
- [240] A. C. Lamont, A. T. Alsharhan, R. D. Sochol, Geometric determinants of in-situ direct laser writing, *Sci. Rep.* **9**(1), 394 (2019).
- [241] L. Jonušauskas, S. Rekštytė, M. Malinauskas, Augmentation of direct laser writing fabrication throughput for three-dimensional structures by varying focusing conditions, *Opt. Eng.* **53**(12), 125102 (2014).
- [242] D. W. Abueidda, M. Elhebeary, C.-S. Shiang, S. Pang, R. K. A. Al-Rub, I. M. Jasiuk, Mechanical properties of 3D printed polymeric gyroid cellular structures: Experimental and finite element study, *Mater. Des.* **165**, 107597 (2019).
- [243] P.-I. Dietrich, M. Blaicher, I. Reuter, M. Billah, T. Hoose, A. Hofmann, C. Caer, R. Dangel, B. Offrein, U. Troppenz, M. Moehrle, W. Freude, C. Koos, In situ 3D nanoprinting of free-form coupling elements for hybrid photonic integration, *Nat. Photonics* **12**(4), 241–247 (2018).



- [244] R. Buividas, S. Rekštytė, M. Malinauskas, S. Juodkakis, Nano-groove and 3D fabrication by controlled avalanche using femtosecond laser pulses, *Opt. Mater. Express* **3**(10), 1674–1686 (2013).
- [245] K. Obata, S. Slobin, A. Schonewille, A. Hohnholz, C. Unger, J. Koch, O. Suttmann, L. Overmeyer, UV laser direct writing of 2D/3D structures using photo-curable polydimethylsiloxane (PDMS), *Appl. Phys. A* **123**(7), 495 (2017).
- [246] J. Qu, M. Kadic, M. Wegener, Three-dimensional poroelastic metamaterials with extremely negative or positive effective static volume compressibility, *Extreme Mech. Lett.* **22**, 165–171 (2018).
- [247] S. Maruo, H. Inoue, Optically driven micropump produced by three-dimensional two-photon microfabrication, *Appl. Phys. Lett.* **89**(14), 144101 (2006).
- [248] J. Kohler, S. I. K., C. Esen, A. Ostendorf, Optical screw-wrench for microassembly, *Microsyst. Nanoeng.* **3**, 16083 (2017).
- [249] M. Suter, L. Zhang, E. C. Siringil, C. Peters, T. Luehmann, O. Ergeneman, K. E. Peyer, B. J. Nelson, C. Hierold, Superparamagnetic microrobots: fabrication by two-photon polymerization and biocompatibility, *Biomed. Microdevices* **15**(6), 997–1003 (2013).
- [250] S. Kim, F. Qiu, S. Kim, A. Ghanbari, C. Moon, L. Zhang, B. J. Nelson, H. Choi, Fabrication and characterization of magnetic microrobots for three-dimensional cell culture and targeted transportation, *Adv. Mater.* **25**(41), 5863–5868 (2013).
- [251] A. Buguin, M.-H. Li, P. Silberzan, B. Ladoux, P. Keller, Microactuators: When artificial muscles made of nematic liquid crystal elastomers meet soft lithography, *J. Am. Chem. Soc.* **128**(4), 1088–1089 (2006).
- [252] M.-H. Li, P. Keller, Artificial muscles based on liquid crystal elastomers, *Philos. Trans. Royal Soc. A* **364**(1847), 2763–2777 (2006).
- [253] B. N. Peele, T. J. Wallin, H. Zhao, R. F. Shepherd, 3D printing antagonistic systems of artificial muscle using projection stereolithography, *Bioinspiration Biomim.* **10**(5), 055003 (2015).
- [254] Z. Li, J. Torgersen, A. Ajami, S. Muhleder, X. Qin, W. Husinsky, W. Holthoner, A. Ovsianikov, J. Stampfl, R. Liska, Initiation efficiency and cytotoxicity of novel water-soluble two-photon photoinitiators for direct 3D microfabrication of hydrogels, *RSC Adv.* **3**(36), 15939 (2013).

- [255] J. Fischer, G. Freymann, M. Wegener, The materials challenge in diffraction-unlimited direct-laser-writing optical lithography, *Adv. Mater.* **22**(32), 3578–3582 (2010).
- [256] V. P. Rajamanickam, L. Ferrara, A. Toma, R. P. Zaccaria, G. Das, E. D. Fabrizio, C. Liberale, Suitable photo-resists for two-photon polymerization using femtosecond fiber lasers, *Microelectron. Eng.* **121**, 135–138 (2014).
- [257] E. Harnisch, M. Russew, J. Klein, N. König, H. Crailsheim, R. Schmitt, Optimization of hybrid polymer materials for 2pp and fabrication of individually designed hybrid microoptical elements thereof, *Opt. Mater. Express* **5**(2), 456–461 (2015).
- [258] D. Bäuerle, *Laser Processing and Chemistry* (Springer Nature, 2011).
- [259] K. Maximova, X. Wang, A. Balčytis, L. Fan, J. Li, S. Juodkasis, Silk patterns made by direct femtosecond laser writing, *Biomicrofluidics* **10**(5), 054101 (2016).
- [260] M. Malinauskas, A. Žukauskas, G. Bičkauskaitė, R. Gadonas, S. Juodkasis, Mechanisms of three-dimensional structuring of photopolymers by tightly focussed femtosecond laser pulses, *Opt. Express* **18**(10), 10209 (2010).
- [261] Microresist, *UV-Curable Hybrid Polymers for Micro Optical Components* (2015).
- [262] G. Batavičiūtė, M. Ščiuka, A. Melninkaitis, Direct comparison of defect ensembles extracted from damage probability and raster scan measurements, *J. Appl. Phys.* **118**(10), 105306 (2015).
- [263] V. Mizeikis, V. Purlys, R. Buvidas, S. Juodkasis, Realization of structural color by direct laser write technique in photoresist, *J. Laser Micro. Nanoeng.* **9**(1), 42–45 (2014).

# Santrauka

Spartus medžiagų apdirbimo lazeriu technologijos vystymasis paskatino daugybės naujų tyrimų sričių atsiradimą. Ypač įdomus yra fs lazeris, leidžiantis neprilygstamai tiksliai lokalizuoti ir kontroliuoti šviesos ir medžiagos sąveiką. Tai lemia minimalų ir (arba) kontroliuojamą šiluminį efektą bei labai aukštą apdirbimo tikslumą (iki šimtų nm). Viena iš technologijų, kuri paremta greita šviesos ir medžiagos sąveika, yra 3D lazerinė litografija (3DLL). Tai yra adityvi gamybos technika, leidžianti panaudoti daugybę medžiagų ir sukurti laisvai pasirenkamos formos 3D struktūras. Nepaisant to, nors buvo įrodyta, kad tai puikus įrankis gaminant įvairius mikromechaninius, medicininius, optinius ir fotoninius darinius, vis dar yra neišspręstų problemų, susijusių su šios metodikos našumu. Be to, yra neapibrėžtumų susijusių su kai kuriomis galutinių darinių savybėmis, pavyzdžiui, koks yra lazeriu indukuotos pažaidos slenkstis. Šiuo darbu siekiama atsakyti į kai kuriuos iš šių klausimų.

Pirma, buvo sprendžiamas mezoskalinių 3D struktūrų gamybos klausimas. Mes apibrėžiame, kad mezoskaliniai dariniai turi nm- $\mu$ m lygio pavienius komponentus, o bendras jų dydis yra iki mm-cm. Galimybė gaminti tokius darinius naudojant 3DLL labai pagerintų technologijos patrauklumą platesniam vartotojų ratui ir padėtų ją išpopuliarinti. Norint realizuoti gamybą mezoskalėje, buvo naudojamas sinchronizuotas vienalaikis galvo-skenerių ir linijinių stalų judėjimas. Tai leido sumažinti pozicionavimo klaidas, tuo pačiu išlaikant mm/s-cm/s lygio transliavimo greitį su aukštesniu nei  $\mu$ m pozicionavimo tikslumu. Buvo išnagrinėtos galimos tokio metodo galimybės, taip pat paaiškinti galimi apribojimai susiję su kai kurių geometrijų (pvz., mikrooptikos) ar mažo impulsų pasikartojimo dažnio ( $\sim$ kHz) lazerinių sistemų panaudojimu. Taip pat buvo parodytos galimybės išplėsti šią metodiką naudojant skirtingas fokusavimo sąlygas. Apibendrinus buvo parodyta, jog apdirbimo spartą galima derinti dviem eilėmis nuo  $\sim 1800 \mu\text{m}^3/\text{s}$  iki  $\sim 31300 \mu\text{m}^3/\text{s}$ . Tai reiškia, kad, kalbant apie našumą, 3DLL užima nišą tiesiai po mikrostereolitografijos.

Toliau buvo nagrinėjama galimybė vykdyti 3DLL nenaudojant fotoiniciatoriaus. Fotolitografijai skirtas polimero pirmtakas susideda iš monomero mišinio ir fotocheminį aktyvumą turinčio priedo. Pastarasis reikalingas norint lengvai sukelti fotocheminę reakciją ir paskesnę cheminę tinklinimą. Tačiau dėl galimybės kontroliuoti šviesos ir medžiagos sąveiką 3DLL proceso

metu, fotopolimerizacijos procesas gali būti realizuotas naudojant polimero pirmtaką be fotoiniciatoriaus. Parodyta, kad gamybos langai yra panašaus dydžio ( $\Delta I_{IRG} - \Delta I_{pure} = 0,16 \text{ TW/cm}^2$  arba 15,5 % skirtumas) ir, naudojant tinkamus apdirbimo parametrus, dariniai nerodo jokių neigiamų mechaninės kokybės požymių. Be to, gamyba be fotoiniciatoriaus leidžia lengviau pasiekti didesnę apdirbimo raišką ir leidžia pasiekti paviršiaus šurkštumą kuris yra mažiau nei 10 nm RMS. Ši metodika taip pat suderinama su žemesniu NA (0,45) fokusavimu, įrodančiu jos perspektyvas gaminant mezoskalinius darinius. Apskritai pateikti rezultatai leidžia teigti, jog srityse, kuriuose tai galėtų būti naudinga, gamyba be fotoiniciatorių yra visiškai priimtina. Tokių taikymų pavyzdžiais galėtų būti biomedicina, kur fotoiniciatorius gali būti toksiškas ląstelėms, arba mikrooptika / fotonika, kur papildoma sugertis gali lemti informacijos praradimą arba net žemesnį optinės pažaidos slenkstį.

Galiausiai buvo ištirtos 3DLL darinių optinės pažaidos savybės. Buvo naudojami tiek kokybiniai, tiek kiekybiniai matavimo metodai. Kokybinis tyrimas buvo pagrįstas mikrolęšio veikimo stebėjimu jį apšviečiant intensyvia ( $\text{GW/cm}^2$ ) fs-lazerio spinduliuote. Pasirodė, jog medžiaga neturinti fotoiniciatoriaus yra pranašesnė: laikas reikalingas katastrofiniam lęšio sugadinimui fotojautrinioje medžiagoje sumažėjo  $\sim 7$  kartus, kai fotoiniciatoriaus koncentracija padidėjo iki 2 % w.t. Toliau, buvo atliktas kiekybinis matavimas, pagrįstas modifikuotu ISO standarto testavimu. Tam 3DLL iš įvairių medžiagų buvo gaminami 10x10 stačiakampių gretasienių arba fotoninių kristalų masyvai, kurie po to buvo paveikti įvairiais lazerio parametrais. Tai leido statistiškai apskaičiuoti išbandytų medžiagų pažaidos slenkstį. Bendrosios tendencijos buvo tokios, kad jis priklauso nuo medžiagos sugerties (kuo mažesnė sugertis, tuo aukštesnis slenkstis), sudėties (visiškai organiniai *vs* hibridiniai organiniai-neorganiniai) ir geometrijos (fotoniniai kristalai turėjo kitokį pažaidos slenkstį nei tūriniai dariniai). Iš visų medžiagų grynas organinis-neorganinis SZ2080 parodė aukščiausią slenkstį -  $161,9 \text{ TW/cm}^2$ , kuris yra maždaug eile žemesnis už lydytą kvarcą.

# Curriculum Vitae

## Personal information

Name, Surname: Linas Jonušauskas  
Birthday: 1991 02 10  
Place of birth: Joniškėlis, Pasvalys county  
E-mail: linas.jon@gmail.com

## Education

2016–2020: Vilnius University, Faculty of Physics,  
Laser Research center, PhD studies  
2014–2016: Vilnius University, Faculty of Physics,  
Master studies  
2010–2014: Vilnius University, Faculty of Physics,  
Bachelor studies  
1998–2010: Joniškėlis Gabrielė Petkevičiatė-Bite  
Gymnasium, High school education

## Work Experience

2020 12–Present Head of Research (Valsigna Ghmb)  
2018 11–Present Chief Scientific Officer (Femtika LLC)  
2016 07–2017 12 Junior Researcher (Vilnius University,  
Laser Research Center)  
2015 10–2018 11 Junior Researcher, Researcher &  
Spokesman (Femtika LLC)

## Internships

2016 11–2016 12 CNRS, LOMA (France)

## Other information

**Scholarships** INFOBAL Scholarship for the Best  
Young Scientists (Vilnius, Lithuania,  
2020)

## Awards

Award from Lithuanian Academy of Sciences for the Best Young Scientist Work in Technological Sciences (Vilnius, Lithuania, 2020)

Best Student Paper Award in the International Scientific Conference *SPIE Optics + Optoelectronics 2017* (Prague, Czech Republic, 2017)

Award from Lithuanian Academy of Sciences for the Best Student Scientific Work in Technological Sciences (Vilnius, Lithuania, 2017)

Awarded for the Best Master Degree Graduation Thesis by the Ministry of Economy of the Republic of Lithuania (Vilnius, Lithuania, 2016)

Best Oral Presentation in International Scientific Conference *Open Readings 2013* (Vilnius, Lithuania, 2013)

Best Oral Presentation in International Scientific Conference *Open Readings 2012* (Vilnius, Lithuania, 2012)

## Notes

Vilnius University Press  
9 Saulėtekio Ave., Building III, LT-10222 Vilnius  
Email: [info@leidykla.vu.lt](mailto:info@leidykla.vu.lt), [www.leidykla.vu.lt](http://www.leidykla.vu.lt)  
Print run copies 20